Hybrid Actuation in Haptics and Human-Friendly Robotics

By

Patrick Dills

A dissertation submitted in partial fulfillment of

the requirements for the degree of

Doctor of Philosophy

Mechanical Engineering

at the

UNIVERSITY OF WISCONSIN-MADISON

2024

Date of final oral examination: 06/04/2024

This dissertation is subject to approval by the following members of the Final Oral Committee:

Michael R. Zinn, Professor, Mechanical Engineering
Peter G. Adamczyk, Associate Professor, Mechanical Engineering
Kreg Gruben, Associate Professor, Biomedical Engineering
Dan Negrut, Professor, Mechanical Engineering
Darryl G. Thelen, Professor, Mechanical Engineering

Acknowledgements

I would be remiss without first acknowledging my mom Cathy Reiner and dad Richard Dills along with my grandparents George and June Reiner who intentionally or unintentionally fostered my interests in science and engineering throughout my youth. You gave me the space to tinker without me understanding what I was doing. I want to thank my sister Kristin Dills for allowing me to tag along with you to your high school engineering clubs. Undoubtably, Kristi Dills has given me love and support all along my journey and I would not be who I am without it.

I want to thank the mentors of the Jesuit high school robotics team, specifically Mr. Jerry Glasser who believed in me and gave me more leeway in the physics lab than I probably deserved. I also want to thank Edward Novinski my high school studio art teacher who helped to sustain my love of the outdoors thorough adolescence and showed me how to make a figure without having made one himself. Along the way, I had several key mentors and experiences in my time as an undergraduate. I want to thank Dave Tostenson who gave me my first engineering job in his consulting firm, Nick Repanich and Jason Coats for the experience and opportunity at the California Mechatronics Center, and an unknown study abroad coordinator at CSU Chico that allowed me to travel the world a bit and to get out of my shell.

I did not embark on this journey to a PhD intentionally and instead I came to Madison to simply become a better engineer. In the first year of my time in graduate school my friends and family were clearly my greatest allies and supported me through a tumultuous time. In no specific order of importance, Peter Killeen, Ryan Backman, Hasan Hakim, Muhamad Alvi, Dan Erato, Eugene Rush, Pablo E. Castro Palavicino, and Timmothy Polum all helped to support me early on in graduate school. Upon joining the REACH Lab, the guidance of my lab mate Chembian Parthiban and initial research collaborations with Nick Colonnese and Priyanshu Agarwal helped

set me upon my journey which ultimately morphed into this dissertation. Other lab members and colleagues who have made my time both fulfilling and memorable include It Fufuengsin, Kaitlyn Gabardi, Megh Doshi, Bolun Zhang, Mike Hagenow, and Alexander Dawson-Elli.

The mentorship, friendship, and guidance of my advisor Mike Zinn cannot be understated. Some have said that in the REACH lab "you get a PhD in Mechanical Engineering and in life". We hiked up Mt. Fuji together, opened a "home lab" during a global pandemic, golfed around Madison, and charted new research directions in weekly meetings. I am grateful for the time Mike has consistently made for me over the years. He showed me both through his actions and words how to build an inspiring engineering career, how to be a mentor, and how to be a well-rounded person in academia. He has shown me that there isn't a single path to success and his belief in me has directly corresponded with my success in graduate school. Although I have always been drawn to science and engineering, I doubt I would have continued down the path to a PhD without his support and encouragement.

Other mentors of note include Peter Adamczyk and Kreg Gruben, who also gave valuable perspectives, energy, and time during many research meetings over the years spent working on our National Robotics Initiative (NRI) project. Additionally, I appreciate the time of Dan Negrut and Darryl Thelen who round out my committee. I have had many teachers and professors over my grad school career, but the notable ones include Eric Oberstar, Robert Lorenz, Matt Allen, Willam (Bill) Setharus, Laurent Lessard, and of course Mike Zinn. Thank you.

Funding Support

I gratefully acknowledge the following funding support for my dissertation research and travel:

- Funding from Oculus Research, Facebook Reality Labs, or Meta Reality Labs
- The NSF and National Robotics Initiative (grant: NSF 1830516)
- Madison Vilas Life Cycle Award
- Student Research Travel Grant Competition – Combined

Abstract

This work presents a hybrid actuation approach for haptic interfaces and cooperative physical human-robot interaction which combines active energy producing and passive energy neutral or absorbing actuators in parallel. Two variations of the actuation approach are applied to several devices across a range of interaction motion and force amplitudes. Parallel hybrid actuation which combines a simple brake and DC motor in parallel addresses the needs of small-scale handheld haptic devices. Balanced Hybrid Actuation combines a brake, a Series Elastic Actuator, and a DC motor in parallel to address the needs of larger workspace and force haptic devices. The presented parallel hybrid actuation topologies increase the dynamic range of the device as compared to traditional active only rendering approaches (i.e. DC motors and macro-mini concepts). When used as a haptic device, the hybrid actuators dynamic range is expanded in terms of the range of stable impedances it can achieve. Stability analysis shows that the spring-like characteristics of the passive actuator in combination with a parallel feedback control topology are responsible for the increased range of both passive and asymptotically stable impedances (i.e. virtual stiffness and damping). The actuation approaches do so while overcoming problems in rendering accuracy (like the “sticky effect”) which are common in hybrid actuators due to their nonlinear nature. When used as a robotic actuator for cooperative robots, the actuator displays increased servoing capability, reduced energy consumption, and unique synergy between actuators when tracking trajectories. The actuator does so while remaining low impedance and safe. Finally, we demonstrate the effectiveness of the approach in multiple degrees of freedom with a two degree of freedom hybrid interface designed for lower limb rehabilitation and human scale lower limb forces.

Table of Contents

List of Figures

Chapter 1

Chapter 2

Chapter 3

Chapter 4

Chapter 5

Chapter 6

Appendix A

Appendix C

Appendix D

List of Tables

Introduction to The Thesis

Chapter 3

Chapter 4

Chapter 6

Introduction to the Thesis

An actuator is a force transducer which converts one form of energy into an output force or torque. A necessary part of an actuator is a control system to regulate the energy conversion process and the output force or torque. Electric motors are undoubtably the most common actuator in kinesthetic haptic devices and cooperative human friendly robots. This is predominately due to the established infrastructure and methodologies surrounding their use in position control or pick and place applications (the traditional domain of robotics). As robotics moved away from this domain demands on the actuators which compose robots changed. To address these new demands researchers have explored a complex "taxonomy" of robotic actuators and *actuation approaches*. In this work we discuss actuation approaches specifically for kinesthetic haptics and safe human friendly physical robot interaction

A. General Existing Actuation Approach Categories

Performance of an impedance controlled haptic device or cooperative robot is evaluated by a device's dynamic range. A haptic device with a large dynamic range can stably and accurately render stiff surfaces and have a low output impedance. In cooperative robotics these attributes correspond to a robot with a high control bandwidth to accomplish position tracking tasks, while maintaining safety by reducing injury risks associated with impacts. The ideal device for either application would be able maintain essential characteristics across a large range of workspace sizes and would be capable of producing a large range of forces. Existing actuation approaches have adopted various design approaches but still fall short of this ideal. While somewhat subjective, we have organized this prior work into five categories, classified according to the type and characteristics of the actuation approach (see Table 1).

The first actuation category is comprised of passive and shape rendering devices that utilize mechanical brakes to render kinesthetic feedback to the user. Actuation approaches in this class of device take the form of a brake which can be used to render the shape of the virtual object or a limited set of virtual impedances [1,2]. These devices can typically provide very large forces, due to their passive shape rendering mechanisms, but lack the ability to render a diverse range of impedances.

The second actuation category includes devices that utilize highly geared electric motors, providing a high force/torque density while minimizing weight and resource usage. These devices incorporate output force or torque sensing for feedback and are controlled in an admittance mode where a force control loop is wrapped around the position control loop to render the virtual environment [3]. These actuators are limited by their position control bandwidth and consequently are limited in transparency and force bandwidth.

The third actuation category consists of devices that utilize compliant actuation, typically controlled as a series elastic actuator (SEA) [4]. This approach has been adopted for wearable hand exoskeletons [5,6] and many other applications. These actuators place a compliant (series elastic) element between the user and the actuator, allowing for closed loop force control through the measurement of the compliant element's deflection. Speed reducers used in the SEA increase the range of controllable force magnitudes while maintaining transparency, but they are limited in force control bandwidth.

The fourth actuation category consists of devices that pair electric motors with a small speed reducer, (often a cable reduction) and are often used to provide kinesthetic feedback in hand-centered haptic devices [7,8]. The small gear reduction limits reflected actuator inertia but also the magnitude of forces or torques the actuator can produce.

Employing a larger gear ratio in a haptic device enables larger forces and torques but can negatively impact transparency. Control techniques can help to overcome this limitation in free space and zero force components of a haptic rendering where they are the most noticeable. However, the limitation persists and ultimately distorts a devices desired renderings leading to a somewhat compromised rendering while producing large forces [9,10].

The final actuation category consists of devices that use pneumatic actuators. These devices can address force magnitude and transparency requirements but have trouble providing the torque bandwidth needed for a high-quality rendering [11,12]. Table 1 summarizes which high-level ungrounded kinesthetic haptic design requirements are addressed by each of the five actuation categories discussed.

TABLE 1: KINESTHETIC HAPTIC ACTUATION APPROACHES

Actuation Approach	**Kinesthetic Haptic Design Criteria Composing Dynamic Range**				
	Large Forces	***Large Bandwidth of Force***	***Transparent***	***High Stiffness***	***Variable Impedance Rendering***
Passive Brakes [1,2]	✓	✗	✓	✓	✗
Admittance Control [3]	✓	✗	✗	✓	✓
SEA's [5,6]	✓	✗	✓	✗	✓
Lightly Geared DC Motors [7,8]	✗	✓	✓	✓	✓
Highly Geared DC Motors [9,10]	✓	✓	✗	✓	✓
Pnumatic Devices [11,12]	✓	✗	✓	✗	✓

B. Hybrid Actuation in Haptics

Both active and passive actuators have been commonly used to build haptic displays and they serve different purposes. Active actuators, such as electric motors, can provide high active forces, fast response times and are symmetrical in rendering i.e. they can supply and dissipate energy easily. Performance is limited by stability, which is affected by the physical characteristics of the device and the computer interface. Several researchers have studied the effect of compliance, backlash, friction, sampling, encoder quantization, and delay on performance [13-19]. Colgate showed that the stable rendering range could be improved by adding physical damping to the system [20]. This, coupled with low torque density in active actuators, has led to the use of passive actuators in haptic displays.

Passive actuators have a high torque density, are inherently stable and safe. Since they can dissipate energy, they can be used to increase the physical damping of the system and ensure passivity for stable operations [21]. They can render high passive forces as opposed to electrical motors that may require large gear reductions to achieve the same force levels. However, passive actuators are limited in the range of haptic perceptions they can render [22]. They also can have relatively slow response times when compared to electric motors, which affects device rendering accuracy and transparency. The slow response time and uncertainty regarding the precise output of the passive actuator can result in a mismatch in the active and passive torques, particularly problematic during periods the desired rendering torque frequently oscillates between large active and passive torque, such as would be the case when interacting with a stiff virtual wall. This is commonly known as the “sticky-effect” [23]. In addition, passive actuators typically have residual torques present when powered off which can affect the device’s transparency.

More recently, the use of hybrid actuation in haptics – the coordinated use of controlled passive actuators in parallel with active actuators – has been motivated by its demonstrated advantages including high passive force capacity, low external power requirements, low output impedance when deactivated, improved control robustness, and improved passive force rendering. Interest in hybrid actuation has increased as the advantages of passive actuation have been recognized. Specific hybrid actuation configurations that have been investigated include the use of magnetorheological (MR) brakes in parallel with electric actuators [24-26], dual MR brakes coupled through an overrunning clutch (to reduce the negative effects of the MR brake's nonlinear characteristics) [23], use of a particle brake in series with an elastic spring and an electric actuator [27] and similar configurations using alternative passive actuators such as eddy-current dampers [28]. While improvements in performance and control robustness have been demonstrated using these approaches, they suffer from one or more significant issues which limit their application, including slow response speed and nonlinear hysteresis associated with the passive actuator [29], and a large mismatch between the active and passive actuators, where the passive torque and power capacity can be an order of magnitude larger than the active capacity [23].

C. Hybrid Actuation in Cooperative Physical Human-Robot Interaction

In recent years robotic manipulators have been delegated tasks which bring them into increasingly closer contact with people. Prime examples include the proliferation of manufacturing cobots, human exoskeletons, and rehabilitation robots [30]. Existing systems are not well suited to applications that require high force (>30-150N) and high power (>60-600 watts) while also maintaining the physical characteristics important for safe and effective physical interaction and human-robot collaboration. While much progress has been made in co-robotics, the overwhelming focus has been on robotic manipulators which have relatively low power capacity, such that the inherent safety risks when working directly with humans are minimized. The focus has been on the design and control of naturally light weight and compliant manipulators [4]. In this case, human-robot physical interaction and cooperation is enabled via the manipulator’s naturally low output impedance, which both facilitates the control of robot-human physical interaction and limits the total energy transferred during an uncontrolled collision between a robot and a human (the greatest safety risk) [31].

Unfortunately, the control and design approach applied to low power systems does not scale to manipulators with high force, power, and bandwidth requirements. Due primarily to the limitations of actuation technology [32], high power manipulators must employ transmission designs to achieve the forces and stiffness required. Such designs can cause an unsafe amount of output impedance.

To enable high-performance physical human-robot interaction, the output impedance of high-power manipulators must be reduced to levels sufficient to guarantee inherent safety and to enable human-robot physical interaction without sacrificing the characteristics important to manipulation tasks. Researchers have investigated the use of active force and impedance control [33], which has been used widely in low-power manipulators. However, in high-power systems, force or impedance control is limited by the manipulator’s lack of self-sensing capability (motor torque measurements cannot be used reliably to estimate contact forces), a capability inherent to low-power co-robotic manipulators. Even when feedback control is used, such as instrumenting the manipulator’s end-effector with a force/torque sensor used in feedback [34], the improved performance is limited to point-to-point interactions at the end effector and is only effective below the feedback control bandwidth.

To simultaneously realize high power and low output impedance, researchers have explored the use of a diverse range of variable impedance actuation strategies [33]. Active compliant actuation, such as the series elastic actuator (SEA) [4], [35], [36], variable stiffness actuators [37], and variations on these designs place an elastic element in between a speed reducer and the actuator output. Output impedance is reduced through control resulting in a power dense torque source below the control bandwidth of the actuator. Attempts to extend the performance of series elastic actuators have been made with some success by including a small secondary motor on the output to extend the torque frequency range of the actuator as a whole [27].

Hybrid actuation, the combination of controlled passive actuators, such as brakes or dampers, and active actuators, such as electric motors, has recently demonstrated advantages including high passive force capability, energy efficiency, low output impedance, and improved control robustness. Existing hybrid actuators include haptic devices utilizing magnetorheological (MR) brakes in parallel with DC Motors [23]. Passive Eddy current dampers and back EMF properties of electric motors are also used to provide variable damping sources in parallel with active electric motors to provide increased control robustness and aid in rapid actuator movements [28], [38]. Series damping actuators and series clutch actuators utilize clutches to isolate the high impedance gear head in a similar way to SEA's [39], [40]. Parallel combinations of clutch's and SEA's have been shown to improve actuator energy efficiency [41], [42]. McKibbin muscles and mini brakes were shown to increase actuator performance under large impacts [43]. Performance gains from hybrid actuation are considerable, yet hybrid actuators often still suffer from nonlinearities associated with passive actuators, a low control bandwidth, and oftentimes an inherent imbalance between passive and active actuator torque capability [23].

D. A Hybrid Actuation Thesis

Both haptics and cooperative human-robot physical interaction are in need of an actuation approach which provides high levels of disturbance rejection (high stiffness rendering or high bandwidth) while remaining low impedance (transparent and safe). Current actuation approaches fall short of what is needed in both haptics and cooperative robotics.

> *Hybrid actuation has the potential to accomplish the goals of kinesthetic haptic devices and cooperative robots. A new hybrid actuation approach is needed to capitalize on hybrid actuation benefits while mitigating potential downfalls of hybrid actuation.*

Principal amongst these downfalls is the difficulty of controlling hybrid actuators in both haptics and cooperative robotics. This work aims to propose a new hybrid actuation approach and to explore control methods to capture performance benefits of hybrid actuation for both haptic and cooperative robotic applications.

E. Document Organization

The discussion of our proposed hybrid actuation approach is organized into the following sections. Chapter 1 focuses on describing the actuation and control approach concept used in haptics. We cover the arrangement and function of the parallel and balanced hybrid approaches and how they may be applied to a wide range of actuation scales and degrees of freedom. We subsequently discuss the stability properties of the parallel hybrid haptic approach. In Chapter 2 we focus on passivity of the feedback control structure and discuss the dissipative properties of the parallel hybrid actuation approach. Chapter 3 focuses on asymptotic stability of the feedback control approach. Chapter 4 focuses on an experimental validation of the approach. In Chapter 5 we discuss limitations upon the actuation approach in haptic applications and how they might be mitigated. Finally in Chapter 6 we discuss how the hybrid actuator could be used in physical human robot collaboration and human friendly robotics while using trajectory optimization and active only feedback control approach.

References:

[1] J. Blake and H. B. Gurocak, “Haptic Glove With MR Brakes for Virtual Reality,” *IEEE/ASME Trans. Mechatron.*, vol. 14, no. 5, pp. 606–615, Oct. 2009, doi: 10.1109/TMECH.2008.2010934.

[2] I. Choi, E. W. Hawkes, D. L. Christensen, C. J. Ploch, and S. Follmer, “Wolverine: A wearable haptic interface for grasping in virtual reality,” in *2016 IEEE/RSJ International Conference on Intelligent Robots and Systems (IROS)*, Daejeon, South Korea: IEEE, Oct. 2016, pp. 986–993. doi: 10.1109/IROS.2016.7759169.

[3] I. Choi, E. Ofek, H. Benko, M. Sinclair, and C. Holz, “CLAW: A Multifunctional Handheld Haptic Controller for Grasping, Touching, and Triggering in Virtual Reality,” in *Proceedings of the 2018 CHI Conference on Human Factors in Computing Systems*, Montreal QC Canada: ACM, Apr. 2018, pp. 1–13. doi: 10.1145/3173574.3174228.

[4] G. A. Pratt and M. M. Williamson, “Series elastic actuators,” in *Proceedings 1995 IEEE/RSJ International Conference on Intelligent Robots and Systems. Human Robot Interaction and Cooperative Robots*, Pittsburgh, PA, USA: IEEE Comput. Soc. Press, 1995, pp. 399–406. doi: 10.1109/IROS.1995.525827.

[5] P. Agarwal, Y. Yun, J. Fox, K. Madden, and A. D. Deshpande, “Design, control, and testing of a thumb exoskeleton with series elastic actuation,” *The International Journal of Robotics Research*, vol. 36, no. 3, pp. 355–375, Mar. 2017, doi: 10.1177/0278364917694428.

[6] I. Jo and J. Bae, “Design and control of a wearable hand exoskeleton with force-controllable and compact actuator modules,” in *2015 IEEE International Conference on Robotics and Automation (ICRA)*, Seattle, WA, USA: IEEE, May 2015, pp. 5596–5601. doi: 10.1109/ICRA.2015.7139982.

[7] R. M. Pierce, E. A. Fedalei, and K. J. Kuchenbecker, “A wearable device for controlling a robot gripper with fingertip contact, pressure, vibrotactile, and grip force feedback,” in *2014 IEEE Haptics Symposium (HAPTICS)*, Houston, TX, USA: IEEE, Feb. 2014, pp. 19–25. doi: 10.1109/HAPTICS.2014.6775428.

[8] CyberGrasp™ User’s Guide v1.2, Immersion Corporation, San Jose C.A., 2000- 2003.

[9] P. Dills and M. Zinn, “Transparent, High-Force, and High-Stiffness Control of Haptic Actuators with Backlash,” in *2023 IEEE World Haptics Conference (WHC)*, Delft, Netherlands: IEEE, Jul. 2023, pp. 439–445. doi: 10.1109/WHC56415.2023.10224471.

[10] P. Dills and M. Zinn, “Transparent, High-Force, and High-Stiffness Control of Haptic Actuators with Backlash: A Multi Degree of Freedom Approach,” in *2024 IEEE Haptics Symposium (HAPTICS)*, Long Beach, CA, USA: IEEE, Apr. 2024, pp. 278–285. doi: 10.1109/HAPTICS59260.2024.10520856.

[11] M. Bouzit, G. Burdea, G. Popescu, and R. Boian, “The Rutgers Master II-new design force-feedback glove,” *IEEE/ASME Trans. Mechatron.*, vol. 7, no. 2, pp. 256–263, Jun. 2002, doi: 10.1109/TMECH.2002.1011262.

[12] Y. Zhang, D. Wang, Z. Wang, Y. Wang, L. Wen, and Y. Zhang, “A two-fingered force feedback glove using soft actuators,” in *2018 IEEE Haptics Symposium (HAPTICS)*, San Francisco, CA: IEEE, Mar. 2018, pp. 186–191. doi: 10.1109/HAPTICS.2018.8357174.

[13] M. Minsky, F. P. Brooks, and M. Behensky, “Feeling and Seeing : Issues in Force Display”.

[14] N. Diolaiti, G. Niemeyer, F. Barbagli, and J. K. Salisbury, “Stability of Haptic Rendering: Discretization, Quantization, Time Delay, and Coulomb Effects,” *IEEE Trans. Robot.*, vol. 22, no. 2, pp. 256–268, Apr. 2006, doi: 10.1109/TRO.2005.862487.

[15] J. J. Abbott and A. M. Okamura, “Effects of position quantization and sampling rate on virtual-wall passivity,” *IEEE Trans. Robot.*, vol. 21, no. 5, pp. 952–964, Oct. 2005, doi: 10.1109/TRO.2005.851377.

[16] N. Colonnese and A. Okamura, “Stability and quantization-error analysis of haptic rendering of virtual stiffness and damping,” *The International Journal of Robotics Research*, vol. 35, no. 9, pp. 1103–1120, Aug. 2016, doi: 10.1177/0278364915596234.

[17] C. Parthiban and M. Zinn, “Performance and stability limitations of admittance-based haptic interfaces,” in *2018 IEEE Haptics Symposium (HAPTICS)*, San Francisco, CA: IEEE, Mar. 2018, pp. 58–65. doi: 10.1109/HAPTICS.2018.8357153.

[18] P. Dills, K. Gabardi, and M. Zinn, “Stability and Rendering Limitations of High-Performance Admittance Based Haptic Interfaces,” in *2022 IEEE Haptics Symposium (HAPTICS)*, Santa Barbara, CA, USA: IEEE, Mar. 2022, pp. 1–8. doi: 10.1109/HAPTICS52432.2022.9765573.

[19] M. Zinn, O. Khatib, B. Roth, and J. K. Salisbury, “Large Workspace Haptic Devices - A New Actuation Approach,” in *2008 Symposium on Haptic Interfaces for Virtual Environment and Teleoperator Systems*, Reno, NV, USA: IEEE, Mar. 2008, pp. 185–192. doi: 10.1109/HAPTICS.2008.4479941.

[20] J. E. Colgate and J. M. Brown, “Factors affecting the Z-Width of a haptic display,” in *Proceedings of the 1994 IEEE International Conference on Robotics and Automation*, San Diego, CA, USA: IEEE Comput. Soc. Press, 1994, pp. 3205–3210. doi: 10.1109/ROBOT.1994.351077.

[21] J. An and D.-S. Kwon, “Stability and Performance of Haptic Interfaces with Active/Passive Actuators—Theory and Experiments,” *The International Journal of Robotics Research*, vol. 25, no. 11, pp. 1121–1136, Nov. 2006, doi: 10.1177/0278364906071034.

[22] M. Lacki and C. Rossa, “Design and Control of a 3 Degree-of-Freedom Parallel Passive Haptic Device,” *IEEE Trans. Haptics*, vol. 13, no. 4, pp. 720–732, Oct. 2020, doi: 10.1109/TOH.2020.2983037.

[23] C. Rossa, J. Lozada, and A. Micaelli, “Design and Control of a Dual Unidirectional Brake Hybrid Actuation System for Haptic Devices,” *IEEE Trans. Haptics*, vol. 7, no. 4, pp. 442–453, Oct. 2014, doi: 10.1109/TOH.2014.2346501.

[24] Jinung An and Dong-soo Kwon, “Haptic experimentation on a hybrid active/passive force feedback device,” in *Proceedings 2002 IEEE International Conference on Robotics and Automation (Cat. No.02CH37292)*, Washington, DC, USA: IEEE, 2002, pp. 4217–4222. doi: 10.1109/ROBOT.2002.1014416.

[25] Jinung An and Dong-Soo Kwon, “Control of multiple DOF hybrid haptic interface with active/passive actuators,” in *2005 IEEE/RSJ International Conference on Intelligent Robots and Systems*, Edmonton, Alta., Canada: IEEE, 2005, pp. 2572–2577. doi: 10.1109/IROS.2005.1545361.

[26] H. Qin, A. Song, and Y. Mo, “A hybrid actuator with hollowed multi-drum magnetorheological brake and direct-current micromotor for hysteresis compensation,” *Journal of Intelligent Material Systems and Structures*, vol. 30, no. 7, pp. 1031–1042, Apr. 2019, doi: 10.1177/1045389X19828473.

[27] F. Conti and O. Khatib, “A New Actuation Approach for Haptic Interface Design,” *The International Journal of Robotics Research*, vol. 28, no. 6, pp. 834–848, Jun. 2009, doi: 10.1177/0278364908097958.

[28] A. H. C. Gosline and V. Hayward, “Eddy Current Brakes for Haptic Interfaces: Design, Identification, and Control,” *IEEE/ASME Trans. Mechatron.*, vol. 13, no. 6, pp. 669–677, Dec. 2008, doi: 10.1109/TMECH.2008.2004623.

[29] M. Antolini, O. Kose, and H. Gurocak, “A first order transfer function to balance the workload in brake-motor hybrid actuators,” in *2014 IEEE Haptics Symposium (HAPTICS)*, Houston, TX, USA: IEEE, Feb. 2014, pp. 509–514. doi: 10.1109/HAPTICS.2014.6775508.

[30] H. Vallery, J. Veneman, E. Van Asseldonk, R. Ekkelenkamp, M. Buss, and H. Van Der Kooij, “Compliant actuation of rehabilitation robots,” *IEEE Robot. Automat. Mag.*, vol. 15, no. 3, pp. 60–69, Sep. 2008, doi: 10.1109/MRA.2008.927689.

[31] M. Zinn, B. Roth, O. Khatib, and J. K. Salisbury, “A New Actuation Approach for Human Friendly Robot Design,” *The International Journal of Robotics Research*, vol. 23, no. 4–5, pp. 379–398, Apr. 2004, doi: 10.1177/0278364904042193.

[32] J. M. Hollerbach, I. W. Hunter, and J. Ballantyne, “A comparative analysis of actuator technologies for robotics,” in *The Robotics Review 2*, Cambridge, MA, USA: MIT Press, 1992, pp. 299–342.

[33] N. Hogan, “Impedance Control: An Approach to Manipulation,” in *1984 American Control Conference*, San Diego, CA, USA: IEEE, Jul. 1984, pp. 304–313. doi: 10.23919/ACC.1984.4788393.

[34] R. Q. Van der Linde, P. Lammertse, E. Frederiksen, and B. Ruiter, “The Hapticmaster, a New High Performance Haptic Interface,” in *Proc. Eurohaptics, 2002*, pp. 1–5.

[35] D. P. Losey, A. Erwin, C. G. McDonald, F. Sergi, and M. K. O’Malley, “A Time-Domain Approach to Control of Series Elastic Actuators: Adaptive Torque and Passivity-Based Impedance Control,” *IEEE/ASME Trans. Mechatron.*, vol. 21, no. 4, pp. 2085–2096, Aug. 2016, doi: 10.1109/TMECH.2016.2557727.

[36] N. Paine, S. Oh, and L. Sentis, “Design and Control Considerations for High-Performance Series Elastic Actuators,” *IEEE/ASME Trans. Mechatron.*, vol. 19, no. 3, pp. 1080–1091, Jun. 2014, doi: 10.1109/TMECH.2013.2270435.

[37] A. Bicchi and G. Tonietti, “Fast and ‘Soft-Arm’ Tactics,” *IEEE Robot. Automat. Mag.*, vol. 11, no. 2, pp. 22–33, Jun. 2004, doi: 10.1109/MRA.2004.1310939.

[38] A. Radulescu, M. Howard, D. J. Braun, and S. Vijayakumar, “Exploiting variable physical damping in rapid movement tasks,” in *2012 IEEE/ASME International Conference on Advanced Intelligent Mechatronics (AIM)*, Kaohsiung, Taiwan: IEEE, Jul. 2012, pp. 141–148. doi: 10.1109/AIM.2012.6265889.

[39] Chee-Meng Chew, Geok-Soon Hong, and Wei Zhou, “Series damper actuator: a novel force/torque control actuator,” in *4th IEEE/RAS International Conference on Humanoid Robots, 2004.*, Santa Monica, CA, USA: IEEE, 2004, pp. 533–546. doi: 10.1109/ICHR.2004.1442669.

[40] L. Chen *et al.*, “Optimal control for maximizing velocity of the CompAct™ compliant actuator,” in *2013 IEEE International Conference on Robotics and Automation*, Karlsruhe, Germany: IEEE, May 2013, pp. 516–522. doi: 10.1109/ICRA.2013.6630623.

[41] E. J. Rouse, L. M. Mooney, E. C. Martinez-Villalpando, and H. M. Herr, “Clutchable series-elastic actuator: Design of a robotic knee prosthesis for minimum energy consumption,” in *2013 IEEE 13th International Conference on Rehabilitation Robotics (ICORR)*, Seattle, WA: IEEE, Jun. 2013, pp. 1–6. doi: 10.1109/ICORR.2013.6650383.

[42] D. F. B. Haeufle, M. D. Taylor, S. Schmitt, and H. Geyer, “A clutched parallel elastic actuator concept: Towards energy efficient powered legs in prosthetics and robotics,” in *2012 4th IEEE RAS & EMBS International Conference on Biomedical Robotics and*

Biomechatronics (BioRob), Rome, Italy: IEEE, Jun. 2012, pp. 1614–1619. doi: 10.1109/BioRob.2012.6290722.

[43] D. Shin, X. Yeh, and O. Khatib, “A new hybrid actuation scheme with artificial pneumatic muscles and a magnetic particle brake for safe human–robot collaboration,” *The International Journal of Robotics Research*, vol. 33, no. 4, pp. 507–518, Apr. 2014, doi: 10.1177/0278364913509858.

Chapter 1: Hybrid Haptic Actuation Methods

Hybrid actuators are composed of active energy producing actuators and passive energy neutral or dissipative actuators. Our approach features electromagnetic actuation as the active actuation method due to its wide commercial availability and ease of control. Each hybrid haptic device shown in Fig. 1-3 features a particle brake as the passive actuator of choice because of their low rotor inertia compared to a motor of comparable torque capability. When inactive the user only feels the relatively small inertia of the passive actuator rotor and some latent friction. This makes them a suitable choice as a low impedance actuator. Additionally, a key feature of our hybrid actuation approach is passive actuator feedback. Each of the actuators includes a torque sensor to measure the torque produced by the passive actuator.

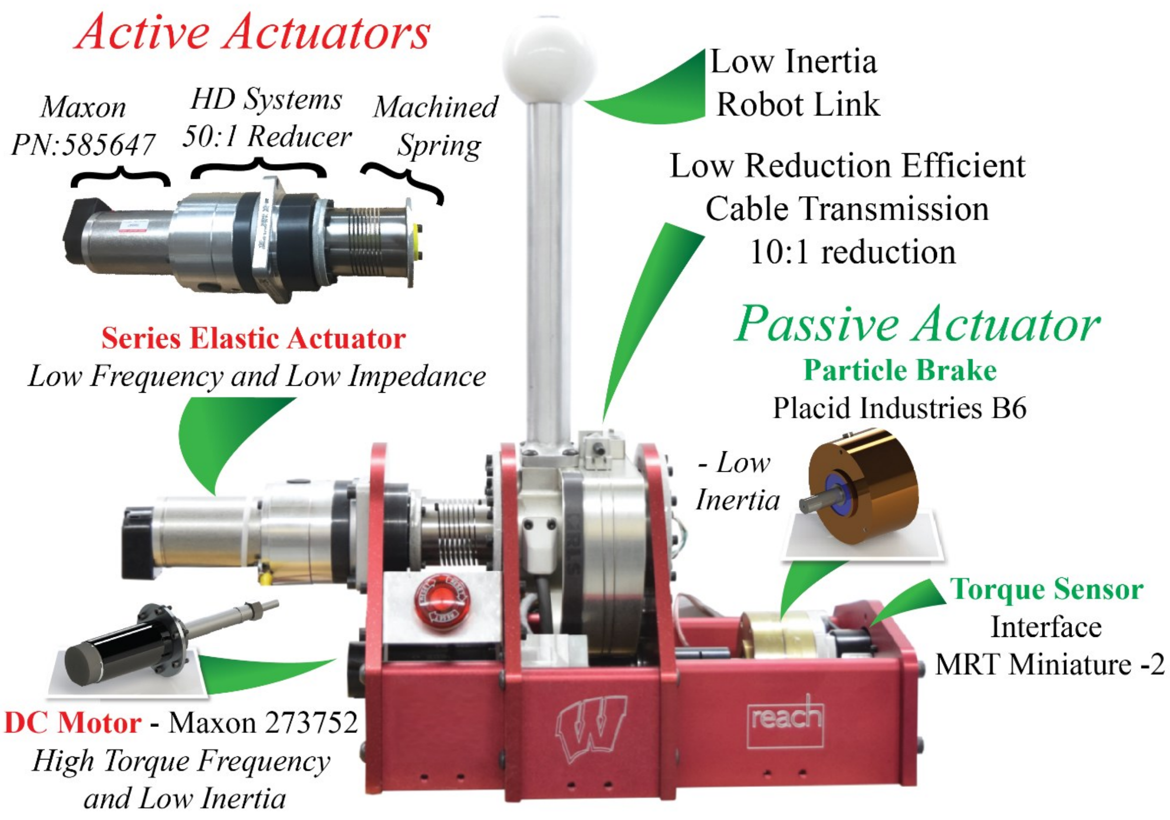

Figure 1: A desktop scale balanced hybrid actuator. The actuator is composed of a Series Elastic Actuator, a small DC motor and a Particle Brake arranged in parallel.

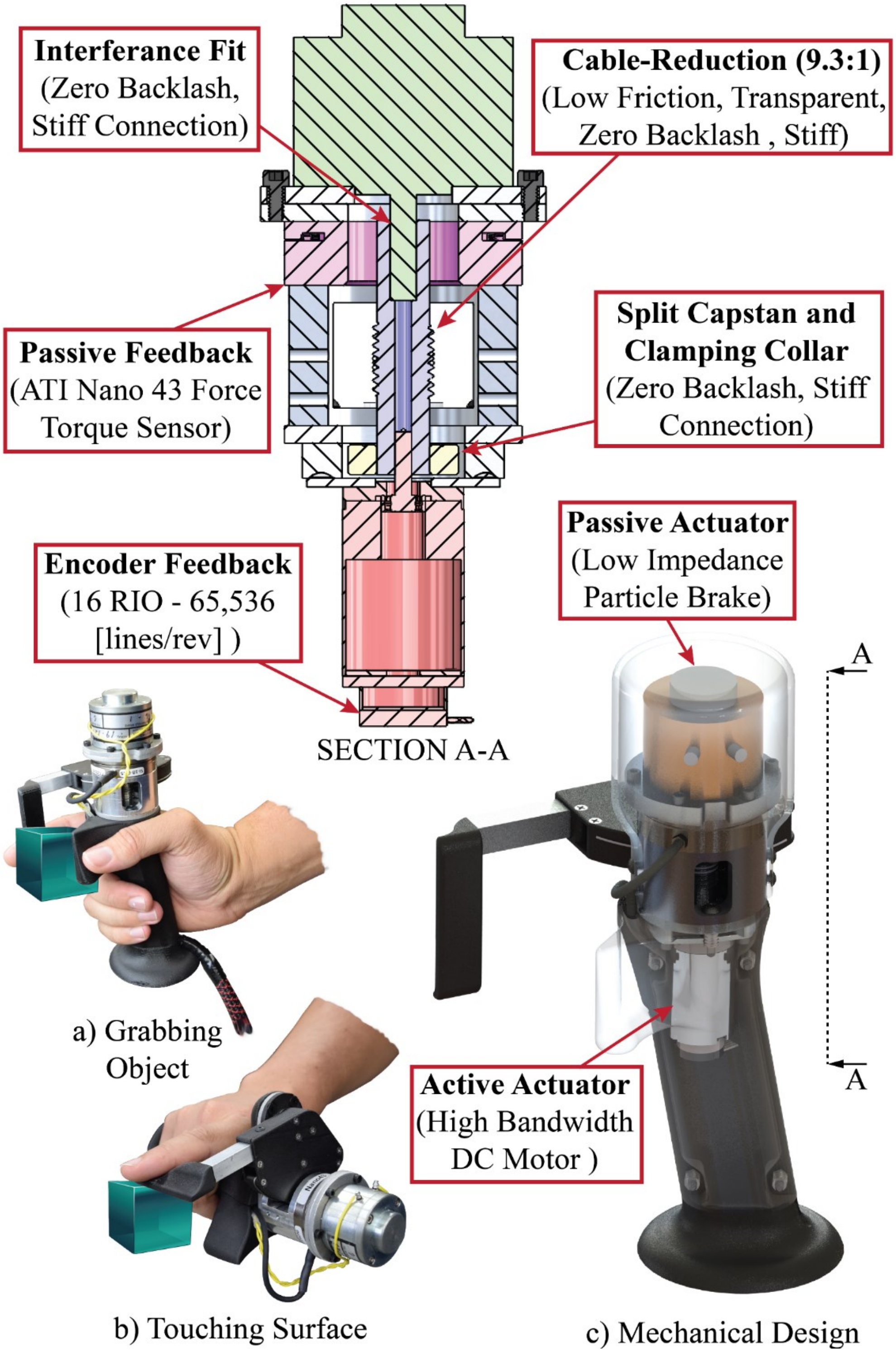

a) Grabbing Object

b) Touching Surface

c) Mechanical Design

Figure 2: A single degree of freedom handheld hybrid actuator. The handheld device uses the parallel hybrid actuation approach a) A grabbing gesture possible with the design b) A touching gesture where the thumb rest is not used. c) The mechanical design of the handheld device

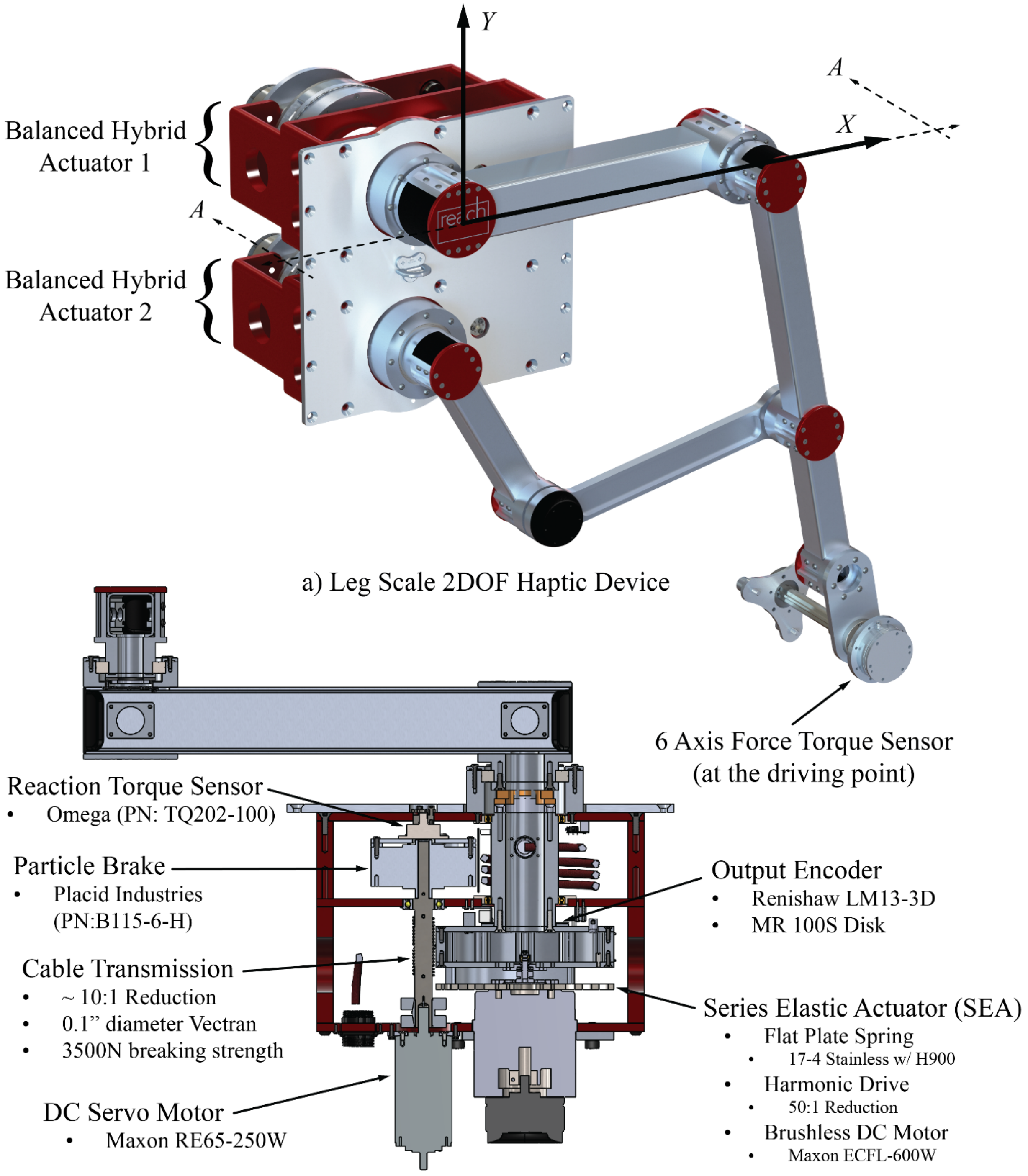

a) Leg Scale 2DOF Haptic Device

b) Large Scale Actuator Section A-A

Figure 3: A two degree of freedom human leg scale balanced hybrid device. Actuators provide greater than 100 Nm capability per actuator. a) Device overview showing coordinate frame. b) Section view of an individual actuator with parts breakdown.

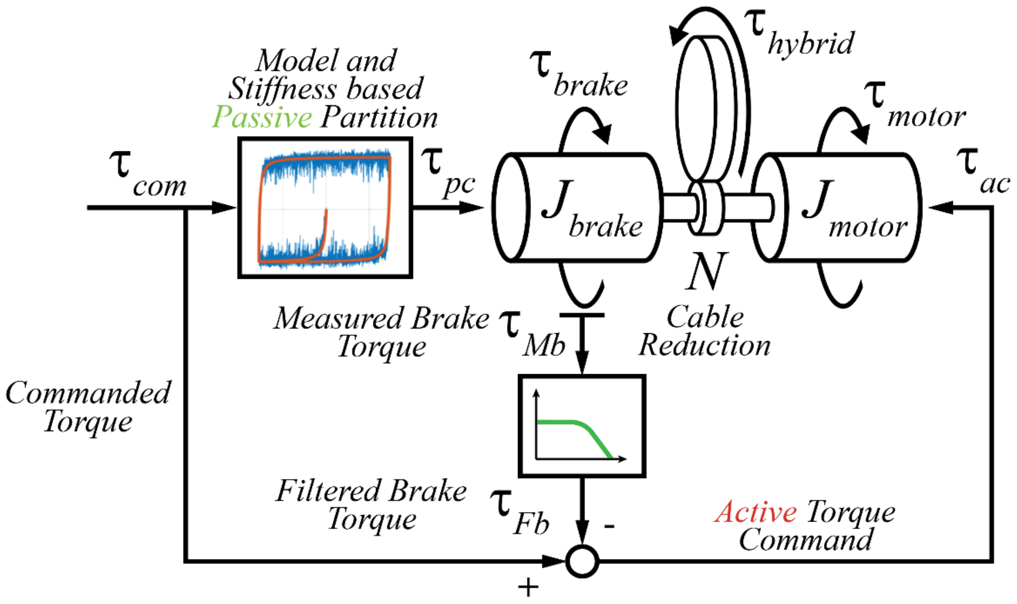

Figure 4: A conceptual view of the single degree of freedom parallel actuation topology. The topology is used for both balanced hybrid actuation and parallel hybrid actuation. In the case of balanced hybrid actuation, the active portion is composed of the SEA and DC motor together.

Fig. 4 shows the general control approach for our hybrid haptic device. Initially, the torque command is fed through a torque partitioning process from which the passive actuator commanded torque is developed. The difference between the measured passive actuator torque and the total torque command is used to form the active actuator's torque command. Measured torque feedback is key to our approach and allows the high bandwidth active portion of the hybrid actuator to compensate for unwanted passive torques and to produce torque the passive actuator cannot.

A. Handheld Hybrid Haptic Actuation.

Small scale haptic devices have traditionally used active actuators which are paired with low reduction (approximately 10:1) extremely efficient cable transmissions. Careful design of these transmissions allows for simple DC motors to provide sufficient active force and torque while preventing excessive increases in reflected inertia, friction, and damping. The low inertia properties of the particle brake allow us to simply connect it directly in parallel with the active portion of the haptic device forming a capable small scale hybrid actuator.

B. Balanced Hybrid Haptic Actuation.

As haptic devices grow in force capability as well as workspace size the actuation force and torque requirements increase significantly. Traditionally in robotics this need for higher forces is addressed with the use of high reduction speed reducers. Unfortunately for haptic devices, increases in gear ratio increase the reflected inertia of the actuator with the gear ratio squared while only proportionally increasing the actuators active torque capability. Haptic devices using large gear reductions and simple open loop active control methods result in devices where the reflected inertia of the active actuator dominates the rendering resulting in poor haptic performance. If the reduction ratio is kept to a minimum as in small scale devices a significant mismatch between passive and active actuator force and torque capability quickly becomes evident as devices scale into larger haptic devices.

To address this need we developed the balanced hybrid actuation concept and control approach which combines high-power, low-impedance active compliant actuation (series-elastic actuator) with high-force passive actuation in parallel with a fast, low-power secondary active actuation. In general, the inclusion of passive actuation provides high stiffness passive rendering capabilities, aids in control stabilization and helps to minimize power consumption, while the inclusion of the active compliant actuation provides high-force active rendering capabilities and low output impedance. The combined active-passive hybrid system provides equivalent passive and active force and power output. The fast secondary actuator addresses the slow response speeds of both the passive and the active compliant actuation. The combination of active and passive actuation can help realize the advantages of both and aid in overcoming drawbacks associated with each actuator. The passive actuator can extend the stable rendering range while feedback of passive torque error to the active actuation can reduce the sticky-effect and non-linear hysteresis associated with passive actuation techniques. Fig. 4 shows a schematic representation of the actuation approach and Fig. 1 and 3 show a desktop and human scale haptic device utilizing the approach.

C. Single Degree of Freedom Hybrid Control Approach

Both the balanced hybrid actuation and handheld hybrid actuation approaches work well in a single degree of freedom device if sufficient passive feedback bandwidth is present, and latency is eliminated in the controller when providing active torques or forces. However, this can be difficult to achieve in practice due to sensor noise, unwanted transmission dynamics, or time delays. To help mitigate this difficulty we developed several torque partitioning strategies to enable seamless operation of the hybrid actuator.

1.Particle Brake Dynamics

An essential part of our proposed model-based passive actuator partitioning approach is the development of an accurate passive actuator physical model. To motivate our modeling approach, it is instructive to discuss the specifics of the passive actuator's design. In our work, we have used a particle brake, shown in Fig. 5, which can produce controllable passive torques when current is passed through a coil generating an electromagnetic field. The field binds the rotor and stator together via ferrous metal particles and resulting torques resist motion of the rotor. Steady-state brake torque increases with increasing current and is a function of displacement. At large position oscillation amplitudes coulomb friction is a good approximation of the brakes torque response and energy dissipation. However, closer examination of the measured brake torque vs. position relationship, Fig. 6, shows a more continuous transition in torque during velocity reversal conditions.

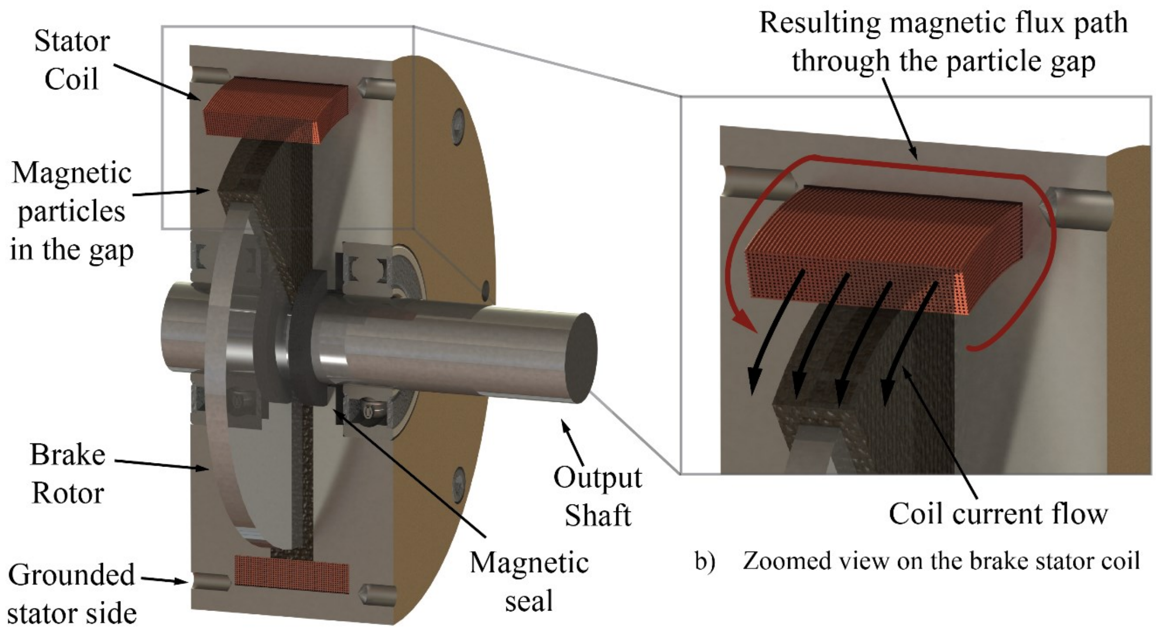

a) Magnetic Particle Brake Cutaway View

b) Zoomed view on the brake stator coil

Figure 5: Components and function of a particle brake. a) Cross section of a particle brake showing rotor and stator and magnetic particles filling the gap between them. b) Zoomed view of the stator coil showing the flux lines passing through the particle gap when energized locking the rotor and stator together.

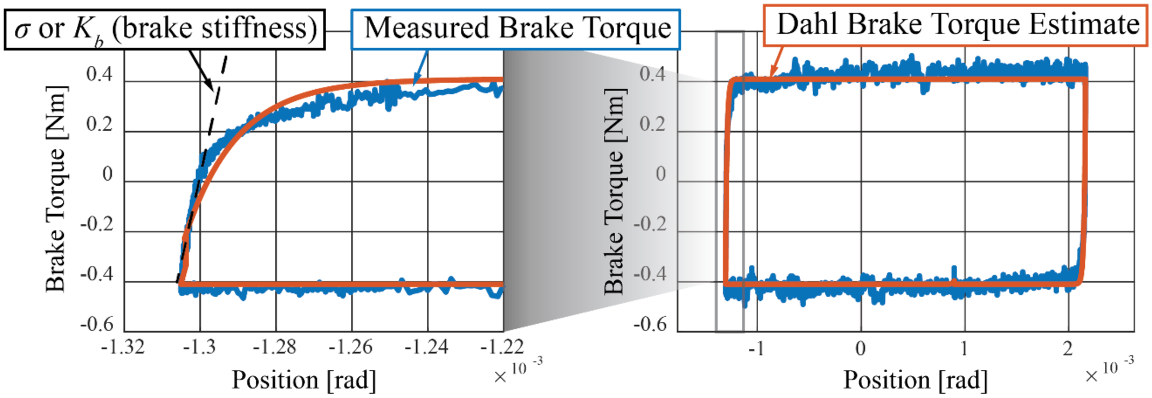

a) Zoomed view of brake velocity reversal

b) Brake response at constant current

Figure 6: Measured brake torque values compared to the Dahl friction brake model. a) Zoomed plot showing spring like transition dynamics. b) Running friction showing behavior akin to Coulomb friction.

Our experiments show the brake is able to store energy and under small deflections and can behave more like a spring than a purely dissipative system. This behavior is akin to structural damping observed in bolted joints [1] and bearing friction. Taking inspiration from these sources we developed a modified Dahl friction model to describe the torque production and mechanical hysteresis of our brake under velocity reversal conditions [2]. A graphical comparison of measured brake torque and rotor position data can be seen in Fig. 6.

In addition to mechanical behavior, particle brake electrical dynamics limit the change of current in the coil and influence torque production in the brake. Particle brakes also display a nonlinear and hysteretic relationship between current flowing in the coil and steady state output torque. The complete brake mathematical model is described in detail in Appendix A.

2.Model Based Passive Partitioning

Our passive partitioning method, shown in Fig. 4 and 7, utilizes our particle brake model to estimate particle brake torque. Both electrical dynamics and mechanical hysteresis effects are important to produce a useful estimate of brake torque production.

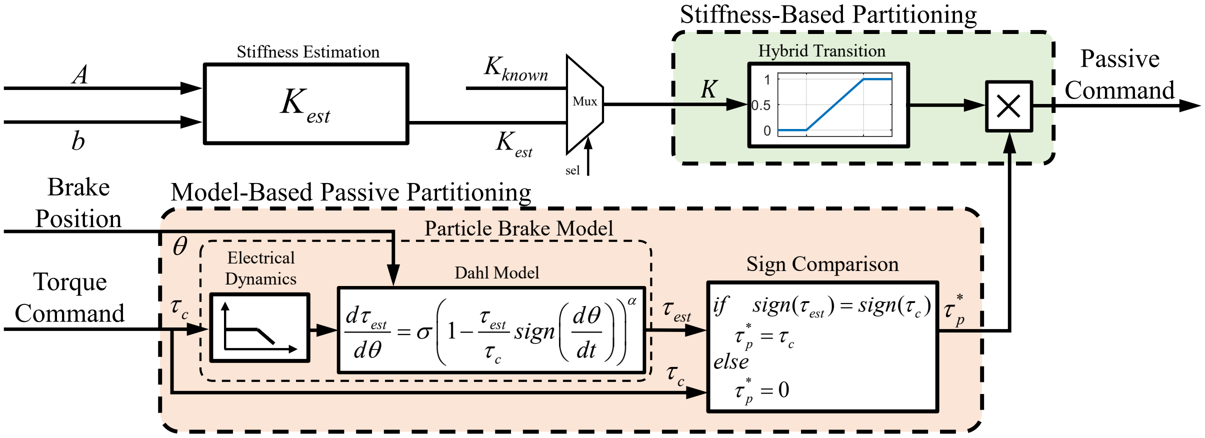

Figure 7: Model based, and stiffness based passive partitioning. Model based passive partitioning helps to remove unwanted brake torques and stiffness based passive partitioning prevents sticking while the actuator is operating at low stiffness.

The torque command and brake position are the inputs to the brake dynamic model whereas the estimated brake torque is the model's output. If the open loop brake torque estimate is of the same sign as the commanded torque, indicating that the commanded torque is physically feasible given the brake's current state, then the commanded torque is sent to the brake.

Our method of partitioning the actuator's commanded torque has several advantages over methods assuming purely dissipative passive actuator torques. First, power based partitioning methods have problems at zero or near zero velocity. In discrete systems with finite velocity resolution power-based partitioning can produce rapid switching at or near the sample frequency of the discrete time controller. This can cause chattering in the passive actuators rendered torque and affect the rendering of a haptic device without other mechanical or software provisions [13,15]. Single degree of freedom passive torque commands obtained with our open loop model do not display the same switching behavior as seen in Fig. 8. Additionally, the passive actuator is able to produce zero velocity passive torque in a single degree of freedom operation. Finally, our passive partitioning method accounts for strain energy stored in the brake. Accounting for this has distinct advantages while the hybrid device is operating at high stiffness where energy stored in the brake plays a significant role in the dynamics of the device.

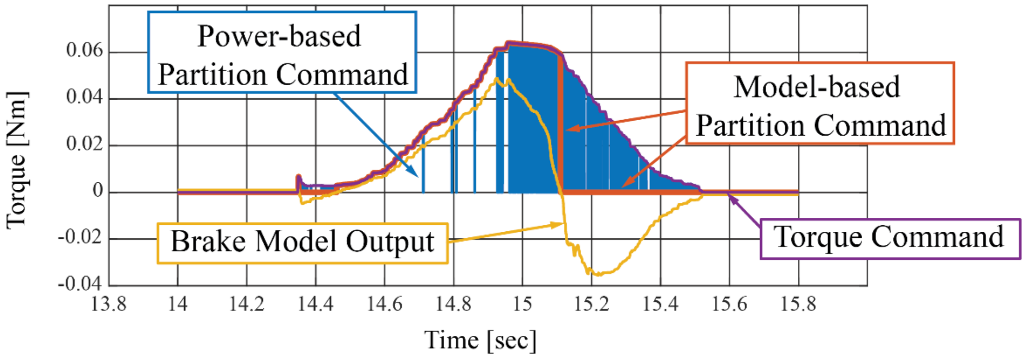

Figure 8: Output of model based passive partitioning. Model based passive partitioning prevents switching behavior seen in power-based passive partitioning methods resulting from quantization.

3.Stiffness Based Partitioning

While our device is producing a high stiffness our torque partitioning method works well and the device produces impressive high impedance renderings. An example of the desktop devices performance while rendering a high impedance of (170.5 [N/mm]) can be seen in Fig. 9. For reference we compare the hybrid devices performance to the active only (macro-mini) system at its virtual stiffness stability limit. We attribute this to the behavior of the particle brake at small deflections. Our partitioning approach allows the brake to behave like a physical spring in parallel with the active actuator.

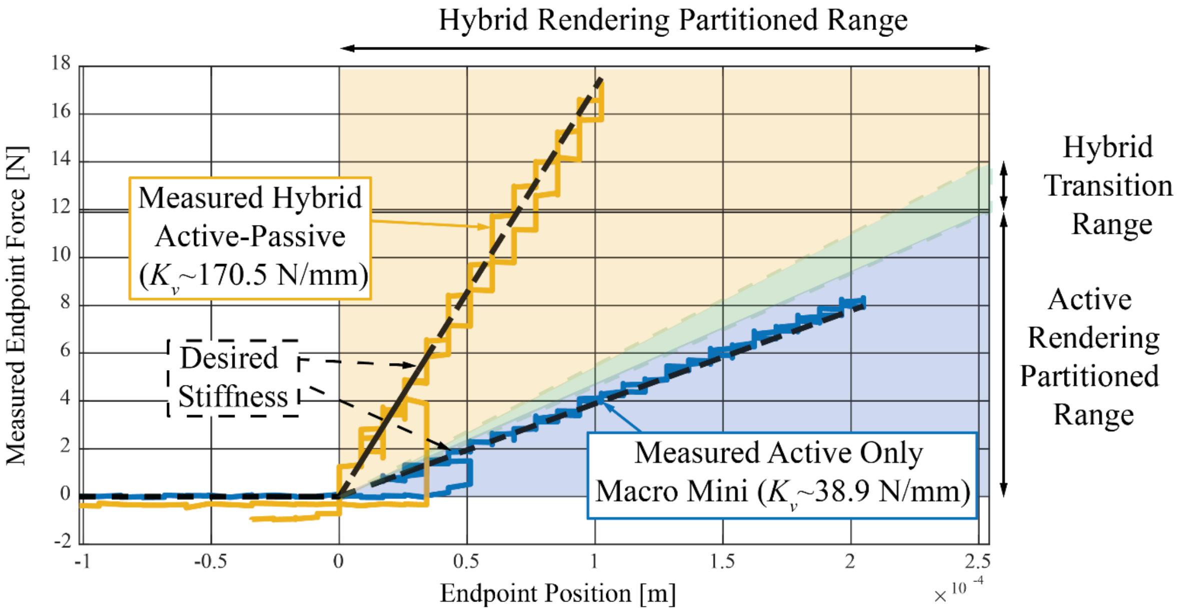

Figure 9: Hybrid vs active only rendering comparison. The shaded blue area represents the hybrid rendering region after stiffness based passive partitioning. Active only renderings are used during low stiffness renderings. Dashed green lines represent the edges of the transition from active only low stiffness rendering to hybrid high stiffness rendering.

However, large position oscillation amplitudes are often encountered at low stiffness and the hybrid actuator begins to display undesirable effects where the device feels as if it is lagging upon velocity reversals. This behavior can be shown with output force measurements in Fig 10.

Active actuators like the DC motor and SEA comprising half of our hybrid actuator are capable low stiffness and impedance actuators. Consequently, we choose to utilize only the active portion of our hybrid actuator while rendering low impedances. Utilizing the active actuator at low stiffness prevents particle brake sticking. Our control structure, enables a smooth transition between active only and hybrid operation, can be seen in Fig. 7 and 9. In practice we set hybrid transition points from low stiffness active-only rendering to high stiffness hybrid rendering at a stiffness where sticky walls are no longer observed. In most haptic applications the rendered stiffness or more broadly the rendered impedance is known and could be supplied as part of the control algorithm. However, in applications where the virtual environment stiffness is not known apriori an online estimation approach can be adopted (see Appendix B)

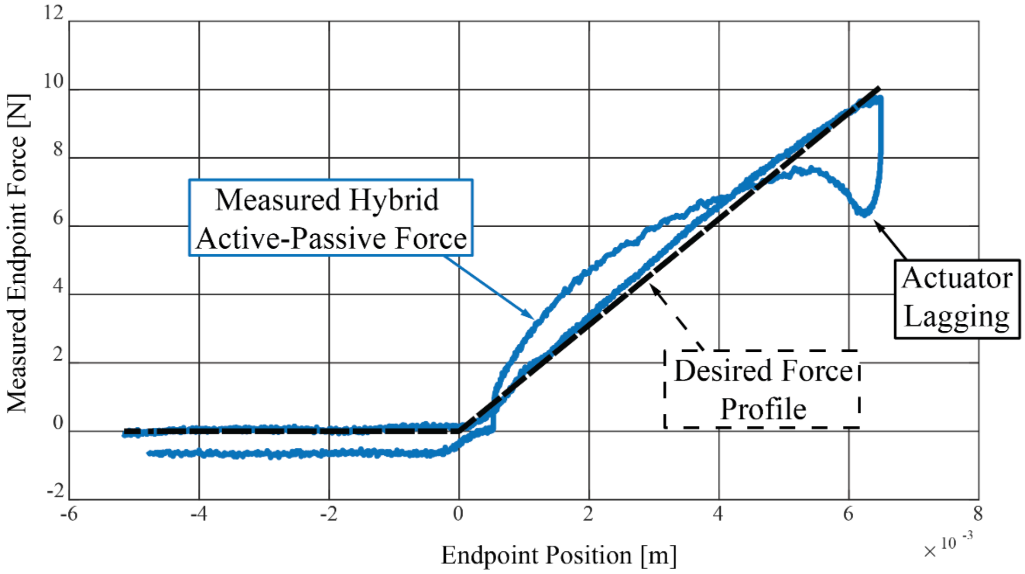

Figure 10: Low stiffness hybrid actuation rendering errors. Errors become apparent when using the hybrid actuator at low stiffness. The lagging rendering errors are mitigated through stiffness based passive partitioning. Stiffness based passive partitioning allows us to use the active actuator at low stiffness and transition to the hybrid actuator for high impedance rendering removing the hybrid actuation rendering errors in single degree of freedom systems.

D. Multiple Degree of Freedom Hybrid Control Approach

Our parallel hybrid control approach is fundamentally a joint space torque control approach. If sufficient passive feedback bandwidth is present and latency is eliminated in the controller the approach works well. While high bandwidth passive feedback can improve rendering quality, achieving it can be challenging and perhaps undesirable from a stability standpoint.

Just as multiple degree of freedom purely passive systems produce notable vibrations sliding along surfaces, hybrid haptic devices can create rendering defects when actuation effort is needed from both actuators to produce a force [5]. Rendering defects while producing coupled constraints are especially noticeable when passive feedback bandwidth is limited or distorted. Fortunately, an easy solution is possible to remedy this problem. Removing low frequency content from the passive commands allows for smooth sliding along virtual constraints even when only finite passive actuator feedback is available. This method removes the attractive force generation benefits of DC passive torques. However, it preserves much of the stabilizing effect of the passive actuator while eliminating vibrations observed while sliding along constraints shown in Fig 11.

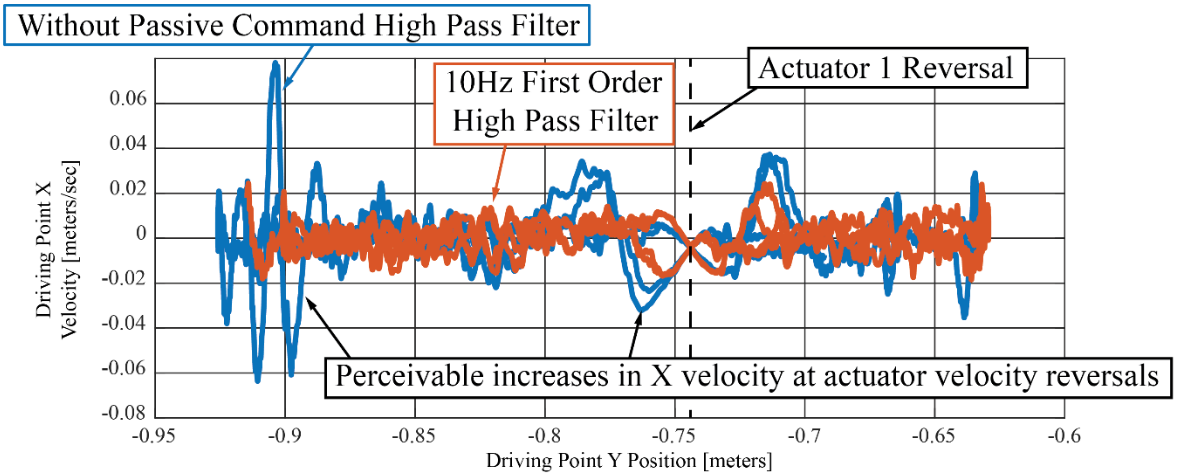

Figure 11: Multiple degree of freedom sliding rendering comparison. The multiple degree of freedom hybrid system shows distortion when sliding along a stiff wall. The control system when adding a high pass filter shows less distortion and the virtual constraint becomes smooth.

The consequence of this method is that active actuators must supply the DC content of the virtual environment. In our approach we accomplished this by simply adding a high pass filter to our actuation level control method shown in Fig. 12 and a comparison between the passive torques produced with and without the high pass filter can be seen in Fig 13 A and B. The distortion before implementing a high pass filter is especially noticeable where actuators are required to reverse velocity while supplying a near constant torque as is common in haptic tasks like sliding along a virtual constraint. Fig 11 and 12 shows this velocity reversal and the resulting distortion both at the end of a sliding motion and in the middle of a sliding motion where actuator 2 must reverse velocity due to the device kinematics.

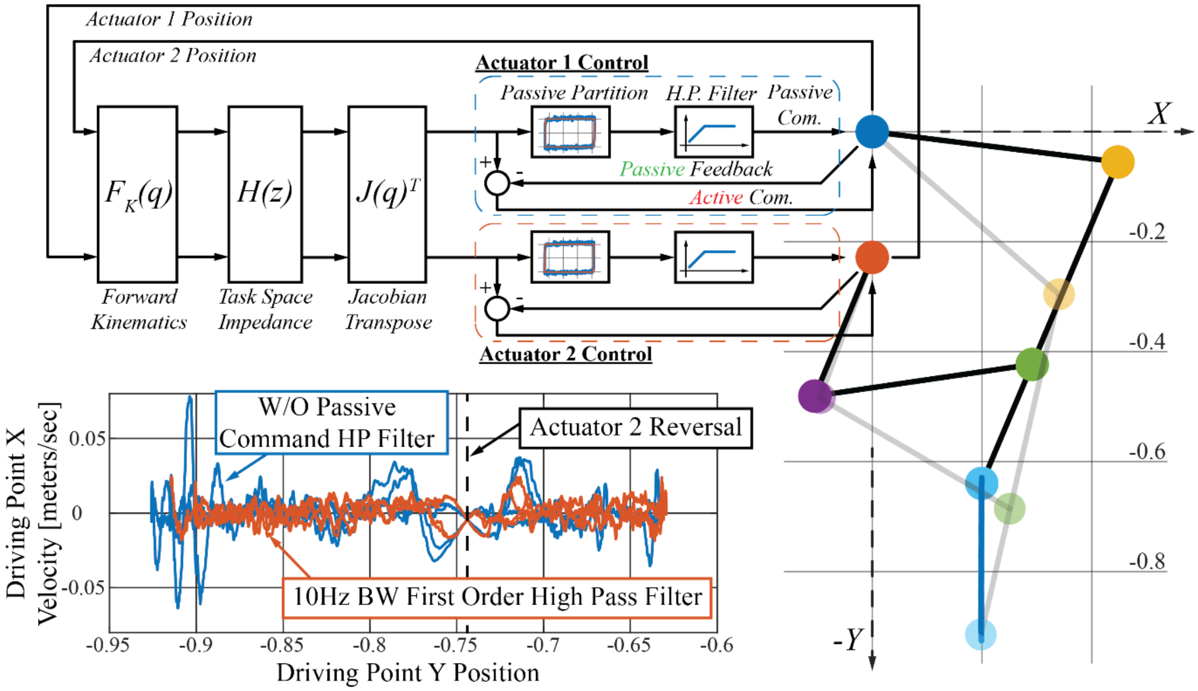

Figure 12: Multiple degree of freedom control method. The multiple degree of freedom hybrid system relies on joint level torque control outlined in prior sections and the addition of a high pass filter to fit into a typical multi degree of freedom impedance control loop. Forward kinematics transform joint states into task space driving point states. Driving point state estimates are used to generate endpoint forces which are transformed back into joint torques with the basic Jacobian.

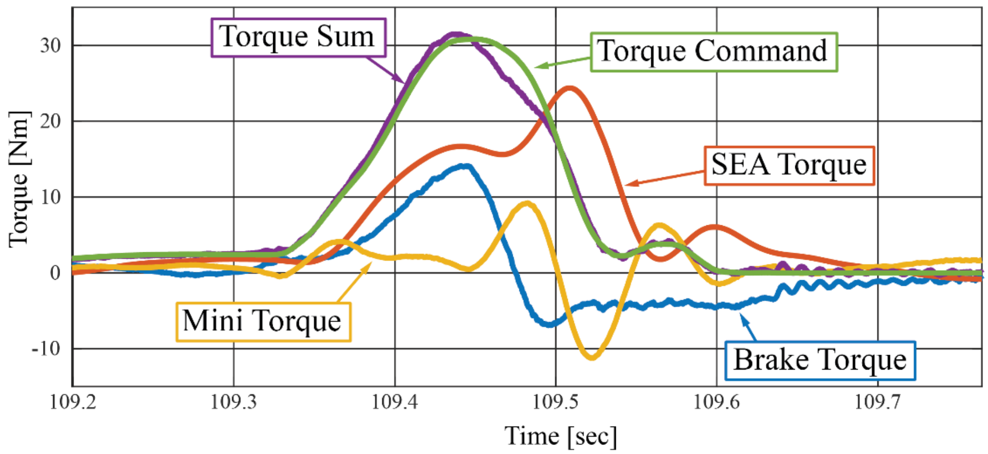

a) The high pass filtered version of the passive partitioning method

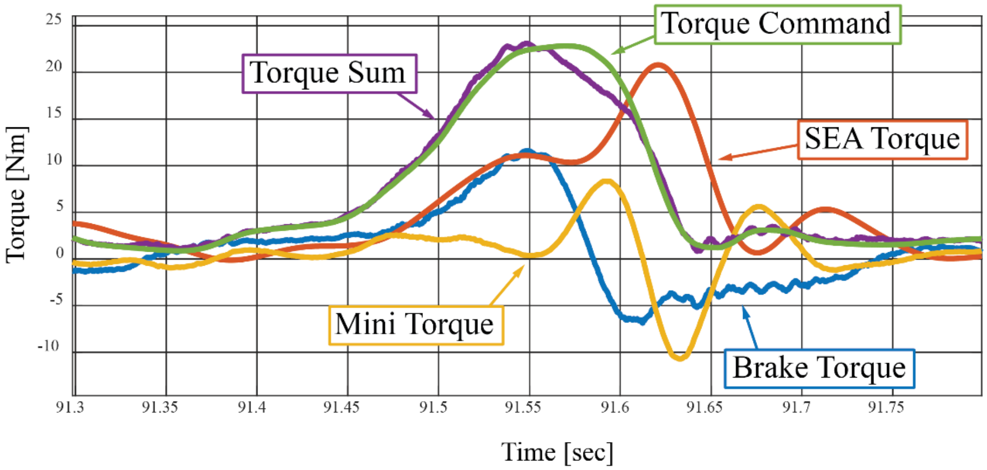

b) The torque interaction signals from actuator 2 without a high pass filtered implemented

Figure 13: Multi degree of freedom high pass filter comparison. The high pass filtered and unfiltered actuation torques from actuator two when pushing against the multiple degree of freedom virtual constraint shown in Fig. 12. Interactions show minimal differences when interacting transiently with the virtual constraint. This comparison shows that the high pass filter is effective at removing rendering defects while preserving much of the passive actuators beneficial torques during transient events like tapping a wall a) The filtered version of the transient pressing interaction b) A similar baseline interaction without a high pass filter implemented.

Multiple degree of freedom hybrid control is simple due to our actuator level control methods and directly mirrors a typical active haptic devices control system. Fig. 12 shows the method where forward kinematics relate joint space measurements to the devices driving point. A task or operational space control law relates the driving point motions to desired forces and torques. Finally, the commanded forces and torques are transformed back into joint space torque commands with the basic Jacobian and are executed by each hybrid actuator.

References

[1] B. J. Deaner, M. S. Allen, M. J. Starr, and D. J. Segalman, "Investigation of Modal Iwan Models for Structures with Bolted Joints," in *Topics in Experimental Dynamic Substructuring, Volume 2*, R. Mayes, D. Rixen, and M. Allen, Eds., in Conference Proceedings of the Society for Experimental Mechanics Series. , New York, NY: Springer New York, 2014, pp. 9–25. doi: 10.1007/978-1-4614-6540-9_2.

[2] `P. R. Dahl, "Solid Friction Damping of Mechanical Vibrations," *AIAA Journal*, vol. 14, no. 12, pp. 1675–1682, Dec. 1976, doi: 10.2514/3.61511.

[3] Jinung An and D.-S. Kwon, "Five-bar Linkage Haptic Device with DC Motors and MR Brakes," *Journal of Intelligent Material Systems and Structures*, vol. 20, no. 1, pp. 97–107, Jan. 2009, doi: 10.1177/1045389X07086690.

[4] M. Antolini, O. Kose, and H. Gurocak, "A first order transfer function to balance the workload in brake-motor hybrid actuators," in *2014 IEEE Haptics Symposium (HAPTICS)*, Houston, TX, USA: IEEE, Feb. 2014, pp. 509–514. doi: 10.1109/HAPTICS.2014.6775508.

[5] J. E. Colgate, M. A. Peshkin, and W. Wannasuphoprasit, "Nonholonomic haptic display," in *Proceedings of IEEE International Conference on Robotics and Automation*, Minneapolis, MN, USA: IEEE, 1996, pp. 539–544. doi: 10.1109/ROBOT.1996.503831.

Chapter 2: Hybrid Actuator Passivity

Analyzing the stability of the hybrid actuator highlights the mechanisms that extend and limit the actuator's rendering performance. In this section, we consider the effects of the zero order hold inherent to discrete time controllers, along with the brake's dynamics, time delay, and velocity filtering but ignore the effect of brake measurement filtering (filtered feedback), which will be considered in Chapter 3.

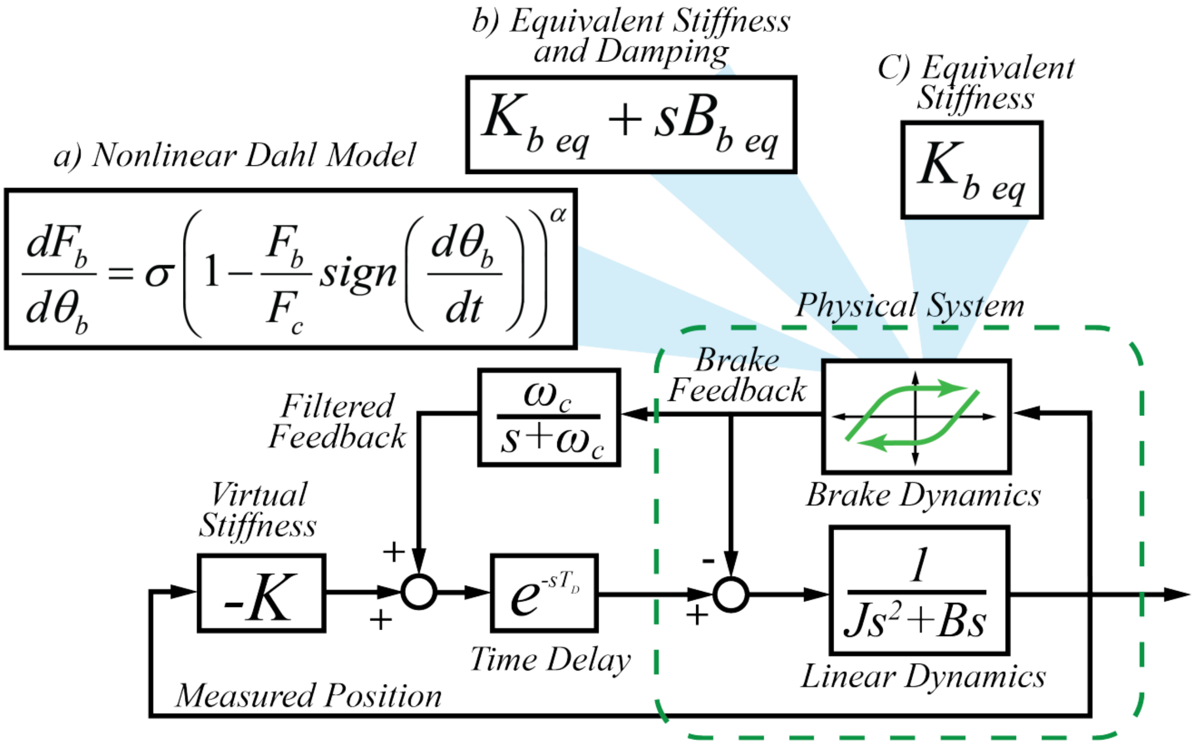

Figure 1: Single degree of freedom control loop with simplified brake models. The full Dahl friction model of the brake is simplified to an equivalent stiffness and damping or just an equivalent stiffness at small amplitudes. a) The full nonlinear Dahl friction-based brake model. b) The simplified equivalent stiffness and damping model c) The small amplitude equivalent stiffness model of the particle brake. The full equivalent stiffness and damping methodology is shown in Appendix C.

While the full brake model developed in the previous chapter describes the behavior of the particle brake's electrical dynamics and physical dynamics across a large range of position oscillation amplitudes, our hybrid actuator often only functions over small deflections. This is especially true when operating on the edge of stability (at high loop gains). The brake is generally "locked" or energized to its saturation limit when operating in this regime. In these situations, the brake is only deflecting small amounts and responds approximately as a spring as shown in Fig. 2.

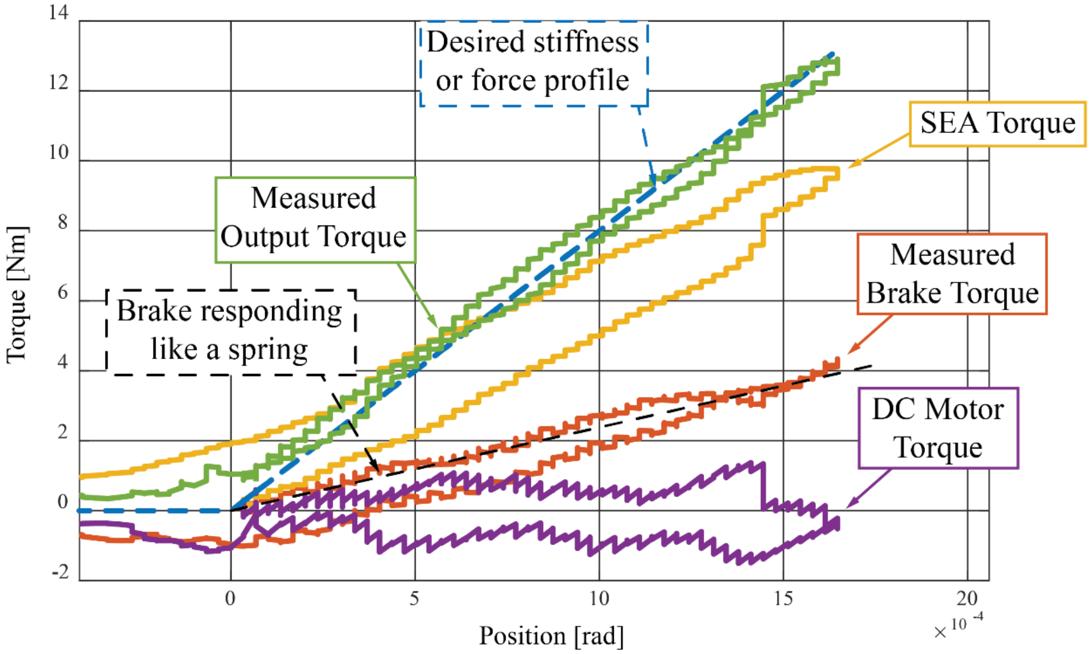

Figure 2: High gain virtual stiffness interaction. Each of the torque components of the hybrid actuator are shown against actuator deflection. The passive actuator responds approximately as a pure stiffness which agrees with the equivalent stiffness and damping analysis from Appendix C.

Further study in Appendix C of the Dahl friction model confirms these experimental results and indicates that the particle brake functions as a pure stiffness while operating at small deflections as seen during high stiffness and high gain interactions. Consequently, we simplify our particle brake model into a pure physical stiffness for the purpose of analyzing the stability properties of our hybrid actuator.

A. Hybrid Actuator Discrete Time Virtual Stiffness Passivity.

Considering the system shown in Fig. 1, where the brake is approximated by an equivalent stiffness, we can evaluate the stability of the system using passivity as a stability criterion. Passivity stems from the study of what are known as dissipative or positive real systems [1]. The formal definition of a passive system is shown in (1).

$$\int_0^t f(\tau)v(\tau)d\tau + E(0) \geq 0 \quad \forall f(\cdot), v(\cdot) \quad \forall t \geq 0 \tag{1}$$

Variables *f* and *v*, force and velocity respectively, are conjugate power variables describing energy flow in the system and *E(0)* is the energy stored in the system at $t = 0$. Applying (1) to a one-port system, such as a single degree of freedom haptic device, implies that a system will be passive if the integral of power extracted from the system over time does not exceed the initial energy of the system [2].

Showing a dynamic system to be passive is useful because of the stability guarantees which go along with it. Network theory states that feedback combinations of stable passive systems are also stable and passive. In kinesthetic haptics the device is physically interacting and conveying feelings to a user which is "coupled" to the haptic device. The interactions between the human and device can be viewed as a feedback interconnection of two systems. People have been shown to be skilled at approximating a passive system and are often considered to be passive [3]. Thus, designing a haptic device to be passive allows one to apply network theory to the interactions between a human and device and ensure stability. Simply analyzing the haptic device and showing it to be passive (ignoring the human environment) ensures the device will be stable when interacting with the operator and any other passive environment.

Passivity can be shown in a discrete time system by showing the system will dissipate energy over each sample period. As in [2] comparing an ideal physical spring mass system (which will always remain passive) to our hybrid haptic device provides a simple method to analyze the range of passive virtual stiffness our hybrid actuator can produce. If the two systems shown in Fig. 3 share the same rendered stiffness K_v and inertia M, bounding the difference in energy between the ideal system and haptic device over any sample time defines the range of achievable passive virtual stiffness.

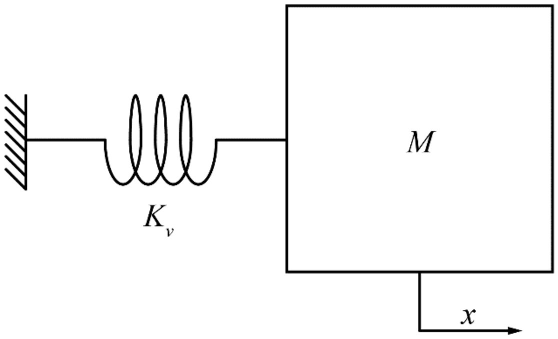

a) The ideal passive physical spring mass system

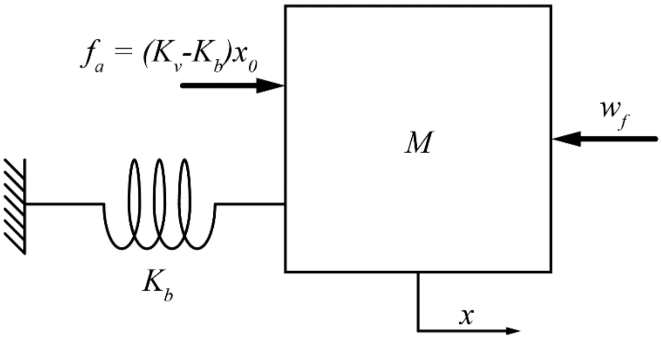

b) Schematic representation of the hybrid actuators physical system

Figure 3: A schematic representation of an ideal spring damper and our hybrid actuator. a) An ideal physical spring mass system with a physical spring of the same stiffness as the desired virtual stiffness (K_v) that the haptic device is trying to reproduce and that by definition must be passive. b) The schematic representation of our hybrid actuator with the spring model of the brake (K_b), non-conservative damping forces acting upon the system (w_f), and the latched force input from the active actuator(f_a).

We begin our analysis by calculating the energy extracted from the ideal system over a single sample time which is simply the sum of potential and kinetic energy (2).

$$w_2 = \frac{1}{2}K_v(x_0^2 - x_T^2) + \frac{1}{2}m(\dot{x}_0^2 - \dot{x}_T^2) \qquad (2)$$

In (2) the first term quantifies the potential energy stored in the ideal version of the physical spring. The second term represents the kinetic energy in the system's mass. Variables x_0 and x_T are the devices position at the beginning and end of the considered sample period. Additionally, $\dot{x}_0$ and $\dot{x}_T$ are the systems velocity at time zero and at the sample time T respectively. We can write the work a single degree of freedom hybrid device does on the environment or human operator in (3).

$$w_1 = f_a(x_0 - x_T) + \frac{1}{2}m(\dot{x}_0^2 - \dot{x}_T^2) + \frac{1}{2}K_b(x_0^2 - x_T^2) - w_f \qquad (3)$$

In (3) the first term represents the work done by the active actuator of the device where f_a is the active actuator's constant latched force value over a sample period. Again, the second term is the kinetic energy of the device due to inertia m. The third term is the stored potential energy internal to the passive actuator. In this case the brake is locked and is modeled as a physical stiffness K_b. Finally, w_f represents non-conservative forces like friction and damping in the hybrid device.

For simplicity, we only consider linear damping in this analysis. In [2] the Cauchy-Schwarz inequality provides a lower bound on the energy dissipated by linear damping b over a sample period (4).

$$w_f = \int_0^T bx^2 dt \geq \frac{b}{T}(x_T - x_0)^2 \qquad (4)$$

Finally, we recognize that our hybrid haptic control law for virtual stiffness is simply the difference between the desired virtual stiffness force and the measured brake force $(K_v\text{-}K_b)x_0$. Forming (5) quantifies the difference between the minimum energy produced by the hybrid device and the ideal spring mass system and results in (6) after canceling inertial terms.

$$J = w_2 - w_1 \tag{5}$$

$$J \geq \frac{1}{2}K_v(x_0^2 - x_T^2) - \left((K_v - K_b)x_0(x_0 - x_T) + \frac{1}{2}K_b(x_0^2 - x_T^2) - \frac{b}{T}(x_T - x_0)^2\right) \tag{6}$$

Expanding and rearranging (6) yields the quadratic (7).

$$J \geq \left(\frac{b}{T} + \frac{K_b}{2} - \frac{K_v}{2}\right)(x_0 - x_T)^2 \tag{7}$$

It follows that *J* can only be greater than zero (the system remains dissipative and passive) if the quadratics coefficient is greater than zero. This leads to (8) which bounds the maximum passive virtual stiffness the hybrid device can produce.

$$K_v \leq \frac{2b}{T} + K_b \tag{8}$$

Several insights into the stability of the system are gained through this simplified analysis and are summarized below:

1. ***Brake stiffness, K_b, is an important factor*** in determining the range of passive virtual stiffness our hybrid device is capable of rendering, and a higher brake stiffness directly increases the maximum passive virtual stiffness.
2. ***No physical damping, b, is needed*** to passively render virtual stiffness up to the brake's stiffness and the device is dissipative for virtual stiffness less the brake stiffness. Just as "energy leaks" occur in an active device [4,5], ***"energy sinks" are possible*** in our hybrid device when the active portion renders a negative stiffness to negate unwanted physical passive torques. In this case the ***effects of the zero order hold are reversed*** (due to the effective negative active actuator rendered stiffness).
3. The range of virtual stiffness reduces to the brake stiffness as sample time increases. The system is ***passive independent of sample time*** for virtual stiffness up to the brake stiffness.

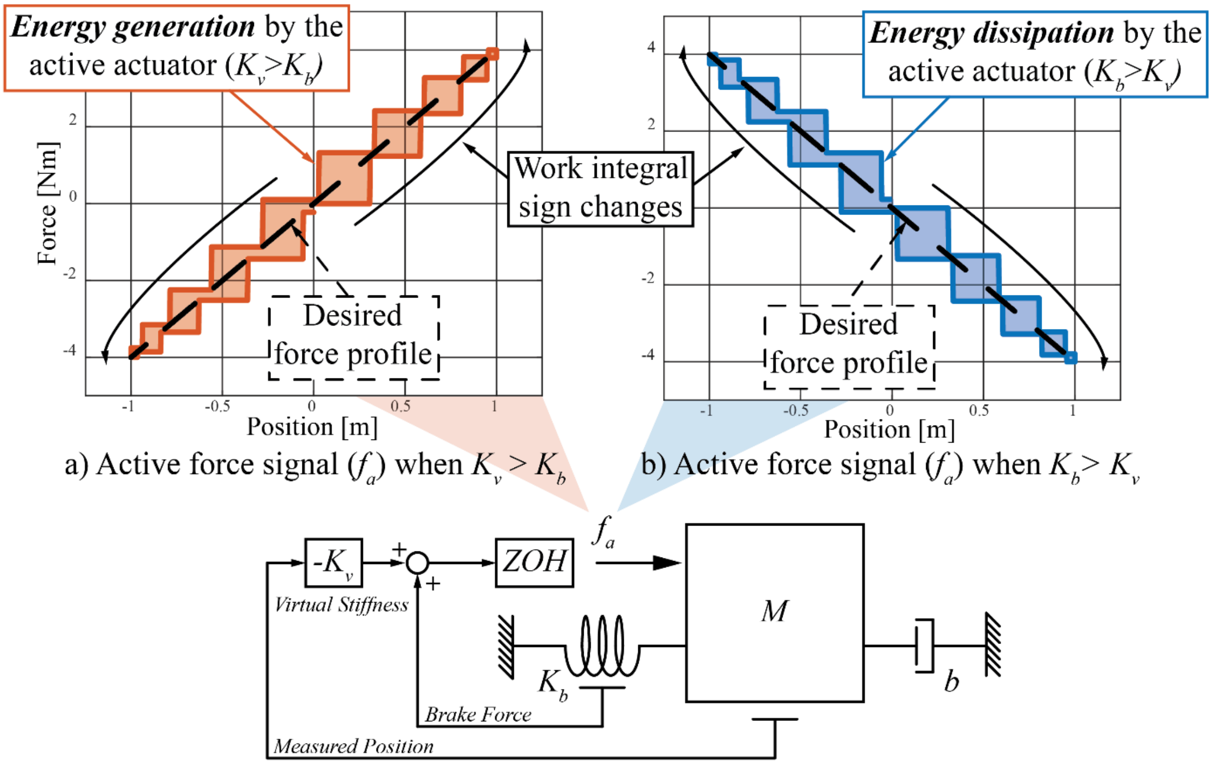

a) Active force signal (f_a) when $K_v > K_b$

b) Active force signal (f_a) when $K_b > K_v$

c) Functional Block diagram of the Actuator

Figure 4: Work integrals of the active actuators above and below the brake stiffness. a) The resulting work done by the active actuator when the desired stiffness is greater than the brake stiffness b) The same work integral reversing direction if the desired stiffness is less than the brake stiffness resulting in an “energy sink”. c) A functional block diagram of the actuator.

An intuitive explanation for the stability results emerges when considering (8). The parallel actuation topology allows the actuator to substitute physical stiffness for virtual stiffness thereby expanding the range of passive stiffness. This happens when the desired virtual stiffness is greater than the brake stiffness as in Fig. 4a. In this situation the brake stiffness expands the range of the device by rendering a portion of the virtual stiffness. However, energy generation or “energy leaks” proportional to (9) ultimately limits the passive rendering range just as in a normal active only haptic device. Conversely, if the active actuator attempts to cancel the hybrid actuator’s torque

($K_v<K_b$) the device produces an ***"energy sink"*** at a rate proportional to a damper (b_{kb}). This dissipative behavior is shown in Fig. 4b where the work integral of the active actuator reverses direction, and the active device begins to dissipate energy as a result. One might think of this effect as the dynamics of the device and the control system approximating a derivative via a finite difference between two signals in phase with position (i.e. virtual and physical stiffness forces) ultimately generating damping as a result.

$$\frac{T(K_b - K_v)}{2} \approx b_{kb} \tag{9}$$

B. Hybrid Actuator Passivity of Virtual Stiffness and Damping

While the analysis presented in Section A yields many insights into hybrid actuator stability and performance, it lacks versatility and applying the method to a diverse range of virtual impedances can be tedious. For active actuators the inequality (10) first presented in [6] and subsequently in [7] provides a more versatile solution to evaluate the range of passive virtual impedances a device can achieve.

$$\Re\big(Z(j\omega)\big) + \frac{T}{2\big(1 - cos(\omega T)\big)}\Re\{\big(e^{-j\omega T} - 1\big)H\big(e^{j\omega T}\big)\} > 0 \tag{10}$$

$$for\ 0 \leq \omega \leq \omega_n = \frac{\omega_s}{2}$$

Where $\Re(Z(j\omega))$ is the real component of the physical system, $H(e^{j\omega T})$ is the discrete time haptic control law, T is the sample time, ω is the frequency at which the expression is evaluated at, ω_n is the Nyquist frequency, and ω_s is the sampling frequency.

The inequality relates the physical dissipation of a haptic device to the energy created by the device while reproducing a virtual impedance. Traditionally, (10) has been applied to only rigid active devices but it can be applied to our hybrid actuator by recognizing that the physical brake (represented here by a pure stiffness) is not dissipative and does not contribute to the real component of the inequality, thus the real component of our physical system simplifies to the linear damping component. Additionally, as in (6) we recognize that our hybrid haptic control law takes the form of *(K_v-K_b)*. Incorporating a backwards difference velocity estimate and virtual damping B_v into the haptic control law yields (11) and an inequality (12) can be derived from (10).

$$H\left(e^{j\omega T}\right) = (K_v - K_b) + B_v \frac{z-1}{Tz} \tag{11}$$

$$b > \frac{T(K_v - K_b)}{2} - B_v cos(\omega T) \tag{12}$$

The expression (12) is bounded by (13) and with some rearranging yields an expression which bounds the maximum passive virtual stiffness and damping the hybrid device can produce (14).

$$b > \frac{T(K_v - K_b)}{2} + |B_v| \tag{13}$$

$$K_v < \frac{2(b - B_v)}{T} + K_b \tag{14}$$

Focusing on virtual damping alone (15) leads to another insight into how the hybrid actuator functions.

$$B_v < \frac{T}{2} K_b + b \tag{15}$$

In the case where the active actuator is canceling the brakes stiffness it creates an ***"energy sink"*** proportional to damping. This effect (9) ***enables increases in the maximum passive virtual damping*** as the discrete time control system samples more slowly. One might understand this by first recognizing that an active device alone is passive for virtual damping up to the linear damping value. Acknowledging that the hybrid system adds damping at the rate of (9) leads to (15) and the conclusion that the hybrid device is adding dissipation as the sample time increases. This added dissipation leads to increases in the maximum passive virtual damping as compared to the active only device as seen in Fig. 5 and 6.

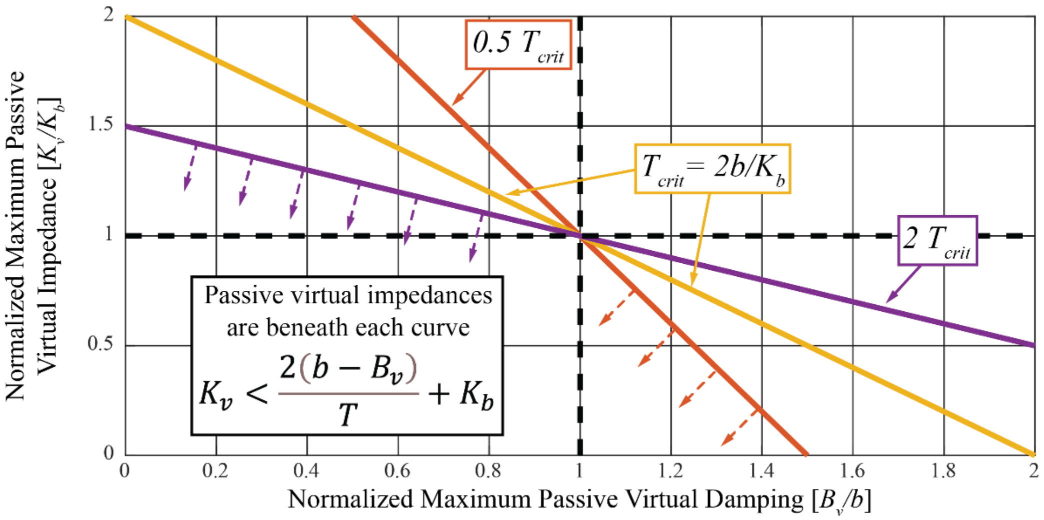

Figure 5: Normalized Z-width plot of the hybrid actuator. The range of passive stiffness and damping the hybrid actuator can achieve normalized by the device's physical stiffness and damping. Changing the sample frequency changes the slope of the passivity boundary.

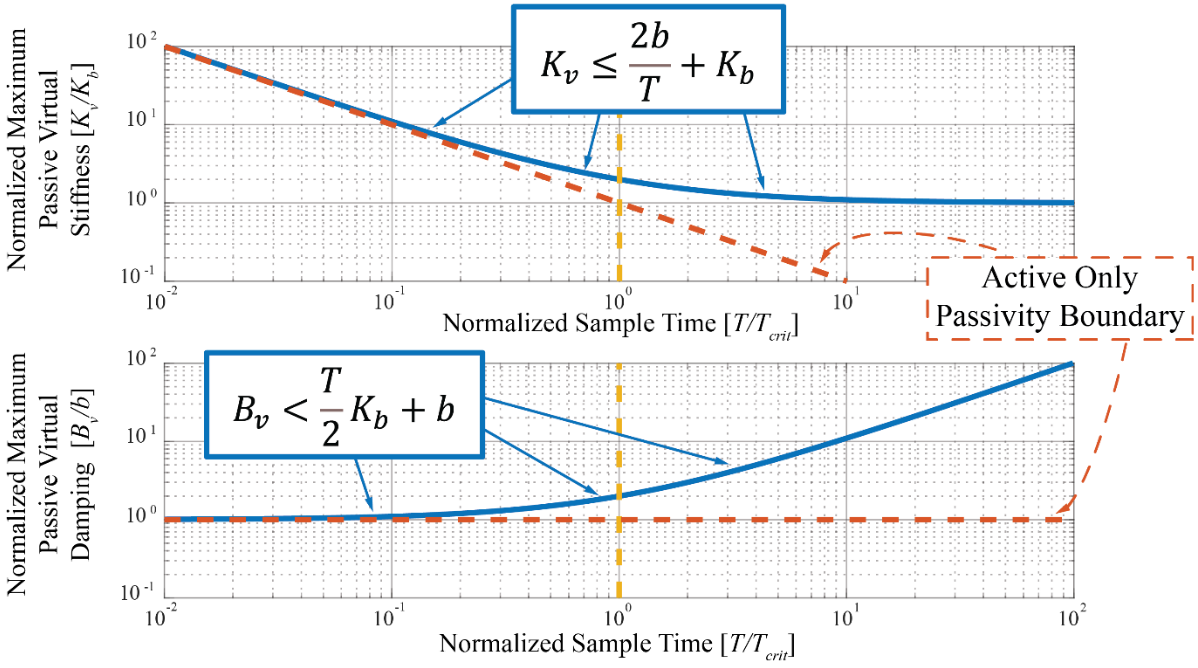

Figure 6: Maximum virtual stiffness and damping plotted against sample frequency. Each plot shows that the hybrid actuator outperforms its active counterpart at sample frequencies below the critical sample frequency (16). The sample frequency is normalized by (16).

As seen in (8) and (15) and Fig. 5 and 6, the hybrid system outperforms an active system most significantly at lower sample frequencies. In fact, we can identify a critical sample frequency or sample time, from the passivity-based expressions (8) and (15), in terms of system parameters. The hybrid system will outperform typical active only systems in the sense that the maximum passive rendered stiffness and damping will be significantly larger for sample frequencies larger than the critical sample time, (T_{crit} or conversely f_{crit}) identified in (16).

$$T_{crit} = \frac{2b}{K_b} \leftrightarrow f_{crit} = \frac{K_b}{2b} \tag{16}$$

For sample times less than T_{crit}, the hybrid and active only systems have more comparable performance, although the hybrid device's maximum passive virtual stiffness will always achieve a higher virtual stiffness than the active device alone by a quantity of at least the brake stiffness even at very small sample times.

C. Effects of Filtered Velocity Estimates on Passivity

A common tactic to increase the range of stable impedances a haptic device can achieve is to low pass filter the velocity estimate used to produce virtual damping. It is well documented that doing so can improve the stability margins of haptic devices and increases velocity resolution, which can be quite poor due to position quantization and high sample frequencies typical to high performance haptic devices. Introducing a low pass filtered velocity estimate in active devices limits the "negative damping" that is produced at the Nyquist frequency by unfiltered virtual damping [6-8].

This logic again holds true in the case of our hybrid device and filtering our velocity estimate increases the range of passive virtual damping the device can achieve. Assuming a first order low pass filter results in the controller (17) and the inequality (18).

$$H\left(e^{j\omega T}\right) = (K_v - K_b) + B_v \frac{z-1}{(\tau - T)z - \tau} \tag{17}$$

$$b > \frac{T(K_v - K_b)}{2} + \frac{B_v T}{2\tau + T} \tag{18}$$

In (17) and (18) τ is the first order filters time constant which is inversely related to the filter's cutoff frequency. Rearranging (18) into (19) expresses the maximum virtual stiffness and damping the hybrid device can achieve (Fig. 7) and the maximum passive virtual damping given a first order velocity filter (20) and Fig.8.

$$K_v < \frac{2b}{T} + K_b - \frac{2}{T}\frac{B_v T}{2\tau + T} \tag{19}$$

$$B_v < \tau\left(K_b + \frac{2b}{T}\right) + \left(\frac{TK_b}{2} + b\right) \tag{20}$$

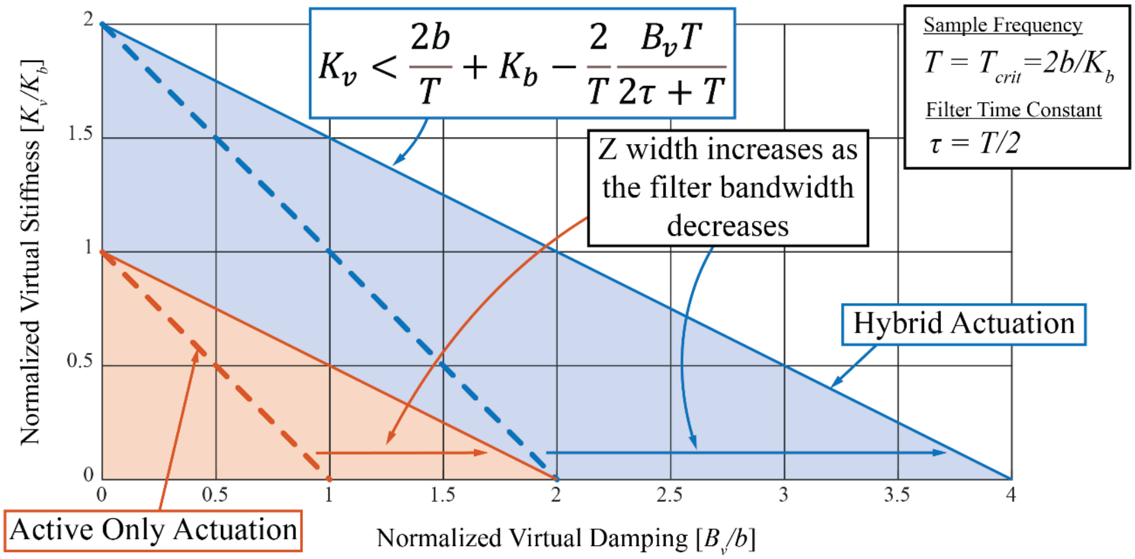

Figure 7: Range of maximum passive stiffness and first order filtered damping. The hybrid actuator will always outperform its active counterpart. As filter time constants increase (bandwidth decreases) The maximum passive damping of the system increases. A first order filter is used in this figure and the shaded areas correspond to a filter bandwidth of 10 Hz. Dashed lines correspond to the cases previously discussed where no velocity filtering is used.

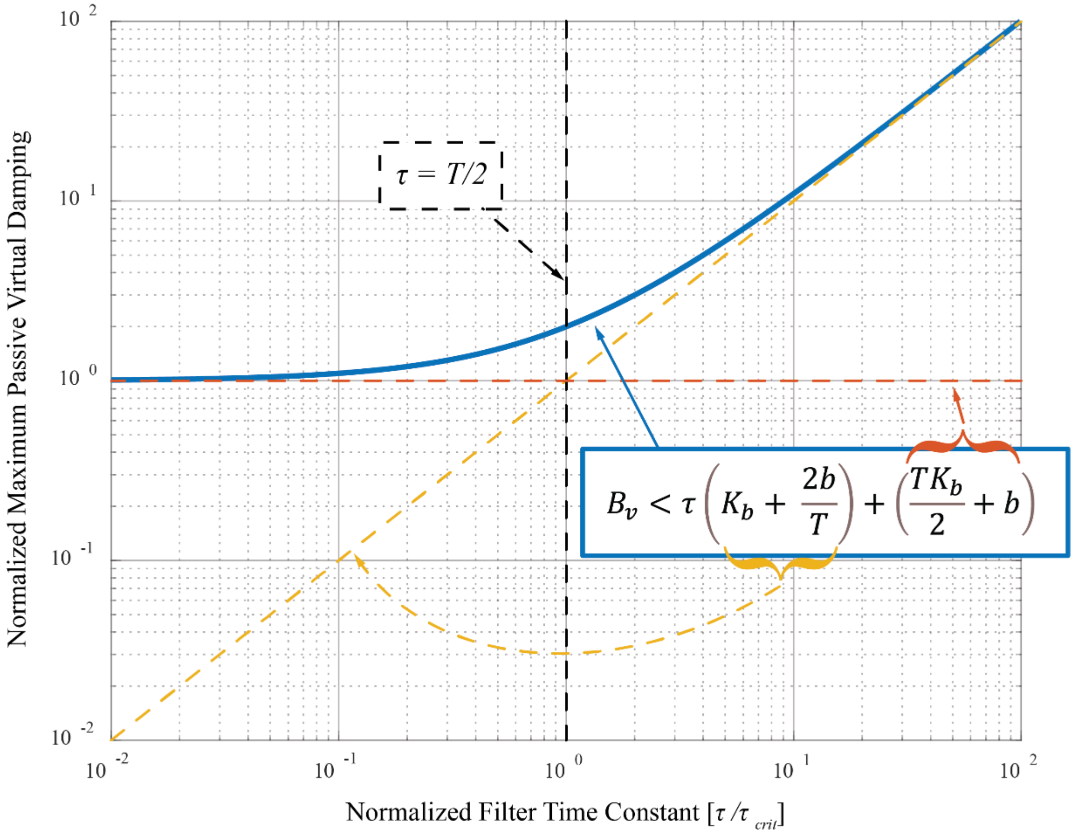

Figure 8: Range of hybrid actuator passive damping plotted against filter time constant. The critical filter time constant shows that the filter bandwidth must be considered in relation to the sample frequency to increase the range of passive damping significantly.

Focusing on virtual damping alone allows us to analyze the impact of velocity filtering more directly. It's interesting to note that terms affected by the filter bandwidth include both the brake stiffness and physical damping. This is again because actively canceling the brake stiffness generates damping. One might see the filter time constant in (20) as a regularization parameter trading off between two solutions (the unfiltered and completely filtered cases). As the filter bandwidth increases to infinity (*τ=0)* we can simplify (20) to the unfiltered case (15). Conversely, as the filter bandwidth decreases the maximum passive damping increases theoretically to infinity. Although in this case the device will dot feel as intended and no damping will be conveyed to the user. A critical filter time constant or filter bandwidth identifies the filter parameters where the effects are more impactful (21).

$$\tau_{crit} = \frac{T}{2} \tag{21}$$

We chose to normalize (20) shown in Fig. 8 by the critical filter bandwidth (the Nyquist frequency) and the unfiltered expression (15) to emphasize this result. The implications of this on design are clear and pertain to both active and hybrid devices alike. One must set the filter bandwidth in relation to the sampling frequency and to much lower than the Nyquist frequency or τ_{crit} to significantly increase the maximum passive virtual damping by filtering velocity estimates.

D. Effects of Pure Time Delays on Passivity

Pure time delays are common in control systems and can be caused by significant computations or simply communication delays in measured signals. Additional time delays often have negative impacts on the stability of haptic devices and have a unique impact on their passivity [9]. Our hybrid actuator is no exception and (10) can be used to evaluate passivity of our hybrid actuator under time delays, T_D, by substituting a pure time delay into the control law. First considering virtual stiffness alone results in the control law (22) and the inequality (23).

$$H\left(e^{j\omega T}\right) = (K_v - K_b)e^{-j\omega T_D} \tag{22}$$

$$b > \frac{T(K_v - K_b)\left(cos\left(\omega(T + T_D)\right) - cos(\omega T_D)\right)}{2(\cos(\omega T) - 1)} \tag{23}$$

When considering virtual impedances where the virtual stiffness is greater than the brake's stiffness. The maximum passive virtual stiffness with time delays takes the form of (24).

$$K_v \leq \frac{b}{\left(\frac{T}{2} + T_D\right)} + K_b \tag{24}$$

While (24) bounds the maximum passive virtual stiffness the hybrid actuator can produce, the possibility of a ***minimum passive impedance greater than zero*** still exists under time delayed conditions as shown in Fig. 9. The possibility of minimum passive stiffness highlights a key difference between true time delays and the approximate delay ($T_D \approx T/2$) induced by the zero-order hold. When assuming a zero impedance (Kv = 0) the inequality (23) is most restrictive at the Nyquist frequency (pi/T). Under specific conditions we can solve (23) analytically for the largest delay the hybrid actuator is able to render zero impedance passively (25).

$$T_D < T\left(1 - \frac{\arccos\left(\frac{2b}{K_b T}\right)}{\pi}\right) \qquad if \quad \frac{2b}{K_b T} < 1 \tag{25}$$

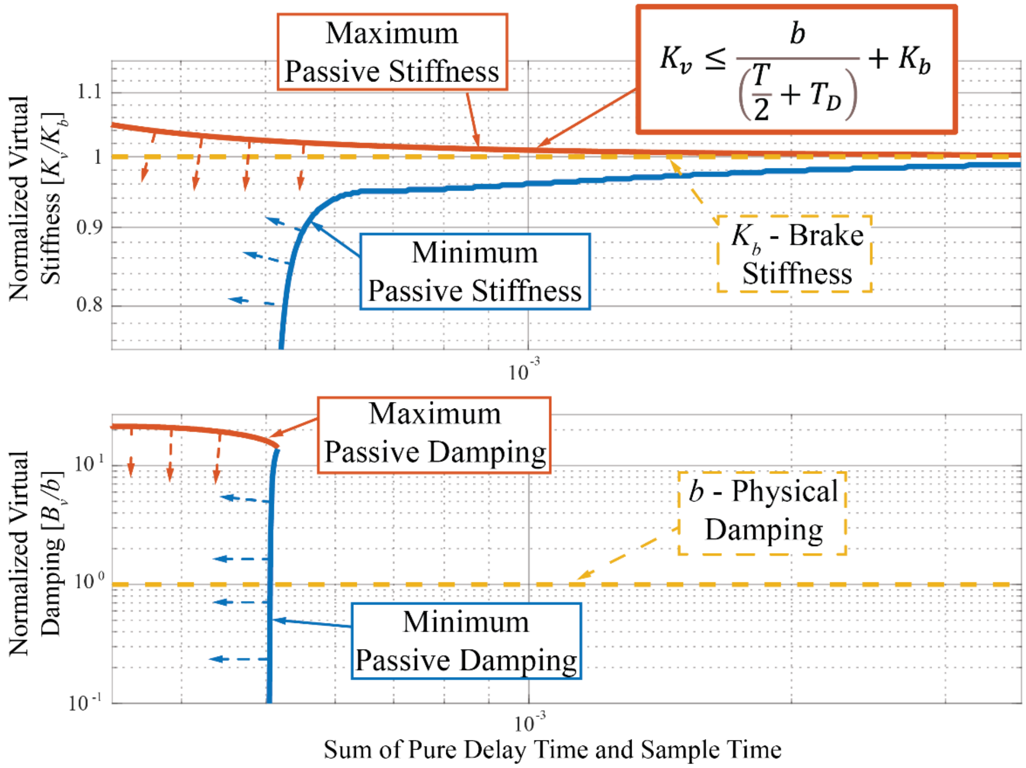

Figure 9: Time delays effect on range of passive virtual stiffness and damping. Numerically calculated virtual stiffness shows a minimum passive virtual impedance. Virtual damping can also display a minimum impedance behavior if the correct parameters are chosen.

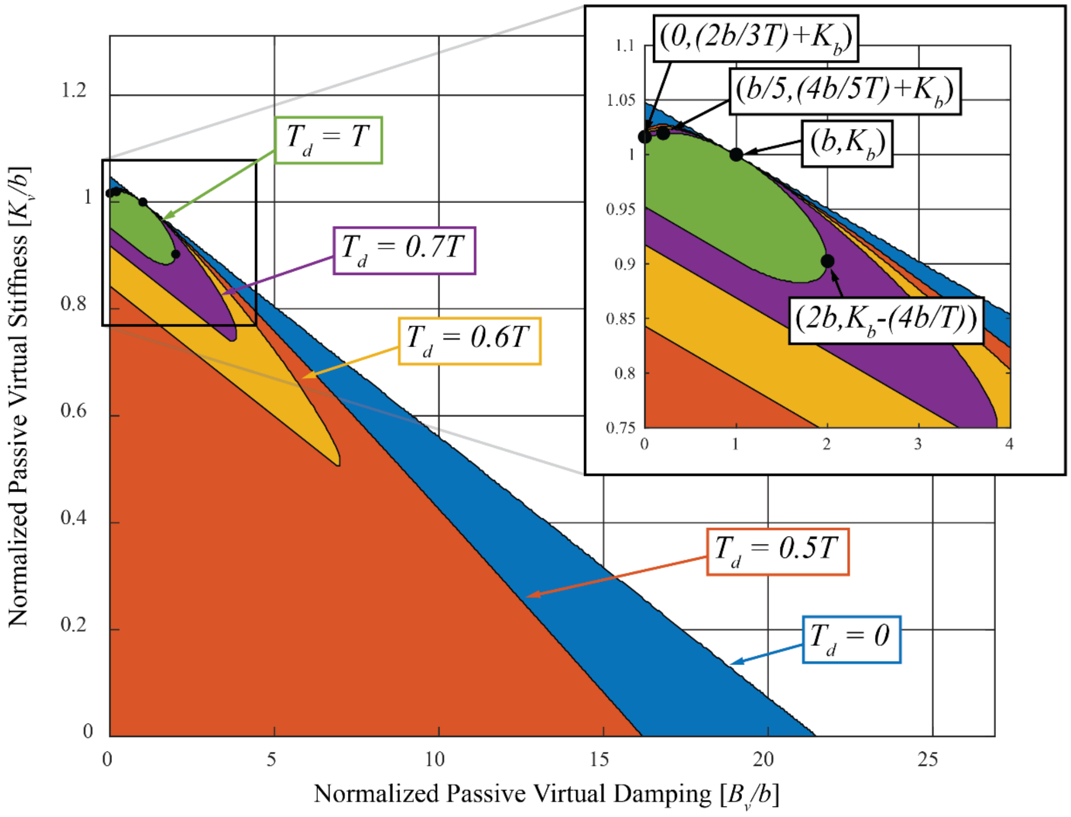

Figure 10: Hybrid actuator Z-width contour when considering time delays. Passive range of virtual impedances shrink towards the (K_b,b) point as the internal time delay increases.

Unfortunately, solving for an analytical minimum or maximum passive impedance considering any time delay generally results in a transcendental equation which does not have an analytical solution. Fortunately, the passivity inequality can be evaluated numerically and it's possible to plot the range of passive virtual impedances (stiffness and damping) of the time delayed system which is shown in Fig. 7 and 8. In Fig. 7 and 8 we use parameters from table 2 in the experimental Chapter 4 which are representative of the desktop hybrid haptic device in Chapter 1 Fig. 1. For a given sample frequency introducing time delay shrinks the range of passive stiffness and damping toward the point with the coordinates of the systems physical brake stiffness and damping (K_b and b)

Analytical solutions for specific time delay multiples of the sample frequency are possible but are too numerous to be covered exhaustively in this work. Analytical solutions bounding the region of passive stiffness and damping considering a full sample delay ($T_D = T$) are shown in Fig. 10. In this case we can see sampling faster (decreasing T and T_D concurrently) expands the region of passive stiffness and damping. This is contrary to results in the case without time delays where sampling more slowly increases the range of passive damping while decreasing the maximum passive virtual stiffness. Conclusions presented in the zero-time delay case, where increasing sample times increase the hybrid actuators stable rendering range, generally hold true for small time delays (T_d ~< equation (25)). However, if passivity is necessary pure time delays even as small as a full sample period can significantly limit benefits to the range of passive impedances our hybrid actuation approach achieves.

References

[1] J.-J. E. Slotine and W. Li, *Applied nonlinear control*. Englewood Cliffs, N.J: Prentice Hall, 1991.

[2] J. J. Abbott and A. M. Okamura, "Effects of position quantization and sampling rate on virtual-wall passivity," *IEEE Trans. Robot.*, vol. 21, no. 5, pp. 952–964, Oct. 2005, doi: 10.1109/TRO.2005.851377.

[3] N. Hogan, "Controlling impedance at the man/machine interface," in *Proceedings, 1989 International Conference on Robotics and Automation*, Scottsdale, AZ, USA: IEEE Comput. Soc. Press, 1989, pp. 1626–1631. doi: 10.1109/ROBOT.1989.100210.

[4] R. B. Gillespie and M. R. Cutkosky, "Stable User-Specific Haptic Rendering of the Virtual Wall," in *IMECE96*, Dynamic Systems and Control, Nov. 1996, pp. 397–406. doi: 10.1115/IMECE1996-0362.

[5] N. Diolaiti, G. Niemeyer, F. Barbagli, and J. K. Salisbury, "Stability of Haptic Rendering: Discretization, Quantization, Time Delay, and Coulomb Effects," *IEEE Trans. Robot.*, vol. 22, no. 2, pp. 256–268, Apr. 2006, doi: 10.1109/TRO.2005.862487.

[6] J. E. Colgate and J. M. Brown, "Factors affecting the Z-Width of a haptic display," in *Proceedings of the 1994 IEEE International Conference on Robotics and Automation*, San Diego, CA, USA: IEEE Comput. Soc. Press, 1994, pp. 3205–3210. doi: 10.1109/ROBOT.1994.351077.

[7] D. Weir and J. Colgate, "Stability of Haptic Displays," in *Haptic Rendering*, M. Otaduy, Ed. A K Peters/CRC Press, 2008, pp. 123–156. doi: 10.1201/b10636-9.

[8] N. Colonnese and A. Okamura, "Stability and quantization-error analysis of haptic rendering of virtual stiffness and damping," *The International Journal of Robotics Research*, vol. 35, no. 9, pp. 1103–1120, Aug. 2016, doi: 10.1177/0278364915596234.

[9] T. Hulin, A. Albu-Schäffer, and G. Hirzinger, "Passivity and Stability Boundaries for Haptic Systems With Time Delay," *IEEE Trans. Contr. Syst. Technol.*, vol. 22, no. 4, pp. 1297–1309, Jul. 2014, doi: 10.1109/TCST.2013.2283372.

Chapter 3: Hybrid Actuator Asymptotic Stability

While passivity is a popular property for a haptic device to have, tuning a system to be passive is often considered to be overly conservative. Uncoupled asymptotic stability (where the device is analyzed without considering the human coupled to the devices driving point) is perhaps a more useful and realistic metric to analyze the stability performance of an impedance type haptic device like our hybrid haptic device. Uncoupled stability is often used as a design metric in impedance type haptic devices because typically humans add damping to the system which in turn stabilizes impedance type haptic devices. It follows that an impedance based haptic device's stability margins are generally smallest when a user lets go of the device.

Though true discrete time control analysis provides the most faithful method to analyze uncoupled stability from a dynamic systems standpoint, traditional continuous time control methods can provide more accessible explanations to understand the dynamics of the hybrid actuator. Here we chose to both explicitly model the zero-order hold in our hybrid control system (Fig 2) and to provide more intuitive understanding of the device's performance through continuous time modeling and analysis methods (Fig. 1).

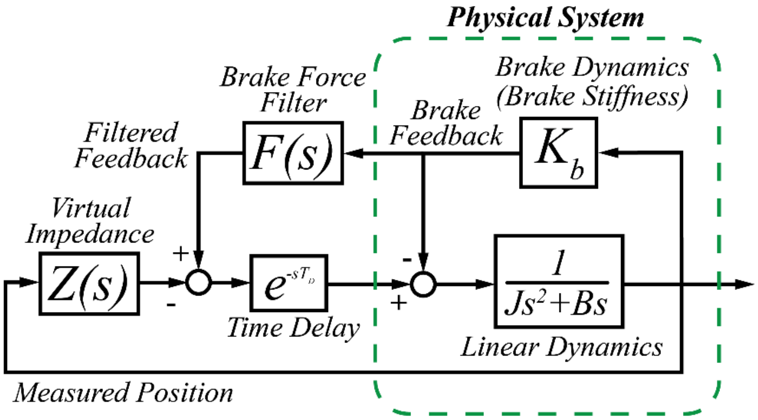

Figure 1: Continuous time hybrid actuator and control system. The SDOF system includes brake stiffness, damping and inertia of the system, time delay, brake filter, and a virtual impedance.

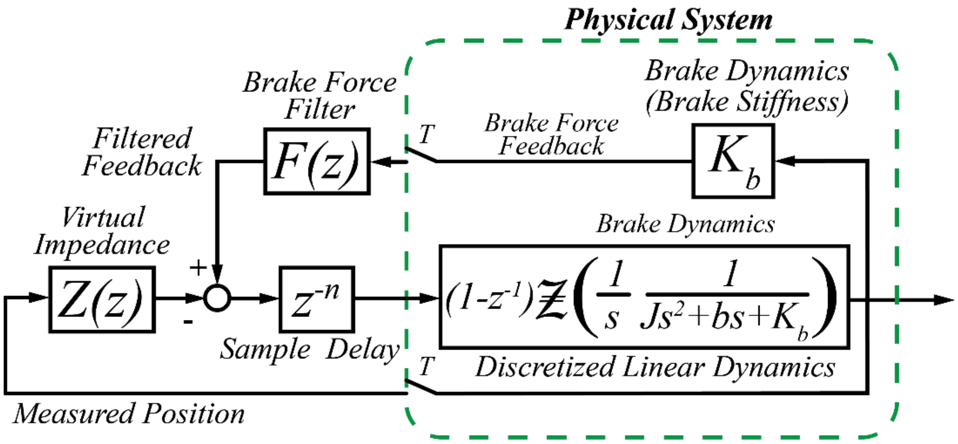

Figure 2: Discrete time hybrid actuator and control system. The single degree of freedom system explicitly models the sample and hold dynamics of the discrete time controller using the zero-order hold method. It also includes a discrete time delay, discrete brake torque filter, and a virtual impedance which can accommodate the dynamics of a backwards difference velocity estimate.

A. Virtual Stiffness Continuous Time Analysis.

We can consider asymptotic stability of the time delayed continuous time system shown in Fig. 1, using pseudo-delay methods [1], [2]. Pseudo-delay methods utilize a mapping based on the bilinear transform to transform the infinite dimensional time delayed system to a finite dimensional system. Stability analysis of the finite dimensional system allows one to draw conclusions about the stability of the original system.

First, we substitute the pseudo-delay (25) for pure delay terms in the system's closed loop transfer function yielding the characteristic quasi-polynomial (26)

$$e^{-sT_D} = \frac{1-\frac{T}{s}}{1+\frac{T}{s}} \tag{25}$$

$$JTs^3 + (J+bT)s^2 + (b - K_vT + 2K_bT)s + K_v \tag{26}$$

The Routh array, Table 2, can be used to analyze the stability of (26) which now depends on an additional parameter, *T*, the pseudo-delay. The system will be stable if the first column of the Routh array is positive.

TABLE 1: Routh Array For Characteristic Quasi-polynomial

JT	$b - K_v T + 2K_b$
$J + bT$	K_v
$\dfrac{(2bK_b - bK_v)T^2 + (b^2 - 2JK_v + 2JK_b)T + bJ}{bT + J}$	0
K_v	0

Considering only positive parameter values leaves (27) as the limiting case. The quadratic form in *T* of the numerator of (27) enables us to use a discriminate analysis to determine the range of values where the system will be positive definite and stable for all values of the *T*.

$$\frac{(2bK_b - bK_v)T^2 + (b^2 - 2JK_v + 2JK_b)T + bJ}{bT + J} \tag{27}$$

Setting the discriminate equal to zero and solving for the virtual stiffness, K_v, yields (28), the upper bound for the maximum uncoupled virtual stiffness independent of delay.

$$K_v \leq K_b + \frac{b\sqrt{4JK_b - b^2}}{2J} \tag{28}$$

Equation (28) is especially relevant when considering the time delayed passivity results presented in Chapter 2. The hybrid actuator also shows the property of asymptotic stability independent of time delay. Generally, the second term of (28) is quite small and the predicted numeric values of passivity independent of time delay or sample frequency are quite similar. However (28) indicates a key difference between the stability metrics. While there is a possibility of a non-zero minimum passive stiffness, (28) indicates that our hybrid actuator remains asymptotically stable independent of time delay for all virtual stiffness greater than zero and less than (28).

B. Effects of Passive Actuator Feedback on the Maximum Virtual Stiffness

Prior to this section we have considered a system with ideal passive feedback, where the measured brake force was not filtered. However, an unfiltered passive feedback signal can be difficult to achieve in practice. Filtering may be required due to sensor noise or to prevent aliasing during analogue to digital conversion. The addition of a filter must be done carefully because it has implications on both the stability and output impedance of the actuator.

Evaluating closed form solutions of uncoupled asymptotic stability is not practical for the filtered brake feedback case with delay, shown in Fig. 1. As such, we numerically evaluate uncoupled asymptotic stability utilizing the open loop transfer function (29) while neglecting equivalent damping (see Appendix C), using a bisection method, bode plots, and the Nyquist Stability Criteria (see Fig. 3).

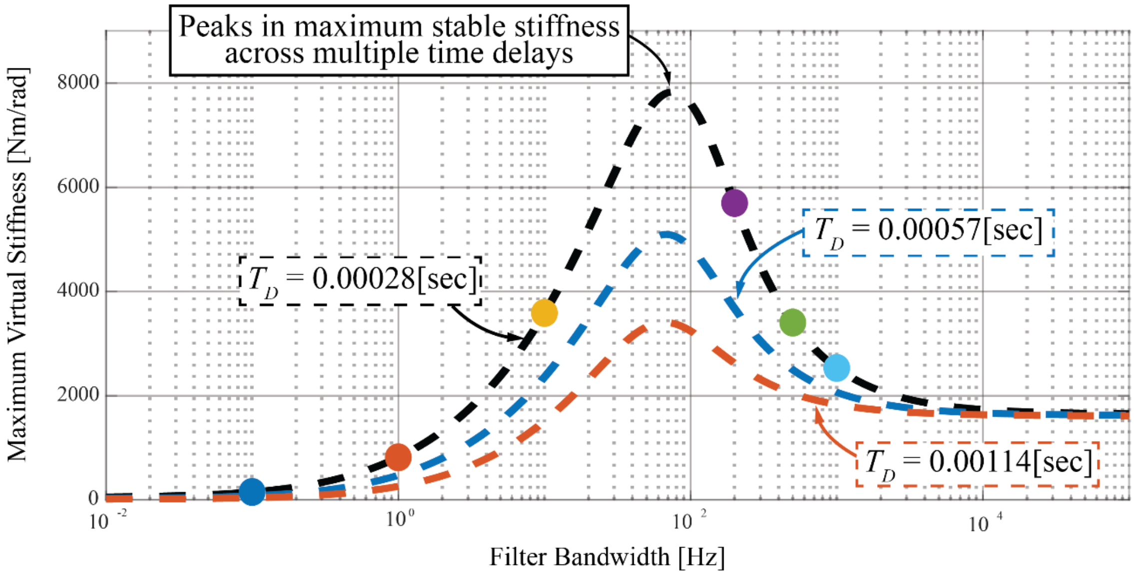

Figure 3: The impact of filtered brake feedback on maximum virtual stiffness. An optimum brake filter feedback bandwidth exists and maximum virtual stiffness reduces with increased time delay. Colored points on the dashed black curve are color coded to the open loop transfer functions plotted in Fig. 5 and Fig. 6.

$$OLTF = \frac{\theta(s)}{\tau(s)} = \frac{e^{-s\left(\frac{T}{2}+T_D\right)}}{Js^2 + bs + K_b - e^{-s\left(\frac{T}{2}+T_D\right)}\left(\frac{\omega_c}{s+\omega_c}\right)K_b} \tag{29}$$

Where J is the device inertia, b is the linear damping, K_b is linear brake stiffness $T/2$ is the approximate delay induced by the zero-order hold, T_D is any additional pure delay, and ω_c is the passive actuator feedback first order filter cutoff frequency. As seen in Fig. 3, the maximum virtual stiffness approaches the active devices' stability limit as the filter cutoff frequency approaches zero. Conversely, the maximum virtual stiffness approaches the result obtained for a fixed delay alone (where we assume perfect brake torque measurement) as the cutoff frequency approaches infinity. As seen in Fig. 3, continuously varying the filter cutoff frequency shows a curious peak in the resulting uncoupled stability curve, suggesting that the maximum virtual stiffness can be increased significantly, as compared to the perfect brake measurement case, by selecting a particular brake feedback cutoff frequency.

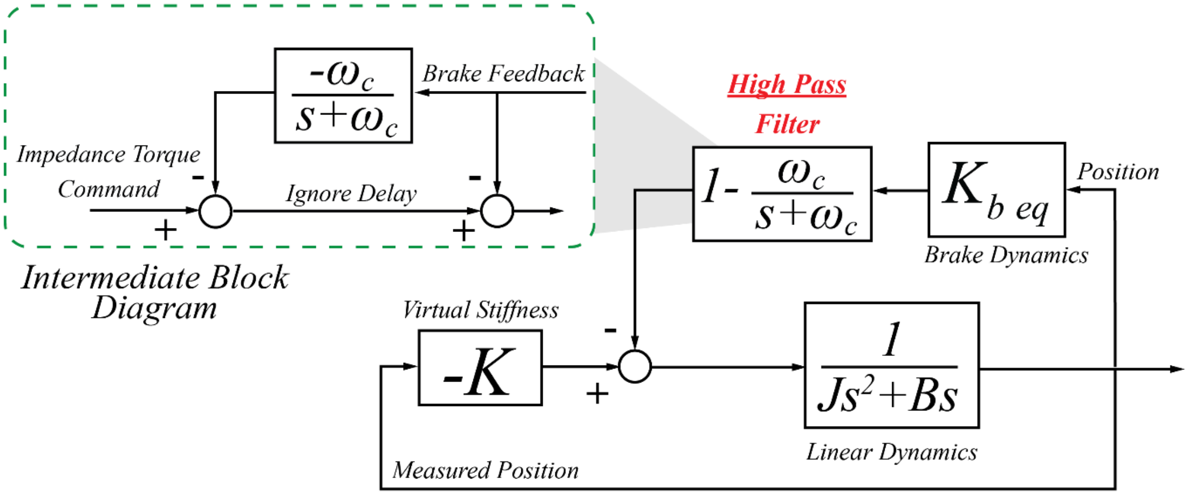

Figure 4: Reformulated block diagram to show the high pass filter effect. Reformulated block diagram showing the effect of passive actuator torque and passive actuator feedback resulting in a net high pass filtered position feedback effect on the open loop transfer function.

To gain insight into this phenomenon, it is useful to temporarily ignore delay in the system, which allows us to reorganize our block diagram from Fig. 1 into Fig. 4. As seen in Fig. 4, physical reflected brake torque and the low pass filtered brake feedback signal produced by the active actuator cancel each other at low frequencies. Subtracting a low pass filtered signal from the original unfiltered signal results in a high pass filtered signal. High pass filtering a signal in phase with position (the derivative of position is velocity) results in the approximation of damping torques (a torque in phase with velocity) below the filter bandwidth.

One can use the system's open loop frequency response and the Nyquist stability criteria to better understand why the high pass behavior of the brake and filtered brake feedback allow for increased virtual stiffness. Additionally, we aim to understand why there is an optimal tuning and how one can tune the passive feedback filter to obtain this. Fig. 5 shows the system's open loop transfer function for a range of filter cutoff frequencies.

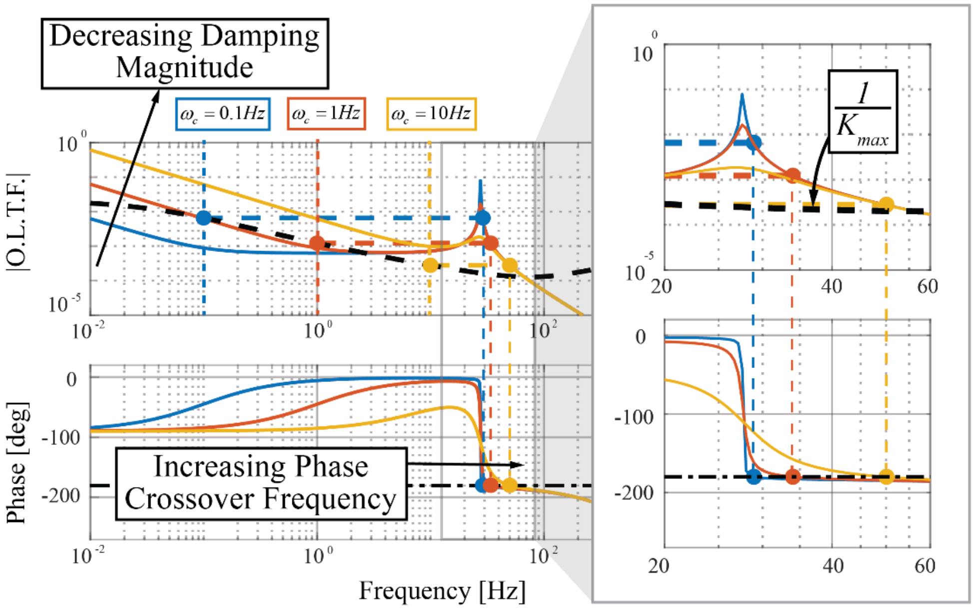

Figure 5: Bode plots of the systems open loop transfer function while increasing stiffness Bode plots of the open loop transfer function of the system with increasing filter bandwidth. Increasing maximum virtual stiffness corresponds to adding damping at the crossover frequency.

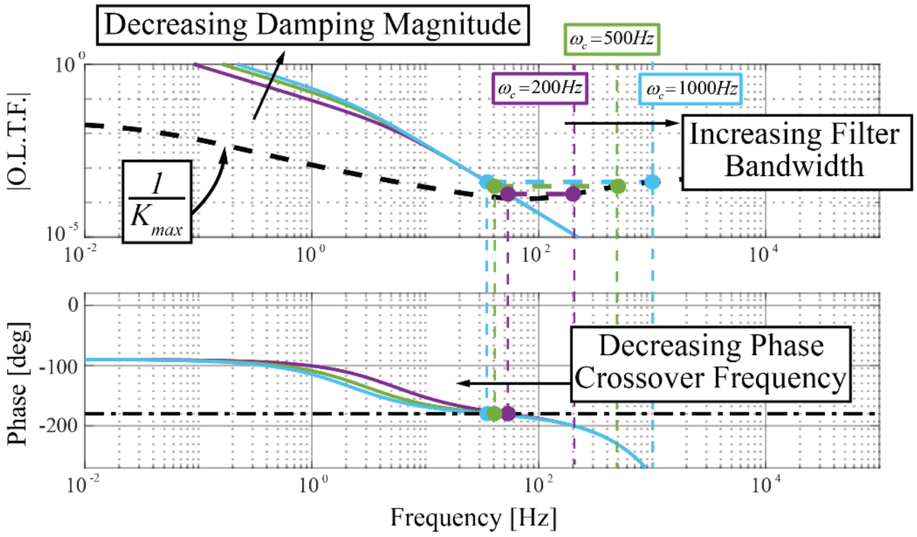

Figure 6: Bode plots of the systems open loop transfer function while decreasing stiffness. The system displays decreasing maximum virtual stiffness because the magnitude of the added damping decreases as the filter bandwidth increases.

Fig. 5 shows three frequency responses of the hybrid open loop transfer function corresponding to the portion of Fig. 3, where the maximum virtual stiffness increases as the cutoff frequency increases. The effect of the combined high pass filter on the maximum stable virtual gain becomes clear with knowledge of the combined high pass hybrid damping effect. As the filter bandwidth increases, damping from the high pass hybrid effect reaches higher frequencies. This helps to both decrease the magnitude of resonance associated with the brake stiffness and smooths the 180-degree phase loss associated with the otherwise lightly damped mode introduced by the brake leading to increases in the maximum virtual stiffness. Continuing to increase the filter bandwidth (Fig. 6) causes the filtering effect to reach higher frequencies but decreases the magnitude of damping added to the system. The reduction in magnitude leads to the peak and decreasing sections of Fig. 3. Overall, introducing the passive feedback filter can increase the actuators maximum virtual stiffness while mitigating noise in the brake feedback signal.

C. Discrete Time Asymptotic Stability Comparisons

Continuous time analysis of a time delayed system provides a convenient method to understand the impact of features of our hybrid actuation control system. However, continuous time analysis does not directly account for several features of discretization which are inherent to our control system. Both the true nature of the zero-order hold and extra delays induced by velocity estimates change the dynamics of the discrete system as compared to its continuous time approximate.

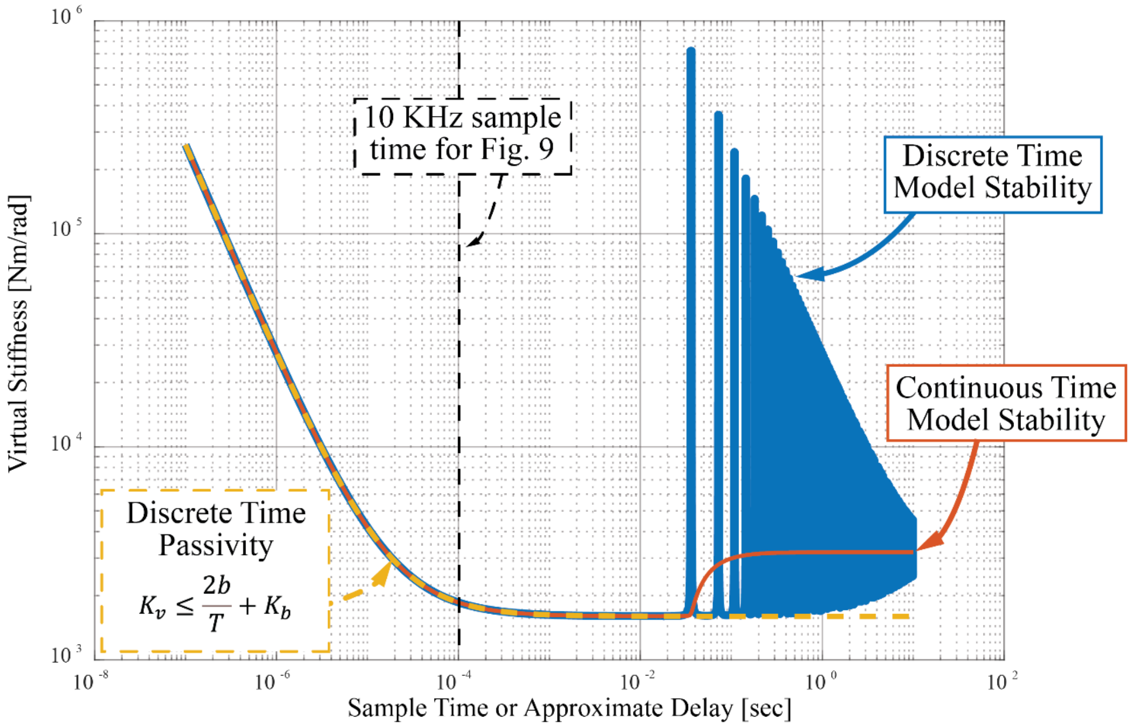

Figure 7: Maximum asymptotically stable virtual stiffness model and passivity comparison Maximum hybrid actuator virtual stiffness is similar to the maximum passive virtual stiffness (dashed lines). The continuous and discrete time models are quite similar at high sample frequency.

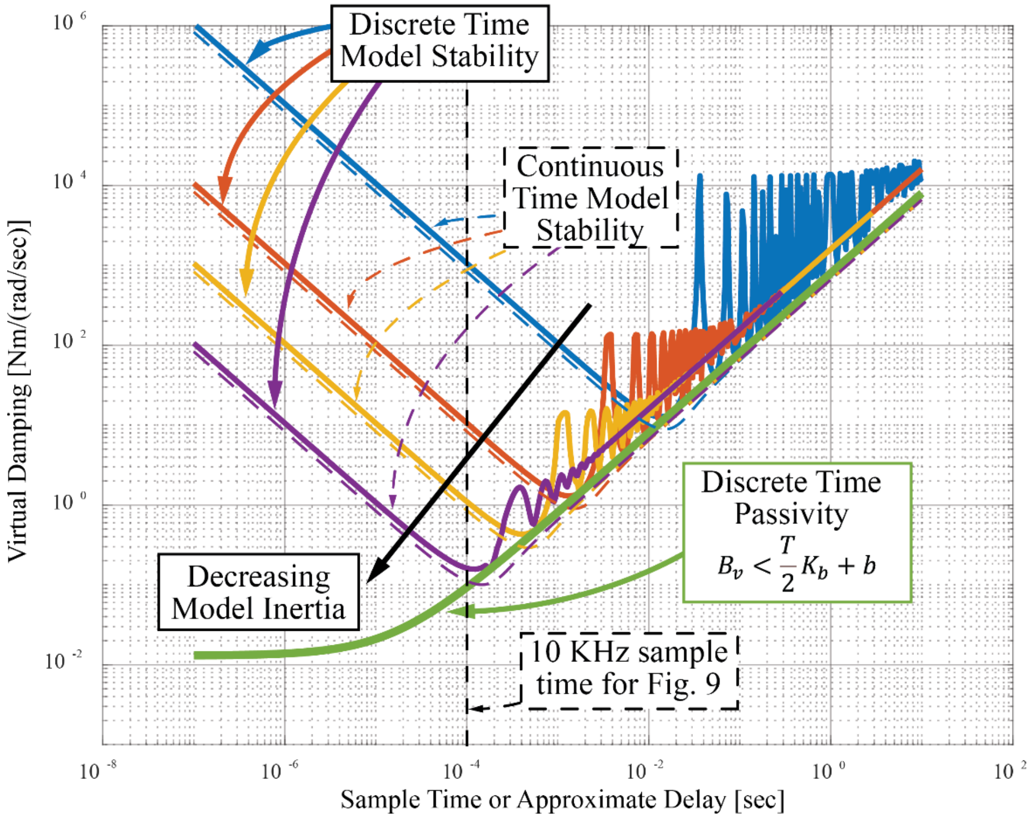

Figure 8: Maximum asymptotically stable virtual damping model and passivity comparison General trends are consistent between the continuous models shown in dashed lines and the discrete models shown in solid lines but the full discrete and continuous approximate models show significant differences in the case of virtual damping. As inertia of the system decreases the asymptotic stability boundaries approach the hybrid actuation stability boundary.

The differences can be observed by comparing stability results from continuous time models and discrete time models. While overall trends are consistent between the two models, numerical values significantly diverge for virtual damping (see Fig. 8 and the damping axis of Fig. 9). This is caused by a large difference in the magnitude of the open loop transfer function at the crossover frequency which is at a higher frequency and close to the Nyquist frequency for virtual damping compared to virtual stiffness.

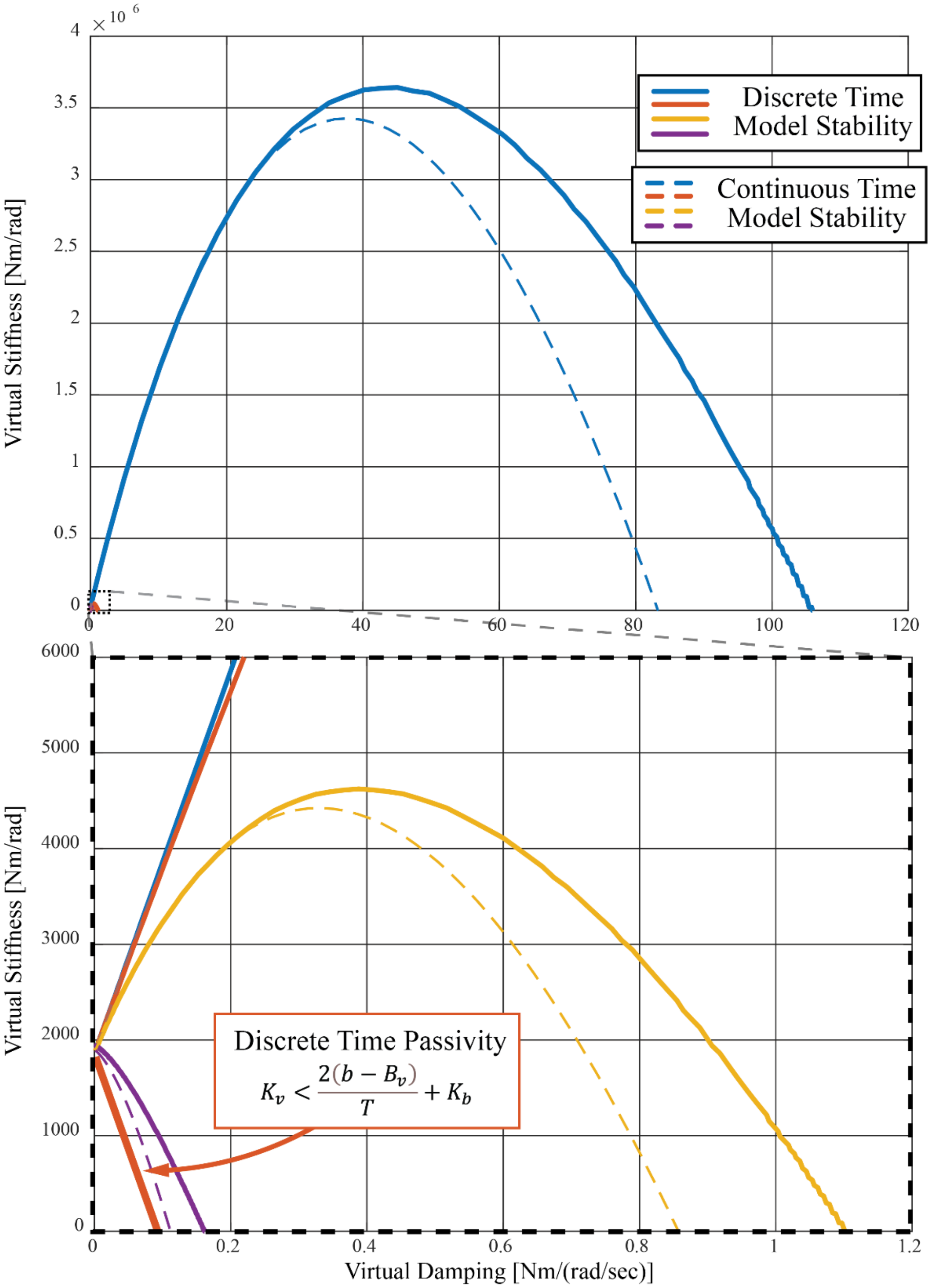

Figure 9: Z-width plots comparing results from discrete time and continuous time models. General trends are consistent between the continuous models shown in dashed lines and the discrete models shown in solid lines sample rate is 10 Khz.

The discrete time asymptotic stability boundary for a pure virtual stiffness is quite close to the virtual stiffness passivity boundary making it easy to see the impact of the hybrid actuator (see Fig. 7). However, in the case of virtual damping asymptotic stability and passivity boundaries deviate significantly (see Fig. 8). Again, inspecting the open loop transfer function shows that physical device inertia can dominate the frequency response around the crossover frequency and can drive asymptotic stability properties of the device while rendering virtual damping. Parametrically decreasing the inertia of the haptic device shows that the asymptotic stability boundary of the hybrid actuator approaches the passivity boundary for both virtual impedances (Fig. 8 and Fig 9).

While passivity results can be conservative in terms of a haptic device's measurable stable rendering range and uncoupled stability, passivity results bound stability performance and are reflected in asymptotic stability boundaries. Ultimately this translates to meaningful stability performance gains in our hybrid actuator. This is particularly true in the case of virtual stiffness but also for virtual damping.

References

[1] K. Walton and J. E. Marshall, “Direct method for TDS stability analysis,” *IEE Proc. D Control Theory Appl. UK*, vol. 134, no. 2, p. 101, 1987, doi: 10.1049/ip-d.1987.0018.

[2] K. Gu, V. L. Kharitonov, and J. Chen, *Stability of Time-Delay Systems*. Boston, MA: Birkhäuser Boston, 2003. doi: 10.1007/978-1-4612-0039-0.

Chapter 4: Experimental Stability Evaluation

We validated the stability of the hybrid actuation system using two configurations of a custom one degree of freedom hybrid actuator, shown in Fig.1a and b. The first configuration (shown in Fig1a) consists of a Maxon RE90 DC motor, used for the active actuator, and a Placid Industries B6 particle brake as the passive actuator. The actuators are rigidly connected via a capstan and are connected to the output handle via an approximately 11:1 veteran cable transmission. Passive actuator feedback is measured with an Interface MRT-2NM reaction torque sensor. The handle position is measured with a Renishaw Magnetic Linear Encoder, 450,000 lines per revolution, and is used to render the virtual impedance. This actuator configuration represents a high brake stiffness configuration typical of a hybrid device designed to extend the maximum stiffness above an equivalent active only device.

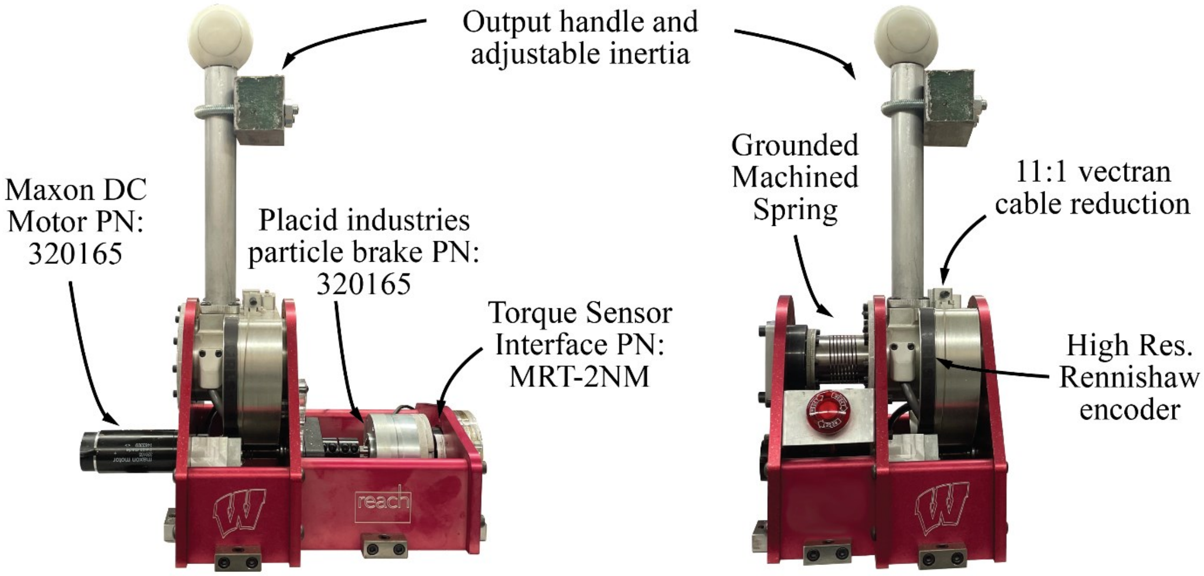

a) Parallel configuration of a stiff brake and DC motor.

b) Parallel configuration of a compliant "brake" and DC motor.

Figure 1: Desktop parallel hybrid actuator configurations used to test stability. a) A one degree of freedom hybrid actuator with a DC motor and particle brake connected in parallel. b) A "compliant brake" configuration utilizing a grounded spring as a stand in for the particle brake.

Fig. 1b shows a compliant brake configuration where we use a grounded spring as a stand in for a brake, primarily for the purpose of validating high brake filter cutoff frequency experiments which are not practical with the high stiffness configuration. The parameters for the single degree of freedom test setup are summarized in Table 1 and are used throughout this work for all figures presenting theoretical results. Table 1 also represents the parameters of the balanced hybrid interface shown at the beginning of this work in Chapter 1 Fig. 1

Table 1: Desktop Hybrid Haptic Device Parameters

Parameter	Brake Stiffness	Spring Stiffness	Handle Inertia	Damping
Value	1600	14	0.053	0.013
Units	[Nm/rad]	[Nm/rad]	[Nm/(rad/sec^2)]	[Nm/(rad/sec)]

A. Hybrid Stability Validation - Stiff Brake Configuration

We begin our experimental validation by testing the uncoupled stability of a prototype desktop hybrid actuator, using the high brake stiffness configuration, and comparing it to our theoretical results. During the experiment, we incrementally increased the virtual stiffness of the hybrid actuator. An active disturbance signal is injected onto the motor torque command to perturb the system. The system is also manually perturbed with a dead blow hammer. The test stiffness is considered stable if no vibrations or unstable behavior are detected after four perturbations, spaced two seconds apart. The virtual stiffness is then increased randomly, in a predetermined range. This process is repeated until unstable behavior, vibrations, or oscillations, are observed.

We tested five delays while running our system with a 3500 Hz sample frequency. The nominal experimental system delay, including the effects of sampling and processing, was measured at 0.0003 seconds. We added an additional pure time delay between 0.01 and 0.0001 seconds. Fig. 2 shows a comparison between the maximum stable stiffness when using the high brake stiffness configuration of the hybrid actuator and the maximum stable stiffness when using the active actuator stiffness configuration. The results from a series of five tests compare well to the theoretical results and are well above the theoretical active only stability curve at the delays used. As shown in Chapter 3B, varying the brake filter bandwidth is an important factor affecting the maximum stable virtual stiffness. Noise propagation in the high brake stiffness system limits the experimental validation to filter cutoff frequencies less than approximately 30 Hz. Fig. 2 compares the theoretical hybrid curve (for zero added delay) to a range of experimentally obtained maximum stiffness values over a range of filter cutoff frequencies.

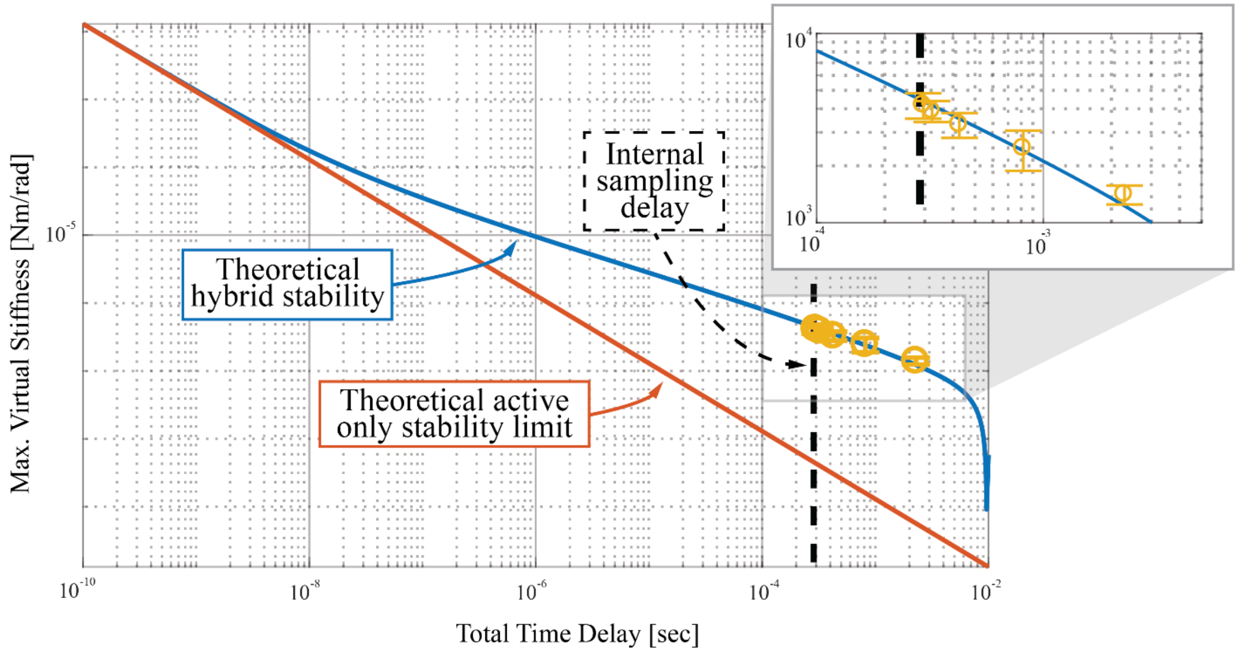

Figure 2: Maximum virtual stiffness stability results with a “stiff” brake while adding delay. Experimental stability results for a “stiff” brake under varying time delays compare well with the theoretical values and are considerably higher than the validated theoretical active only stability limit. The internal delay due to sampling prevents the testbed from testing smaller delay values where the hybrid and active only stability curves are closer together. A first order filter with a 15 Hz bandwidth is used on the passive actuator feedback signal.

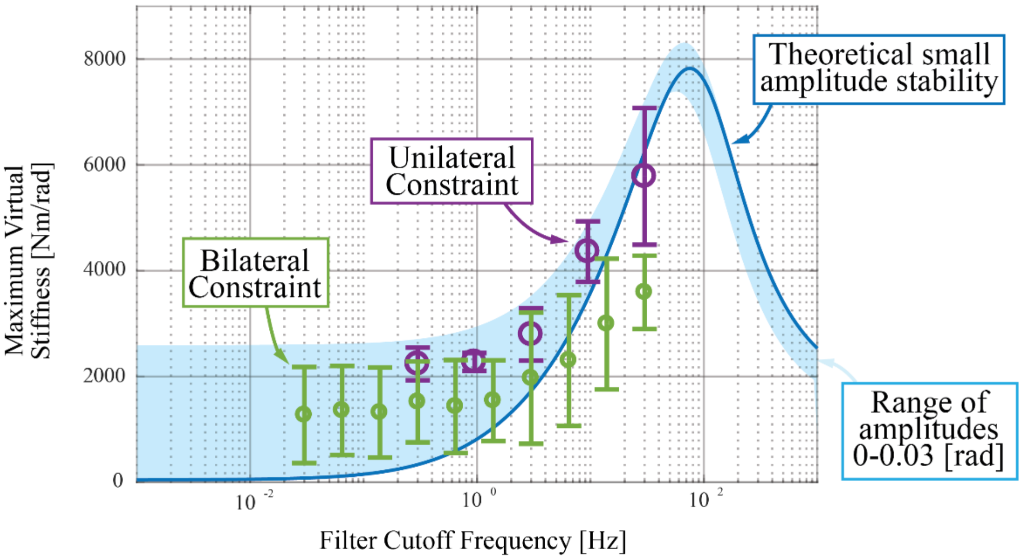

Figure 3: Maximum virtual stiffness with a “stiff” brake varying brake filter bandwidth. Theoretical maximum stable virtual stiffness while varying the feedback filter bandwidth. Experimental unilateral and bilateral tests are also plotted over the theoretical curves. Light blue shaded regions are the stable range of amplitudes for a range of oscillation amplitudes (from the large amplitude model which includes some equivalent damping from the brake model).

Experimental results from both varying time delay and filter bandwidth agree well with the linear analysis and deviations at lower filter cutoff frequencies are likely due to higher dissipation at larger amplitudes. Additionally, Fig. 3 shows experimental coupled stability results, where the actuator was tested using a unilateral constraint and a human user. Trends predicted in our analysis are reflected in unilateral coupled stability tests as well and we see an increase in the maximum stable virtual stiffness as filter cutoff frequency is increased to 30 Hz.

Additionally, we test the “Z-width” or the range of stable bilateral stiffness and damping for the hybrid actuator in Fig. 4. Comparing, the theoretical curve generated for the balanced hybrid actuator shows reasonable agreement across the stable range of stiffness and damping. Additional factors such as noise sensitivity related to the encoder resolution could help to explain differences between experimental and theoretical curves at the peak of the curve and near the virtual damping axis [1-3]. For an additional comparison the same test was performed on the active only portion of the actuator (the SEA and DC motor) which is already considered to be a capable haptic actuator. The hybrid actuator outperforms the active device across all impedances and envelopes the active device's stable rendering range.

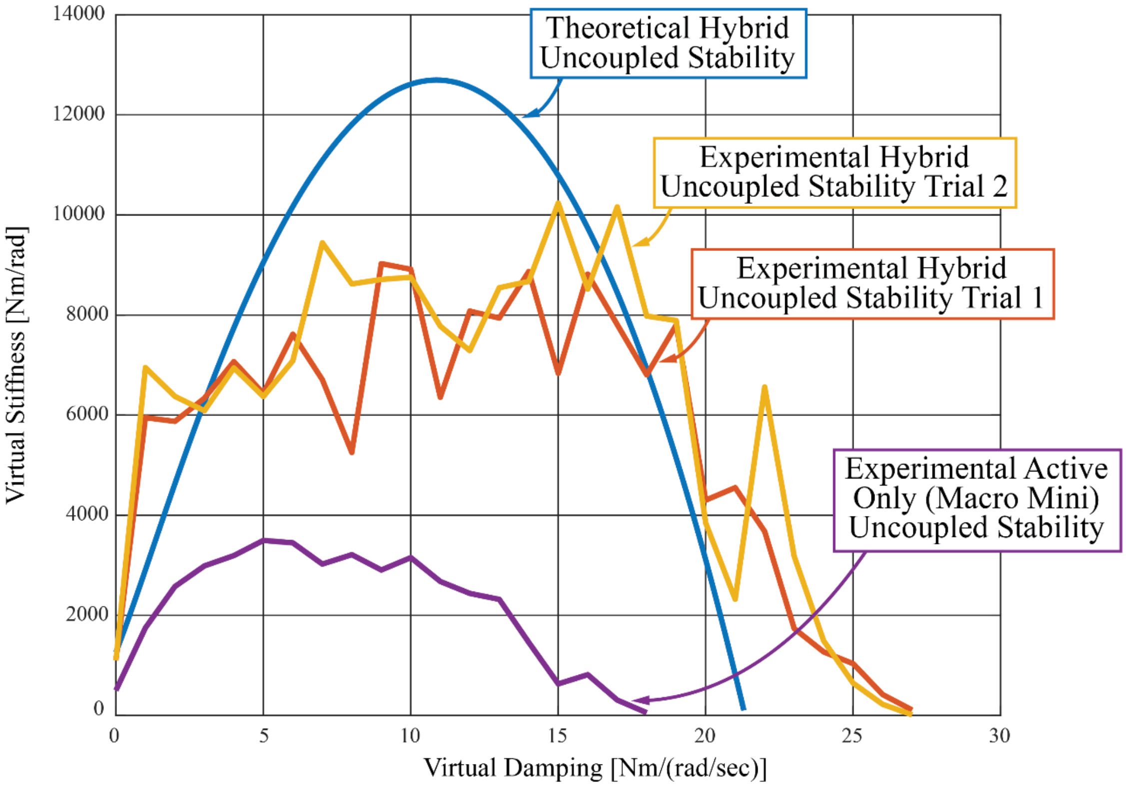

Figure 4: Experimental and theoretical Z-width plot for the balanced hybrid actuator. Curves compare the performance of the full desktop balanced hybrid actuator's performance to a theoretical hybrid uncoupled stability curve and the active only portion of the balanced hybrid actuator (SEA and DC motor). Tests were at 3500Hz sample frequency with a full sample of time delay. Additionally, the tests were performed without the bolted mass shown in Chapter 4 Fig. 1 reducing inertia (*J*=0.0076)

B. Hybrid Stability Validation – Compliant Brake Configuration

We present an additional experimental system validation utilizing a compliant brake configuration shown in Fig. 1b. We chose to test a low stiffness brake configuration primarily to allow for validation of the stiffness vs. filter bandwidth curve at higher filter bandwidth values. In addition, using a linear spring as a substitute for the small displacement brake stiffness provides the best possible comparison to the presented linear analysis. Finally, measuring spring deflection with a high-resolution encoder eliminates noise issues from torque sensor feedback allowing us to explore a wider range of filter cutoff frequencies.

Fig. 5 shows a comparison between theoretical and experimental results for an unfiltered passive feedback configuration and shows close agreement. The system is stable approximately up to the brake or spring stiffness even under conditions with large time delays.

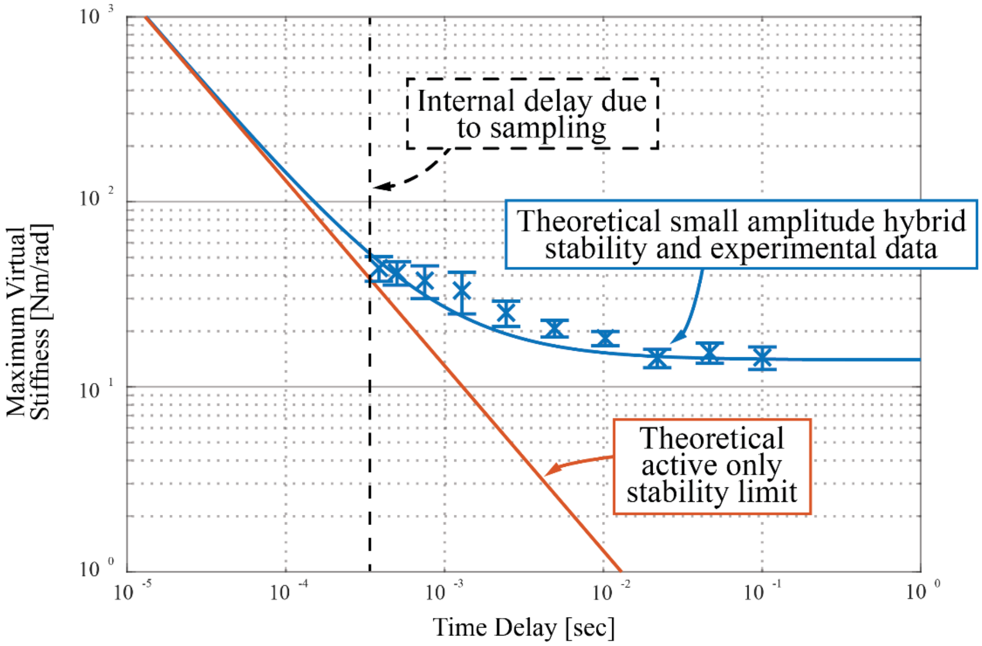

Figure 5: Maximum virtual stiffness stability results with a "compliant" brake adding delay. Experimental stability results under increasing time delays and unfiltered feedback with a compliant brake (Fig 1b) match the theoretical results closely.

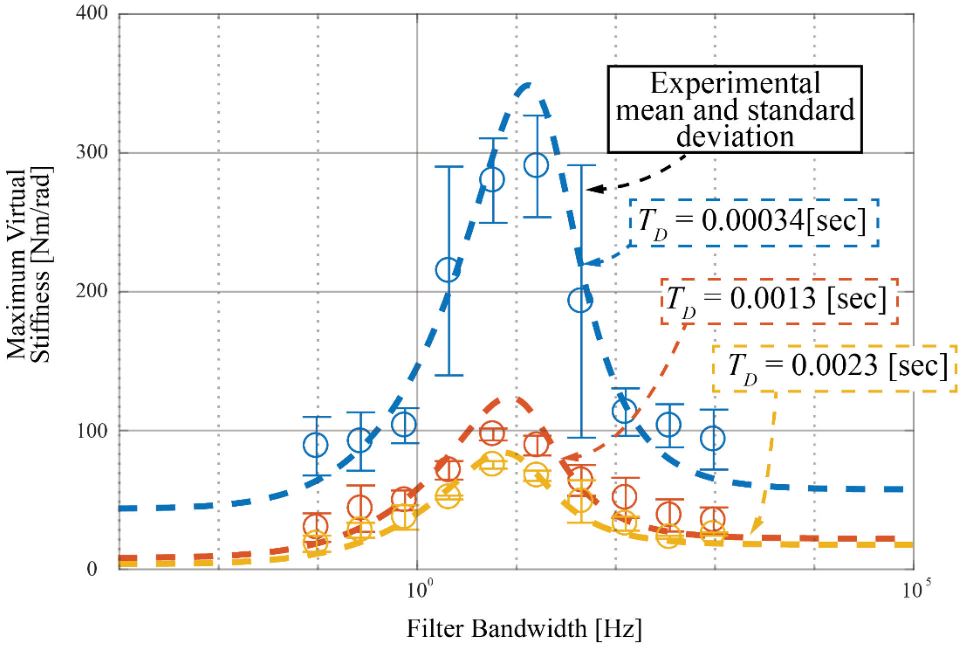

Figure 6: Maximum virtual stiffness with a "compliant" brake varying filter bandwidth. Maximum stable stiffness for varying first order filter cutoff frequencies is shown at three different delay values. Experimental results are shown with the mean and standard deviation from six experimental test runs.

We see from Fig. 6 that the peak stable stiffness predicted by our analysis, across three sample frequencies or time delays, agrees well both in terms of the predicted filter cutoff frequency and the maximum predicted stable stiffness. Experimental results from the compliant brake configuration validate the theoretical predictions made in Chapters 2 and 3 and shows that the peak in maximum stable virtual stiffness can be explained through our analysis.

References

[1] N. Colonnese and A. Okamura, "Stability and quantization-error analysis of haptic rendering of virtual stiffness and damping," *The International Journal of Robotics Research*, vol. 35, no. 9, pp. 1103–1120, Aug. 2016, doi: 10.1177/0278364915596234.

[2] N. Colonnese and S. Chan, "Z-Qualities and Renderable Mass-Damping-Stiffness Spaces: Describing the Set of Renderable Dynamics of Kinesthetic Haptic Displays," in *2019 IEEE World Haptics Conference (WHC)*, Tokyo, Japan: IEEE, Jul. 2019, pp. 325–330. doi: 10.1109/WHC.2019.8816117.

[1] J. E. Colgate and J. M. Brown, "Factors affecting the Z-Width of a haptic display," in *Proceedings of the 1994 IEEE International Conference on Robotics and Automation*, San Diego, CA, USA: IEEE Comput. Soc. Press, 1994, pp. 3205–3210. doi: 10.1109/ROBOT.1994.351077.

Chapter 5: Hybrid Actuation Haptic Limitations

Both the balanced and parallel hybrid actuation approaches work well and extend the stable rendering range of resulting hybrid haptic devices. However, several challenges potentially stand in the way of using these methods to achieve a high-performance hybrid haptic actuator. While methods presented in Chapters 2 and 3 focus on ensuring stable operation of the hybrid actuator, they do not ensure the actuator is delivering the intended impedance. Additionally, the control method presented in Chapter 1 assumes a rigid connection between the brake, high frequency actuator and the device's output which can be difficult to achieve in practice.

A. Limitations on Hybrid Actuation Output Impedance

All haptic devices have imperfect renderings due to physical device dynamics including damping, friction, and inertia. These unavoidable features inevitably distort the device's rendering and what a user feels when interacting with a haptic actuator. The impedance transfer function for our hybrid device, shown in (30), attempts to quantify these rendering defects, and shows how well our hybrid actuator replicates the desired impedance (*Z(s)*).

$$\frac{\tau_h(s)}{\theta(s)} = Js^2 + bs + K_b + \left(Z(s) - \frac{\omega_c}{s+\omega_c}K_b\right)e^{-sT_D} \tag{30}$$

Factors such as damping, and inertia (b and J respectively) are inherent to our hybrid device and can distort the desired output impedance but are typically designed to be small in impedance type haptic devices. Physical passive actuator dynamics represented simply here by the brake's stiffness K_b can distort the device's impedance as well. However, features of the control system including time delays, the zero-order hold, and passive actuator feedback bandwidth play the primary roles in determining the output impedance of our hybrid actuator. Fig. 1 and Fig. 2 each consider the independent effects of time delay, and passive actuator feedback filter bandwidth respectively. That is to say, Fig. 1 only varies time delays (infinite bandwidth passive feedback).

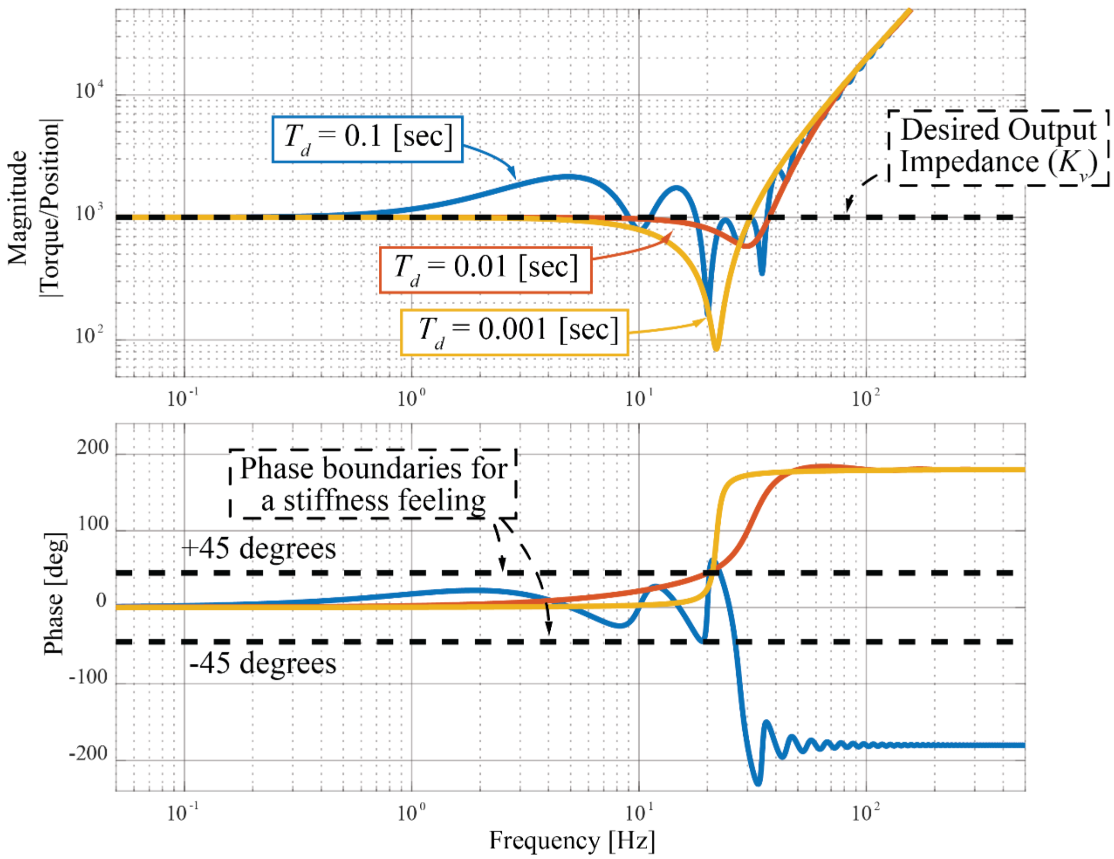

Figure 1.Hybrid actuator output impedance rendering a stiffness under varying time delays. The device performs normally while internal delays are small. As the sample times or time delays increase the output impedance begins to distort predominately the devices output impedance at higher frequencies (~10 Hz and above).

When rendering a virtual stiffness ($Z(s) = K_v$) and time delays or sample times are small the hybrid actuator displays the appropriate impedance until inertia distorts the output impedance. Distortion due to time delays begins to increase at higher frequencies as delays and sample times increase. In the case of virtual stiffness (Fig. 1), the low frequency or DC content is quite tolerant to delay. Distortion due to time delays also increases as the desired virtual stiffness differs from the physical brake stiffness. When the brake and virtual stiffness are the same, distortion due to time delay is zero because the active portion of the device is not producing force or torque.

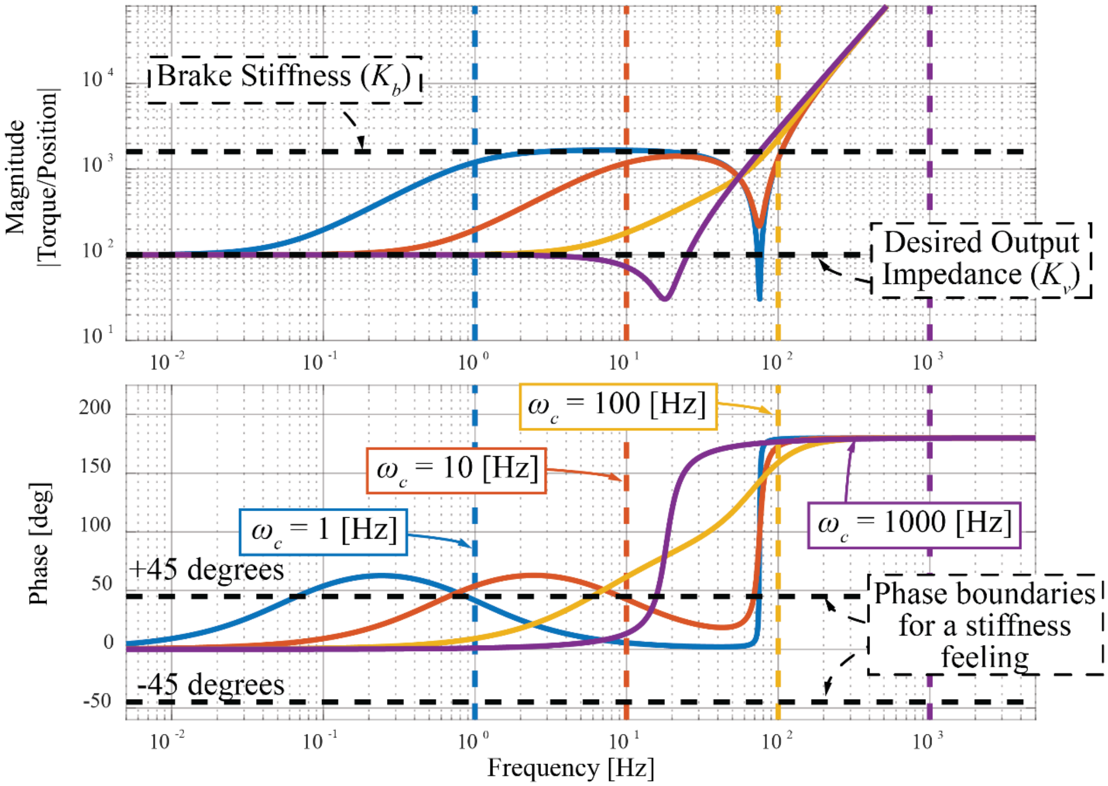

Figure 2.Hybrid actuator virtual stiffness output impedance varying brake filter bandwidth. If filter bandwidths are high the device performs normally. However, as the brake feedback filter bandwidth decreases below the virtual stiffness natural frequency the physical brake stiffness begins to distort the output impedance significantly.

Passive actuator feedback filtering also has the potential to distort a hybrid haptic device's output impedance. It does so in a similar way to time delay. If the device is attempting to render a virtual stiffness and passive feedback bandwidth is sufficiently high (generally greater than the system's natural frequency $\omega_n \sim sqrt(K_v/J)$) impedance distortion is not significant as seen in Fig. 2 . However, if the filter bandwidth is low distortion can be significant and the user will feel the brake's open loop output impedance above the filter bandwidth (represented here by K_b).

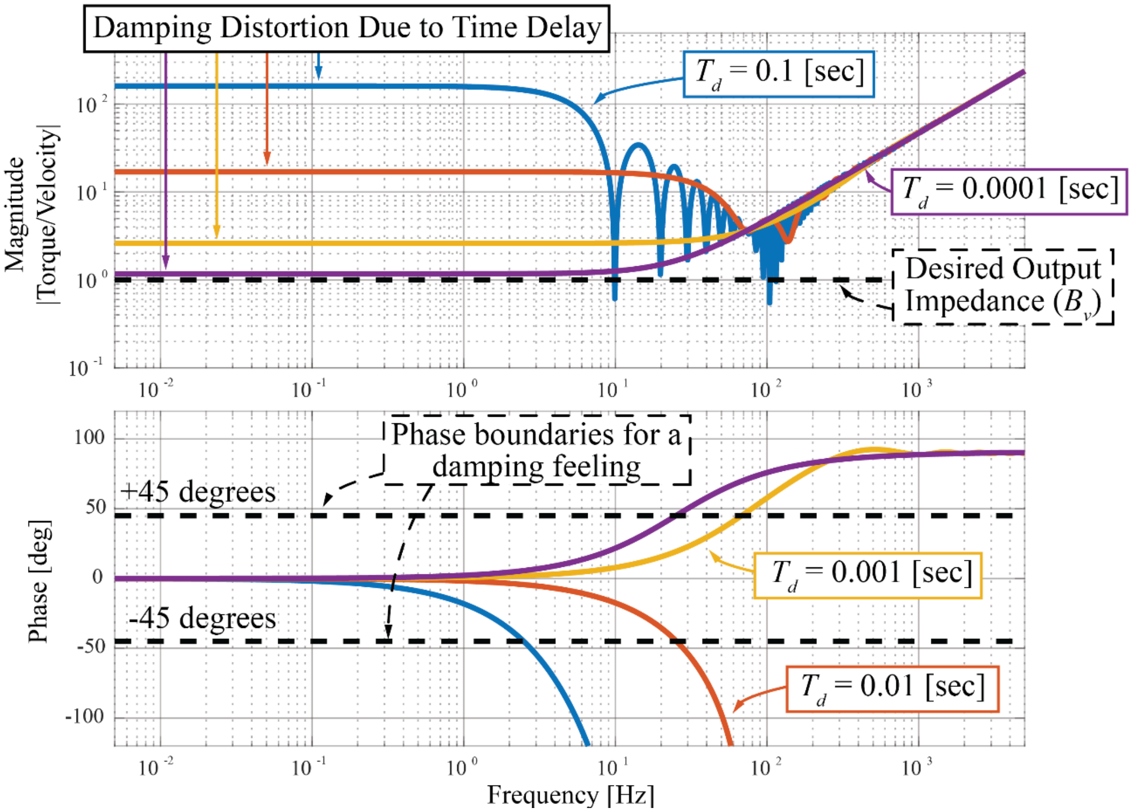

Figure 3. Hybrid actuator output impedance rendering a damper under varying time delays. The device produces the desired impedance at high sample frequencies but begins to generate excess damping in accordance with (9) when sample times or time delays increase.

It's interesting to note that when producing a virtual damper ($Z(s) = B_v s$ and Fig. 3) time delay impacts the output impedance at low frequencies by a factor proportional to (9) emphasizing the fact that damping is generated when actively canceling the passive actuator in both the virtual stiffness and virtual damping environments. When rendering virtual damping with finite filter bandwidth we find parallels to pure time delays. Again, low frequency damping distortion is always evident and can be seen visually in Fig 4. This effect can be quantified and the DC content of the (30) simplifies to (31). Filtered passive feedback can add significant damping to the devices output impedance as the feedback bandwidth decreases. This ultimately validates the analysis presented in Chapter 2 and is shown in and Fig 4.

$$\lim_{s\to 0}\left(\frac{\tau_h(s)}{\omega(s)}\right) = b + B_v + \frac{K_b}{\omega_c} \tag{31}$$

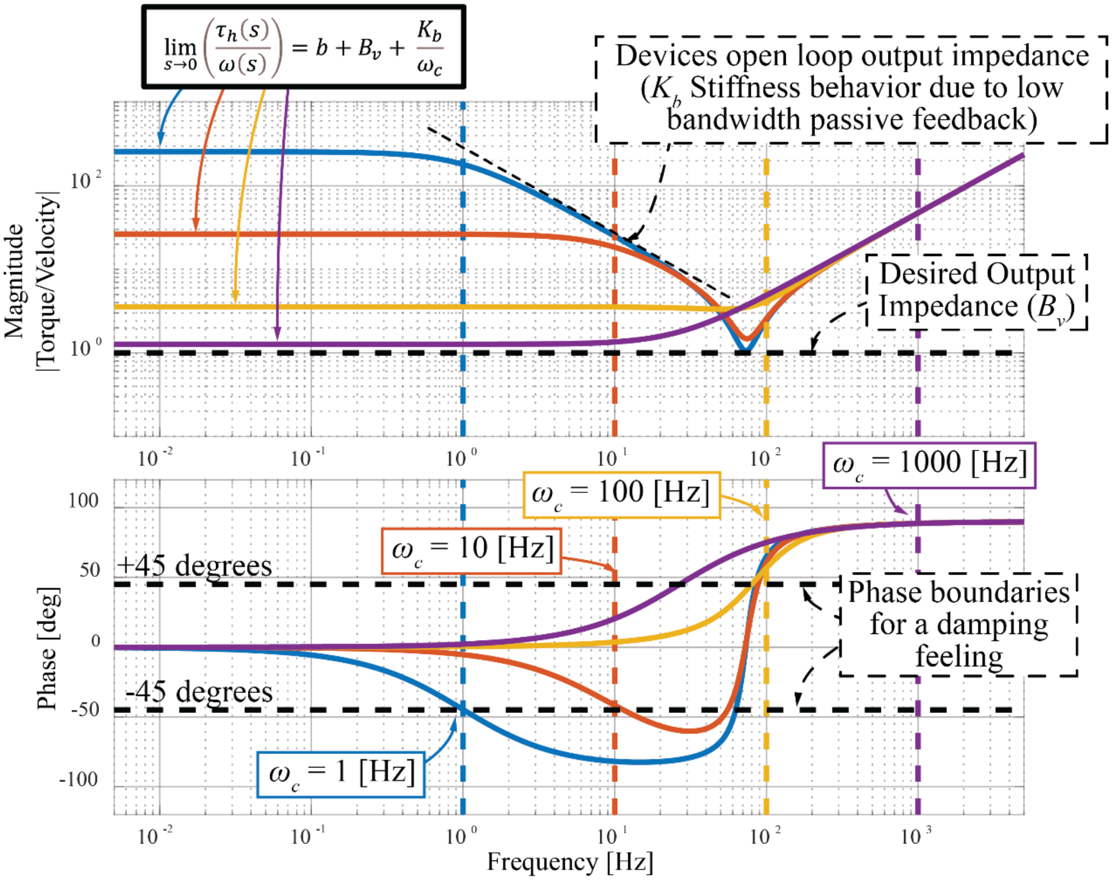

Figure 4. Hybrid actuator virtual damping output impedance varying brake filter bandwidth. The damping rendered to the user begins to distort at lower first order filter bandwidths according to (31). In general, the filter bandwidth must be high to accurately render a virtual damper.

Impedance distortion due to time delays, low sample frequencies and passive feedback filtering represent a limitation on the methods presented in the stability sections of this work. While the device can become more stable and the range of stable passive impedances can increase with a decrease in sample frequency or filter bandwidth, the hybrid actuators output impedance or how the device is intended to feel changes and may no longer render the intended impedance to the user.

B. Drive Train Compliance and Higher Order Modes

The actuator model presented in Chapters 1,2, and 3 lumps compliance in the system from the brake into a single spring element. While doing so is often a good assumption, compliance from drive train elements, the actuators, and robot structure itself can affect the validity of the simple model. Compliance can affect a haptic device's output impedance [1], stability [2][3], and as we will see even the intended function of the hybrid device.

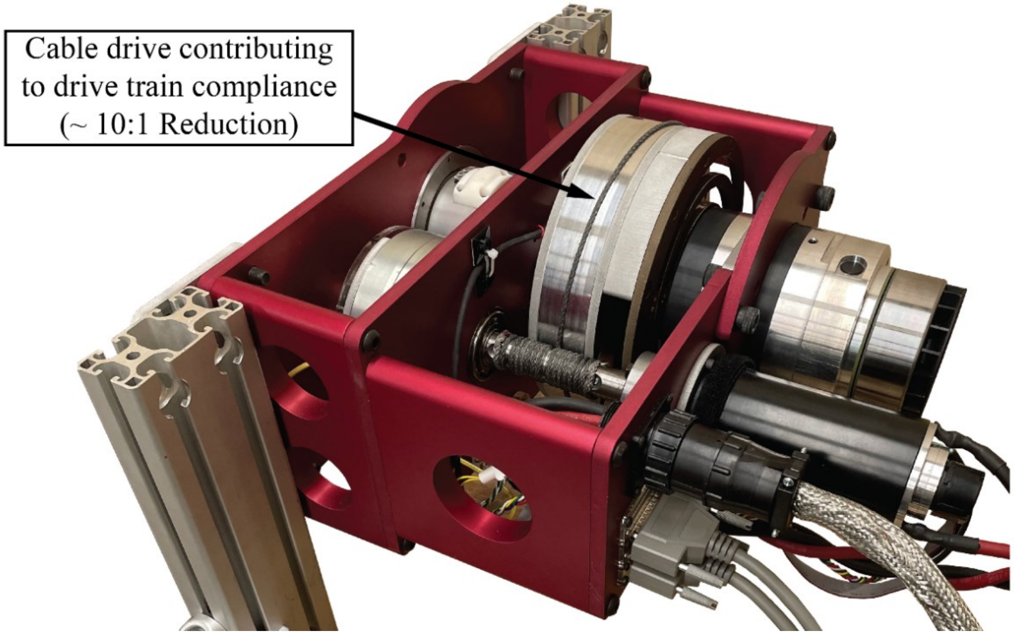

Figure 5. Large scale hybrid actuator cable transmission . Cable transmissions can lead to higher additional modes as actuators scale to larger formats which can impact actuator performance.

The effects of compliance and the resulting higher order modes become especially evident as actuators and robots increase in scale. For example, the large-scale balanced hybrid actuator, shown above in Fig. 5, was designed to output at least 100Nm of torque and drive a human leg scale parallel robot. The cable transmission uses a high strength and zero creep Vectran "rope" with a minimum braking strength of nearly 7000N. The 100Nm design point indicates the cable should experience static loads of no more than 360N. Despite the apparent cable overdesign, frequency response testing of the robot and transmission shows a mode at 40Hz as seen in Fig. 6.

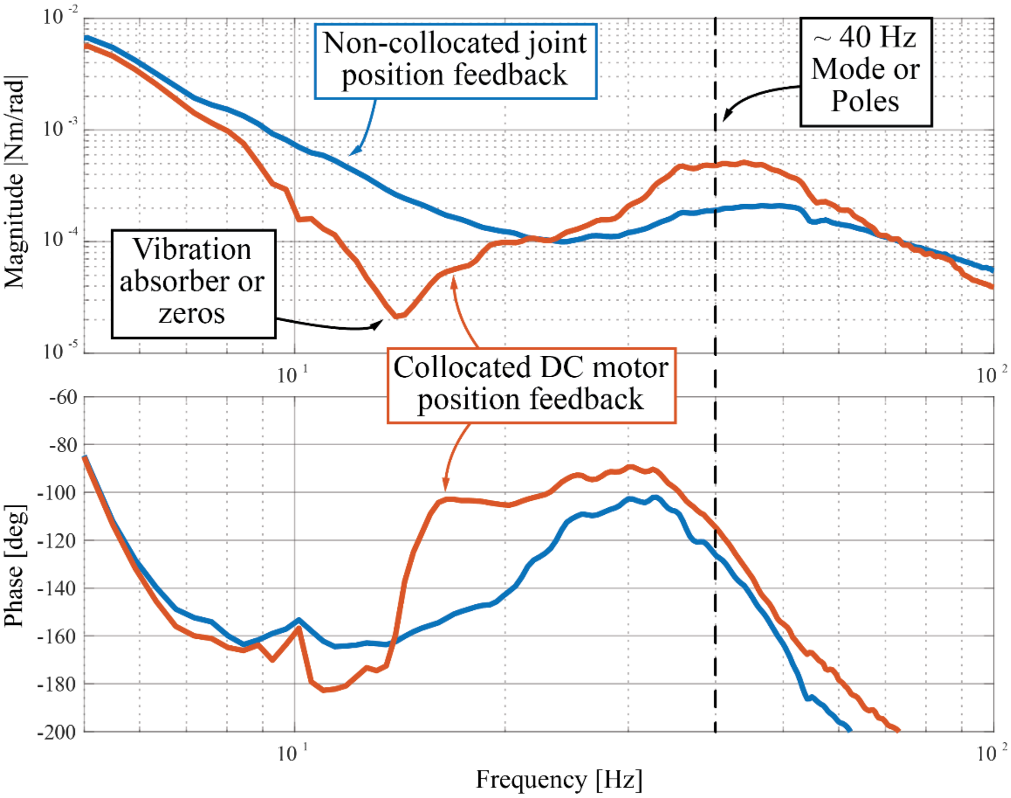

Figure 6. Collocated and non-collocated frequency response of the 2DOF robot. The frequency responses are from actuator 2 and show that the cable transmission has a mode at approximately 40 Hz in the robot pose tested. Modes will shift somewhat depending on the robot's pose due to changing linkage inertia.

Inspecting frequency responses from the capstan torque input to the capstan position and the capstan torque input to the robot joint position (collocated vs non collocated feedback), indicates the cable is stretching and can function as an additional compliant element in series with the brake stiffness. This behavior was difficult to reproduce in the handheld and desktop actuators where Vectran cables were also used and becomes more significant as devices scale to larger formats.

While at first inevitable additional compliance might seem benign, it can have significant impacts on the function of our hybrid actuation approach. When interacting with the large scale two degree of freedom device at frequencies below the cable transmissions mode the device functions as previously described, but the device can begin to function differently during high frequency interactions like hard tapping on a virtual constraint. In this case the DC motor is primarily responsible for torque contributions and must transmit them through the cable transmission. When doing so the cable transmission stretches slightly producing a small displacement opposing the human's disturbance (Fig. 7). The brake is directly coupled onto the capstan drive and the motion of the capstan due to the DC motor torque causes the brake torque to produce a torque contrary to the intended direction as seen in Fig. 7 and 8.

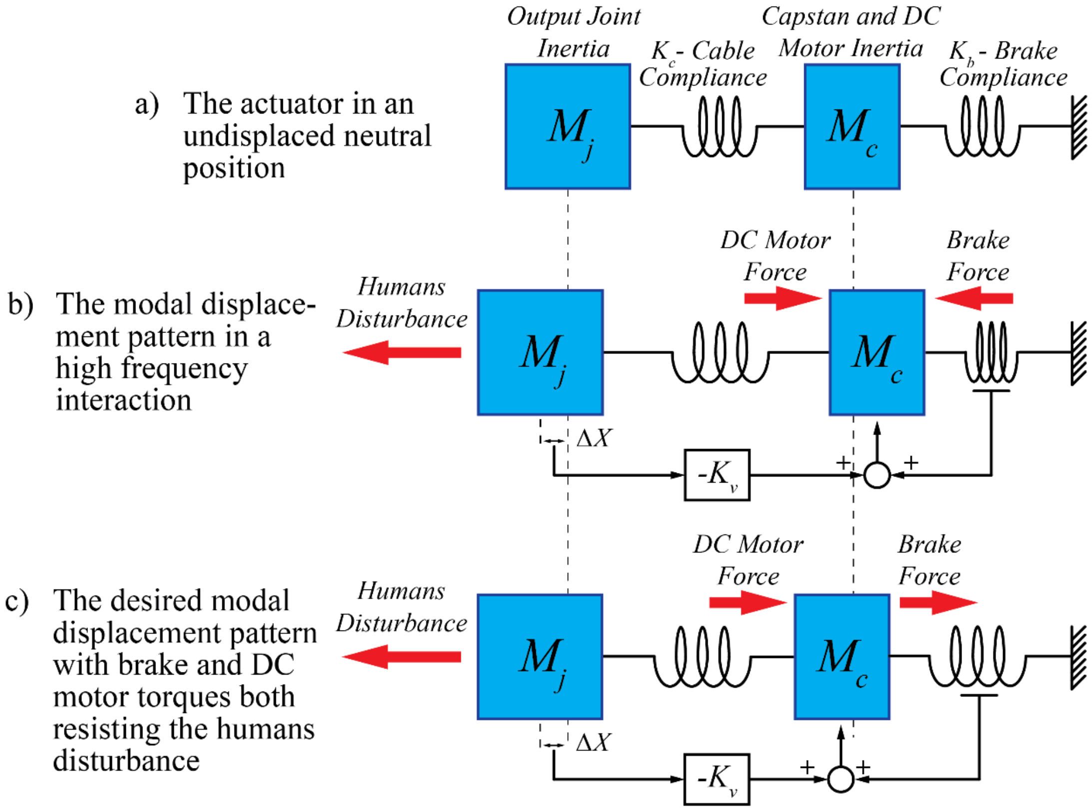

Figure 7. Schematic representation of a high frequency interaction with cable compliance. a) The undisturbed actuator. b) The actuator displacement during a high frequency interaction showing the cable compliance stretching and resulting in a brake force opposing the DC motor force. c) The desired displacement pattern with brake and DC motor forces aligned.

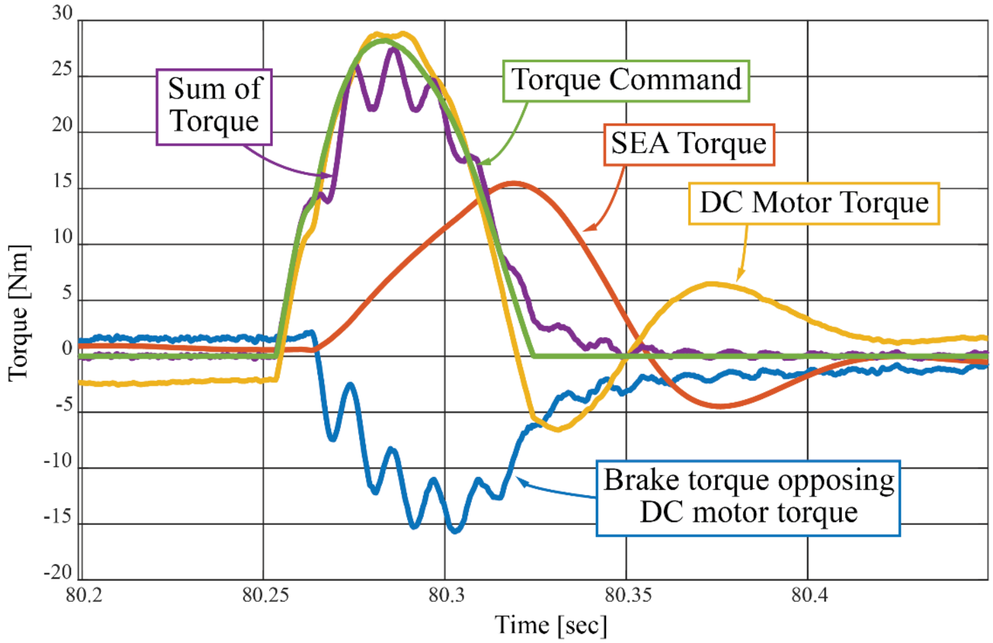

Figure 8. Actuator joint torque signals from the 2DOF robot during taps on a virtual wall. The cable transmission stretches and allows for unwanted brake motions and torques. The measured brake torque changes sign and opposes the intended torque. Additional oscillations show evidence of higher order modes in the feedback signal.

Using collocated position feedback in the model based passive partitioning control method might mitigate this behavior but could remove beneficial passive actuator torques due to the partitioning methods presented in Chapter 1. High bandwidth passive actuator torque feedback ensures the actuator produces the desired torque, but compliance can ultimately be a limitation on the intended function of the hybrid actuation concept especially as actuators scale to larger forces, torques, and workspaces.

References

[1] P. Dills and M. Zinn, “Transparent, High-Force, and High-Stiffness Control of Haptic Actuators with Backlash: A Multi Degree of Freedom Approach,” in *2024 IEEE Haptics Symposium (HAPTICS)*, Long Beach, CA, USA: IEEE, Apr. 2024, pp. 278–285. doi.

[2] M. Zinn, O. Khatib, B. Roth, and J. K. Salisbury, “Large Workspace Haptic Devices - A New Actuation Approach,” in *2008 Symposium on Haptic Interfaces for Virtual Environment and Teleoperator Systems*, Reno, NV, USA: IEEE, Mar. 2008, pp. 185–192. doi: 10.1109/HAPTICS.2008.4479941.

[3] D. P. Losey, A. Erwin, C. G. McDonald, F. Sergi, and M. K. O’Malley, “A Time-Domain Approach to Control of Series Elastic Actuators: Adaptive Torque and Passivity-Based Impedance Control,” *IEEE/ASME Trans. Mechatron.*, vol. 21, no. 4, pp. 2085–2096, Aug. 2016, doi: 10.1109/TMECH.2016.2557727.

Chapter 6: Hybrid Actuation in Human Friendly Robotics

To address the limitations of existing actuation and enable human-robot applications that require high force and high power while also maintaining the physical characteristics important for safe and effective physical interaction we propose the use of a balanced hybrid actuation approach [1], [2], conceptually shown in Fig. 1. In prior work we have shown that balanced hybrid actuation can increase the rendering range of kinesthetic haptic devices. In this section, we extend the application of balanced hybrid actuation to general physical human-robot applications and investigate its potential benefits regarding performance and safety.

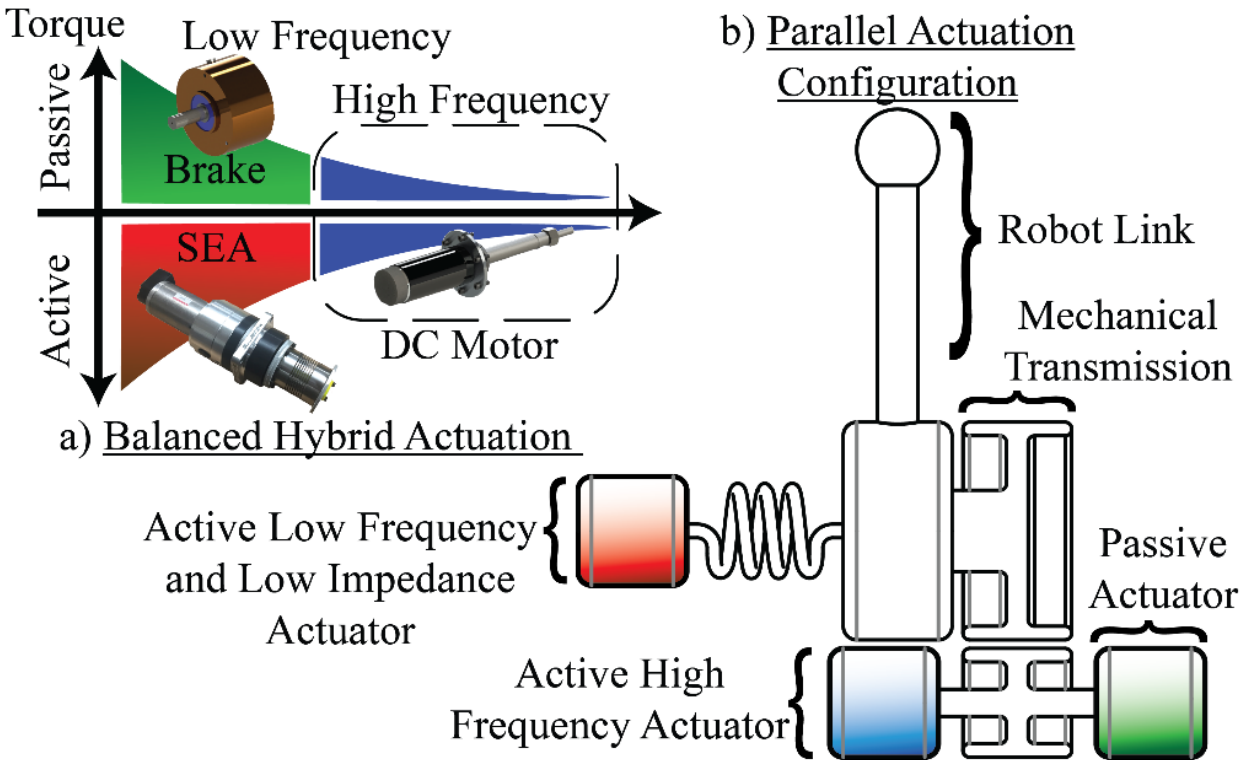

Figure 1. Balanced hybrid actuator concept. The balanced hybrid actuation concept: active and passive torque partitioning as a function of frequency and the active vs. passive torque contributions. b) Overview of the balanced hybrid active-passive actuation approach.

A. Balanced Hybrid Actuation Concept for Physical Human Robot Interaction

Balanced hybrid actuation combines energy-absorbing high-force low impedance passive actuation, high power low impedance active compliant actuation, and active high frequency actuation together. Balanced hybrid actuation improves upon prior hybrid actuators by not only providing a large range of active and passive force magnitudes, but a large frequency range of active and passive torques.

In the context of human-robot interaction, passive actuation helps to reduce power consumption, aid in servoing movements, and safely increase the dissipative power capability of the actuator. The inclusion of active compliant actuation and a high frequency active actuator provides large bandwidth active torque capabilities and may be used to compensate for slower response speeds and nonlinearities typical of passive actuators while maintaining low output impedance, essential for safety. A key component to our balanced hybrid actuation concept is the constructive combination of all three actuators in parallel, made possible by the low output impedance characteristics of each element of the combined hybrid actuation. The combined actuation is balanced in regard to frequency, providing low-impedance actuation over a wide bandwidth, and in regards of torque production, providing high active and passive torque and power output. Finally, the low output impedance of the combined actuation approach greatly reduces impact loads during uncontrolled collisions, essential for safe human- robot interaction.

1. One Degree of Freedom Testbed

A one degree of freedom actuation testbed, shown in Fig. 2, was constructed to evaluate the balanced hybrid actuation concept. The testbed incorporates a (1) series elastic actuator (SEA) as the high power, low impedance active compliant actuation, (2) a particle brake as the energy-absorbing, high-force, low impedance passive actuation, and (3) a low-inertia DC motor as the fast, low-power active actuation.

High-power active actuation: Series elastic actuators, such as the one used in our evaluation testbed, incorporate a compliant element at their output and use feedback to create a low-impedance torque source, effective below the SEA's closed-loop bandwidth, while the compliant element ensures low output impedance at high frequency (important for safety). In our testbed, the SEA torque is derived from a DC motor in series with a high-ratio speed reducer. The high-ratio speed reducer helps to increase the power density of DC motor by allowing the DC motor to operate at higher speeds while the SEA compliance and feedback control reduces the output impedance of the DC motor and speed reducer to safe levels.

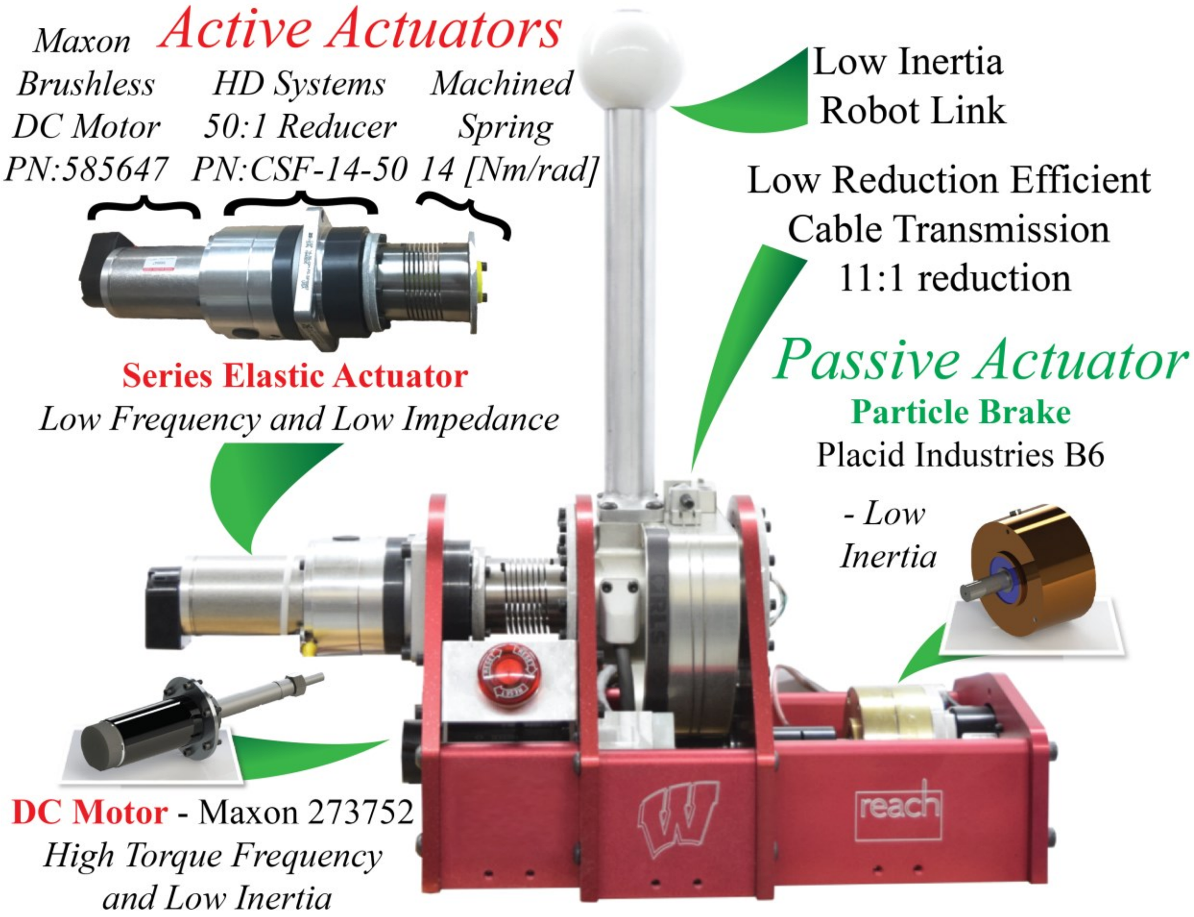

Figure 2. Desktop scale balanced hybrid actuator. A one degree of freedom balanced hybrid actuation test bed with a SEA, brushed DC motor, and particle brake arranged in parallel used to explore the actuation concept.

High-power passive actuation: Including the particle brake at the output allows for a broad frequency range of passive torques of a similar magnitude to the SEA. However, a particle brake's response time is generally slower than DC motors. Consequentially, the brake is primarily responsible for producing lower frequency passive torques. Particle brake rotors have similar inertial properties to DC motors and consequently do not significantly impact the links inertia and safety of the actuator.

Fast, low-power active actuation: Series elastic actuators are most effective as low impedance torque sources below the flexible mode frequency introduced by the series elastic element while particle break's are limited by their relatively slow response time. To combat this effect, we include a small DC motor to recover high-frequency capability.

The DC motor is primarily responsible for high frequency content that the SEA and particle brake are unable to produce. The reflected inertia of the small DC motor has been shown to have little impact on robot safety in [3], if an efficient and low reduction speed reducer is used. We chose a stiff and efficient 11:1 cable reduction, Fig. 2, which connects each component in parallel. The direct connection to the output link allows the DC motor to produce torques above the SEA's flexible mode.

In the following sections we use the testbed described above to explore the potential benefits of the proposed actuation approach. We describe a candidate control approach in section B, explore performance benefits in section C, and explore safety characteristics in section D.

B. Hybrid Actuator Position Control

Many tasks performed by cooperative robots today are pick and place operations such as loading or unloading a machining center or moving items from one conveyer belt to another. These actions are at their core tracking and position control problems. Our hybrid actuator needs a control strategy that can address the redundant and nonlinear nature of our actuator and yield a high level of tracking performance while allowing us to explore its advantages. In trajectory tracking often the feed forward path contributes the majority of the control effort to actuators. Consequently, utilizing the passive actuator in feed forward control allows us to capture much of its tracking benefits while avoiding potential problems resulting from including a nonlinear actuator in our feedback control path. To this end we have implemented a control approach that incorporates feed forward control, leveraging the torque capabilities of all three component actuators, in combination with an active-only feedback controller. The active-only state feedback controller is tuned using a solution to the infinite-horizon Linear Quadratic Regulator (LQR). A high-level block diagram showing the control structure is shown in Fig. 3.

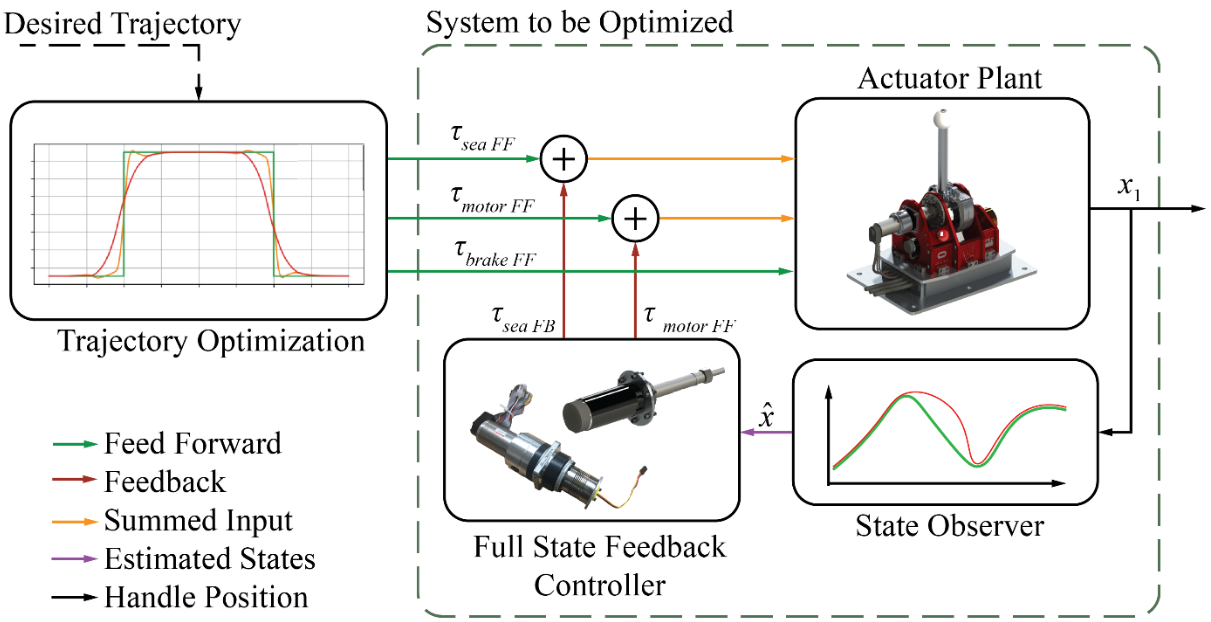

Figure 3. Hybrid actuator tracking control structure. Feedback control only consists of the active portions of the full balanced system. The hybrid actuator optimal feed forward utilizes the brake to enhance the system's operation. The optimization algorithm used to generate feed forward torques includes the physical dynamics of the actuator and the dynamics of the feedback controller.

1. Hybrid Feed Forward Control by Trajectory Optimization

To evaluate the proposed balanced active-passive actuation, it is instructive to examine specific tracking scenarios where its inherent characteristics suggest that it could provide significant benefits. However, we cannot rely on classical control techniques to formulate the specific feedforward torque profiles for the component actuators due to the nonlinear nature of hybrid actuation.

Instead, we turn to optimal control and, more specifically, an offline trajectory optimization method known as direct collocation, described in more detail in Appendix D. Trajectories generated with direct collocation can be computationally costly, but not prohibitively so, making the approach suitable for fast, offline computation. For example, for the trajectories generated in this work (spanning motions of up to 4 seconds), did not exceed 30 seconds of the computation time when computed on a standard desktop computer. Using direct collocation, the actuation feed forward signals in this paper were pre-computed offline and applied online via interpolation and a lookup table. Online disturbance rejection is mainly left to the active actuators LQR controller.

C. Hybrid Actuator Tracking Performance

To explore the potential benefits of the proposed hybrid actuation approach, we investigate three specific tracking scenarios including the following:

Time Optimal Control: Investigate improvements in time to target performance resulting from large high-power passive decelerations.

Minimum Energy Control: Investigate potential energy savings and/or control efficiency resulting from the low energy costs of the passive actuation.

Tracking Error–Control Effort Tradeoff: Explore hybrid actuation control with a more traditional LQR based cost function.

1. Time Optimal Control

Hybrid actuators could help to enable high power high force cooperative robotics because of their ability to create large dissipative forces. Enabling a robot to decelerate faster could increase the capability of a robotic manipulator in terms of its achievable trajectories and the maximum power flow that it can achieve. Furthermore, hybrid actuators do this while maintaining a high level of safety because they are an inherently low inertia actuator.

A convenient way to observe this impact of the hybrid actuator is through what is known as time optimal control. Time optimal control problem finds a trajectory that moves the systems initial states, point "A", to a final state, point "B", in the minimum amount of time. Actuation saturation limits must be included to make the problem well posed. In the spirit of our balanced hybrid actuator we assumed the combined active actuators and passive actuators have equal saturation points (i.e. 1 Nm for active and passive). Trajectories resulting from time optimal control of our hybrid actuator are compared to the active only portion of our actuator in Fig. 4

Unsurprisingly, the hybrid actuator arrives at its destination point "B" faster than the active only actuator. The hybrid actuator does so by taking advantage of the dissipative torque capability of the passive actuator. Plotting mechanical power flow at the robot's link shows the hybrid actuator's trajectory achieved a dissipative mechanical power flow nearly double the active actuators. This occurs during the deceleration phase of the hybrid actuators trajectory and is due to the slightly increased peak handle velocity and because of the greatly increased braking capability of the hybrid actuator. The time optimal control formulation shows that it is advantageous to use the passive component of hybrid actuators to safely achieve high power dissipative movements like decelerating a large mass; which could be essential to the performance of high power high force cooperative robots.

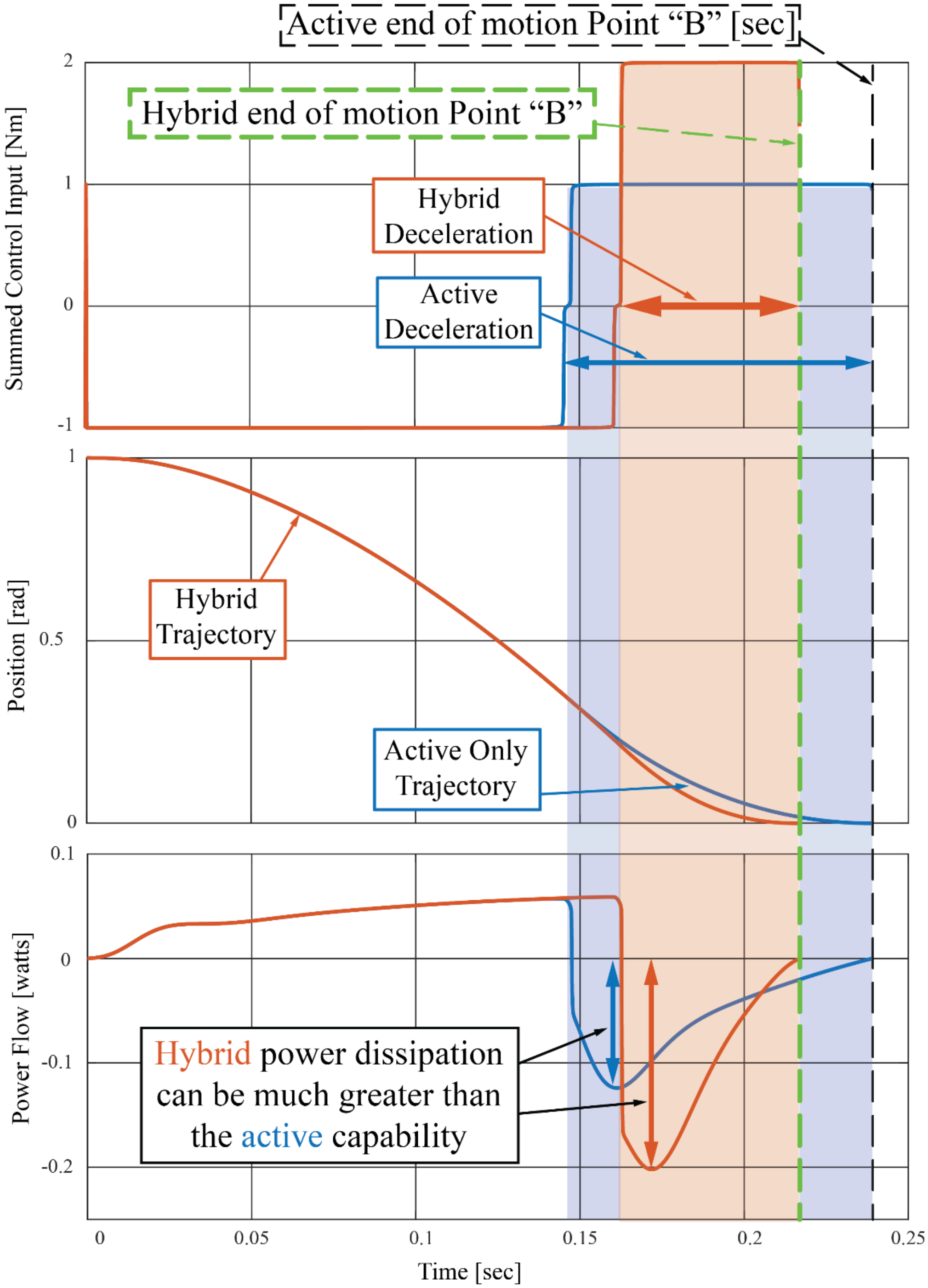

Figure 4. Time optimal control trajectories and torques.. Active only and hybrid time optimal control profiles generated via trajectory optimization. The hybrid actuator moves from point "A" to "B" faster than the active actuator and achieves a higher power movement while decelerating.

2. Minimum Energy Control

Another potential benefit of our balanced hybrid actuator are the energy savings that passive actuators can achieve. That is to say, when properly controlled a hybrid actuator achieves a given trajectory more energy efficiently than a traditional active actuator (see Fig.5). Minimum energy control or minimum effort control provides a framework to reduce the energy usage of the actuator as a whole while tracking a trajectory. The method minimizes the weighted sum of the actuators control effort squared [4] and is explained in greater detail in Appendix D. We chose a sine wave as a representative trajectory to show the energy saving benefits of our hybrid actuator. Comparing the summed squared actuation costs and the integral of each actuator's instantaneous power magnitude, Table 1, shows the hybrid actuator can achieve the desired trajectory more efficiently in terms of both the minimum control effort cost function and in terms of actual total mechanical energy transferred by the actuator. As shown in Fig. 5a and b, the passive actuator is contributing almost half the torque that the DC motor would otherwise be contributing. Again, we see it is advantageous to use the passive actuator, this time in terms of energy, to decelerate the robot's link.

TABLE 1: Active-only and Hybrid Minimum Energy Control Costs for a 5Hz Trajectory.

Actuation Type	Min. Cost Function Evaluation	Integral of absolute value of mechanical power
Active Only (SEA and Motor)	~10300	4.5623 [joules/per cycle]
Hybrid (SEA, Motor, and Brake)	~7000	3.2431 [joules/per cycle]

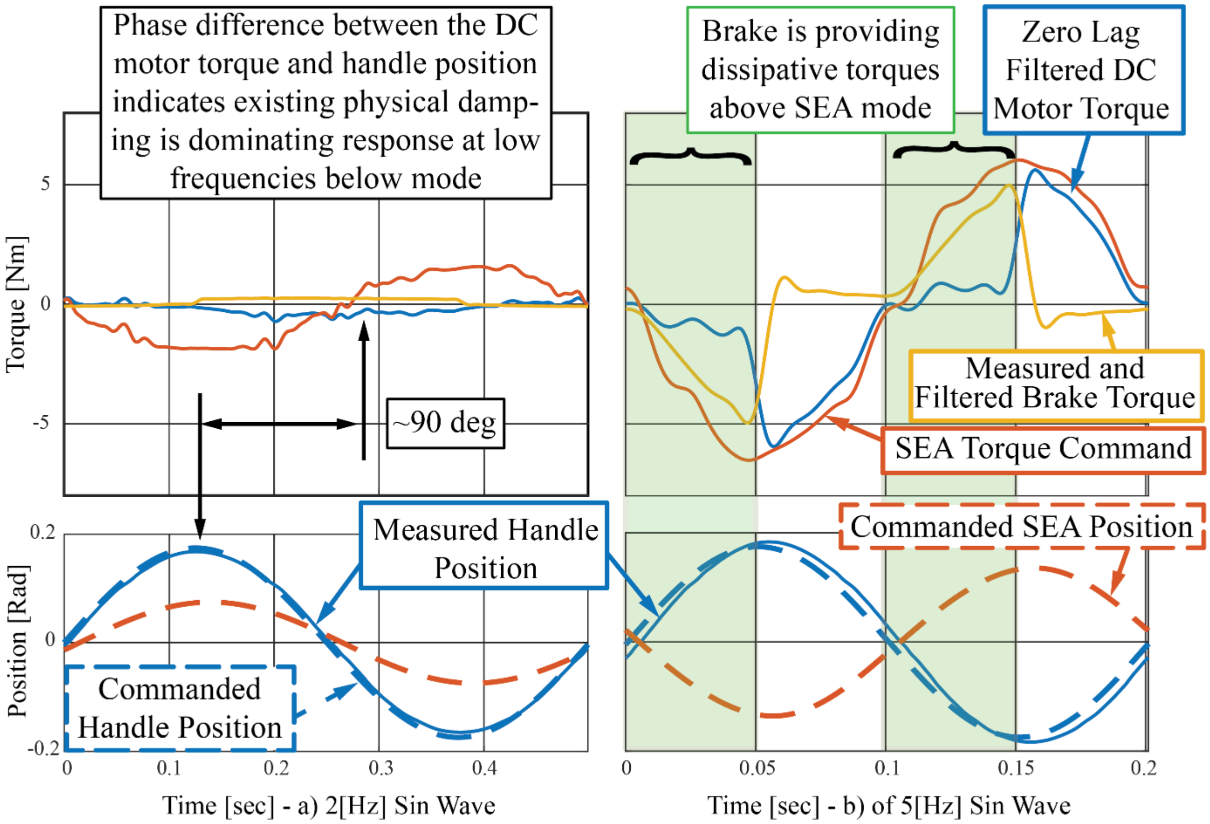

Figure 5. Minimum energy control trajectories and torques.. Comparison of experimental tracking of a sine wave using minimum energy control actuator outputs compared to the optimization output. a) The 2 Hz trajectory is below the flexible mode, or natural frequency, of the SEA. b) The 5 Hz trajectory is above the SEA flexible mode. The 5 Hz trajectory shows how the DC motor and brake begin to dominate the actuators torque response at higher frequencies. Results were obtained using active actuators in the feedback loop for disturbance rejection. A zero-lag low pass filter is applied to the torque waveforms after data collection.

Frequency partitioning between actuators, shown in Fig.5 and Fig.6, is an interesting consequence of minimizing actuation effort. Results show, it is most efficient to use the SEA as a low frequency torque source below its mode. The brake does not contribute significantly at low frequency either, for this specific trajectory, because the actuator is primarily overcoming internal damping. Consequently, the phase of the DC motor at 2 Hz is approximately 90 degrees out of phase with the handle position. In the case of sine wave trajectories, the brake and DC motor work together to generate higher frequency torques above the SEA's flexible mode. It is important to note, that the high frequency content of the brake is limited in reality as is indicated in Fig. 3. The results presented in Fig. 6 are obtained directly from the optimization output which does not account for high frequency limitations on both the DC motor and the brake. In summary Fig.6 shows a clear interplay between low and high frequency actuators which is advantageous to high power and high force cooperative robots. Splitting torques between the brake and DC motor is also effective at reducing actuation and energy costs while tracking a given trajectory.

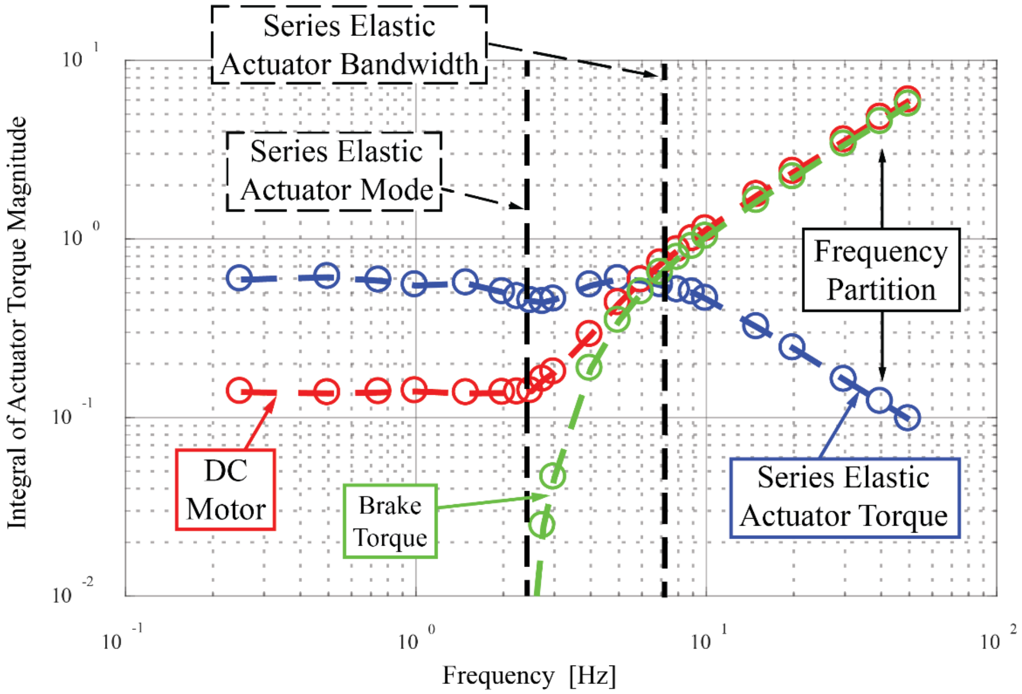

Figure 6. Actuator frequency partitioning due to minimum effort/energy control. Minimum effort/energy control (plotted integral of the absolute value of each actuators torque contribution from a single sine wave cycle). Note, the brake and DC motor nearly split the actuation costs equally above the SEA flexible mode.

3. A Tradeoff Between Tracking and Control Effort – LQR

Thus far, we have seen hybrid behavior take advantage of the dissipative attributes of the passive actuator to decelerate the robot link. However, it can be advantageous to use the passive actuator prior to and during the acceleration phases of trajectories. As we will show, the SEA and particle brake can work together to store potential energy in the SEA's compliant element which in turn can be used to increase resulting tracking acceleration. This synergistic behavior is of particular interest because it allows the system to track trajectories that required rapid accelerations, beyond the capabilities of each actuator individually.

To investigate this potential synergy, we can use a feed forward optimization approach inspired by LQR control where the optimization cost function trades off tracking error and control effort. By heavily weighting the handle position error in the cost function, the actuator will track a specified trajectory while creating a feasible trajectory in the process as shown in Appendix D.

Using this feed forward formulation, it is interesting to examine the behavior of the hybrid actuator when attempting to track a square wave, the experimental results of which are shown in Fig. 7. The brake is used during both the acceleration and deceleration phases of the approximate square wave and during low velocity portions of the trajectory. Interestingly, during the pre-acceleration phase energy is stored in the SEA spring by using the brake to hold the handle in place at the tracking reference while the SEA servos forward towards the new equilibrium position. The brake then releases the stored spring energy. Following this, a high frequency free movement handle acceleration phase occurs where the DC motor supplies some high frequency torque. Finally, the brake is engaged, dissipating energy which decelerates the link. As the overall balanced hybrid actuation concept suggests, the brake and SEA are primarily working together to produce the desired motion while the DC motor fills in where the other actuator's dynamics are too slow or where it is not desirable to use the SEA or brake.

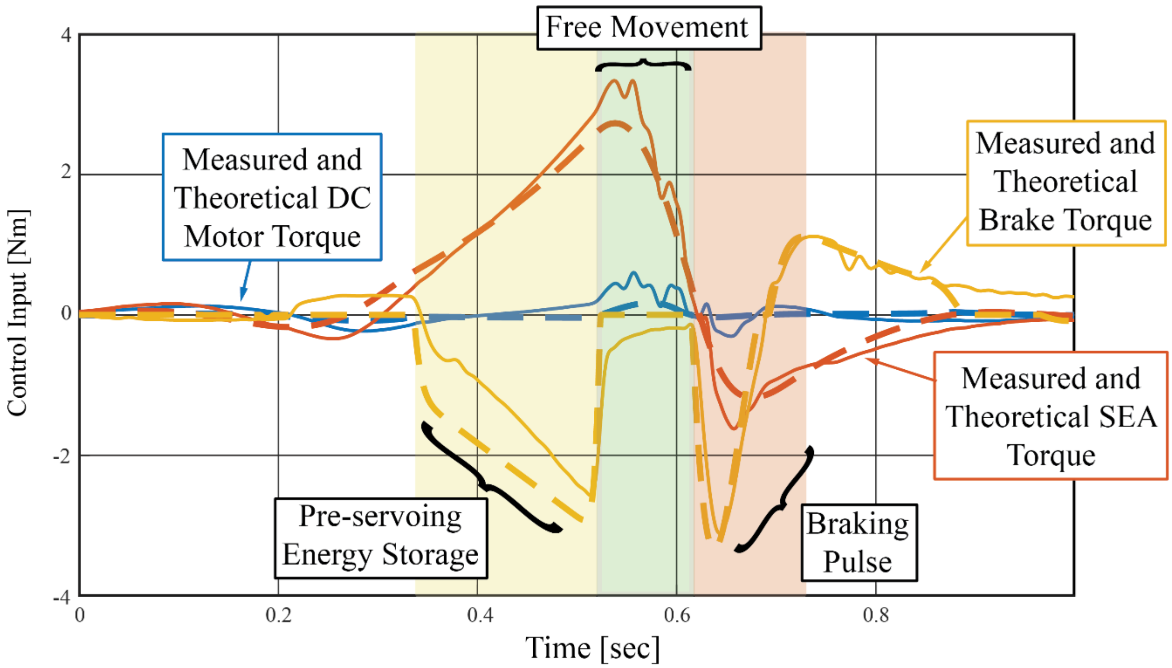

a) Theoretical and experimental torque response

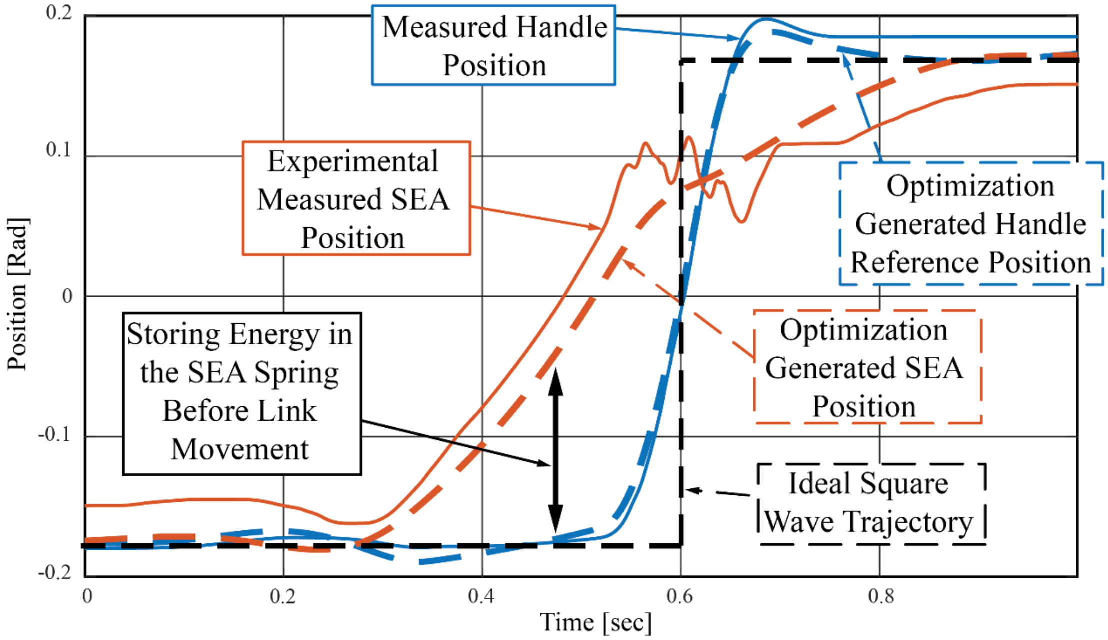

b) Position response through half of a square wave

Figure 7. Actuator trajectories resulting from LQR based cost function. Experimental (solid lines) and optimization results (dashed lines) (a) Each actuators torque contribution (b) tracking a square wave using a LQR based cost function (Unmodeled gravity and friction disturbances cause the steady state error at the end position).

In addition to the benefits described, the synergistic behavior between the brake and SEA at low frequencies can be used to help to solve velocity saturation problems common to SEA [5]. In fact, we can accentuate the interplay between the SEA and brake by penalizing the SEA mass velocity in our cost function. The result is a slower SEA position response while maintaining the desired fast output position response. Avoiding SEA velocity saturation is achieved by storing more energy in the SEA spring and as a result higher brake activation levels prior to the output link movement.

D. Hybrid Actuator Safety Evaluation

Clamping and blunt impacts are the predominate methods by which robots injure people [6]. Clamping injuries occur in robot joints or with robots against another object. Impact injuries arise from high inertia robots impacting people at high velocity and will be the focus of the safety study in this work. Research investigating these impacts has shown that the reflected inertia of an actuator contributes significantly to the safety of a robot overall and reducing the reflected inertia can help to make a robot safer especially at high velocities. The design of a SEA directly addresses this safety risk by introducing a series elastic element between the load (i.e. robot link) and the actuator, significantly reducing the effective inertia of the actuator (in regards to impact) and is widely considered a safe robotic actuator [7].

Our proposed combined active-passive hybrid actuator differs from a SEA actuator with the addition of a small DC motor and passive actuator. Previously it has been shown [3] that adding a small DC motor in parallel with an SEA actuator can be accomplished without degrading the impact safety of a manipulator, assuming that the small motor and its associated reduction have low reflected inertia, as is the case with the actuation approach proposed here. The question remains whether adding a passive actuator might affect impact safety. To this end, we have conducted an experimental impact test which compares the active portion of the balanced hybrid actuation concept to the full hybrid actuator. The results of the experiment are used to validate an impact simulation. The active and hybrid actuator impact simulation is repeated on a full-size collaborative robot to study impact safety under more realistic conditions.

1.Hybrid Actuator Impact Experiment and Validation

The impact test set up, shown in Fig. 8, consists of a weighted pendulum instrumented with an encoder (US digital PN:E5-5000-375-IE-D-H-D-B) and an accelerometer (Analog devices PN:EVAL-ADXL325Z). The pendulum also includes a leaf spring to augment the interface stiffness between the robot link and the pendulum.

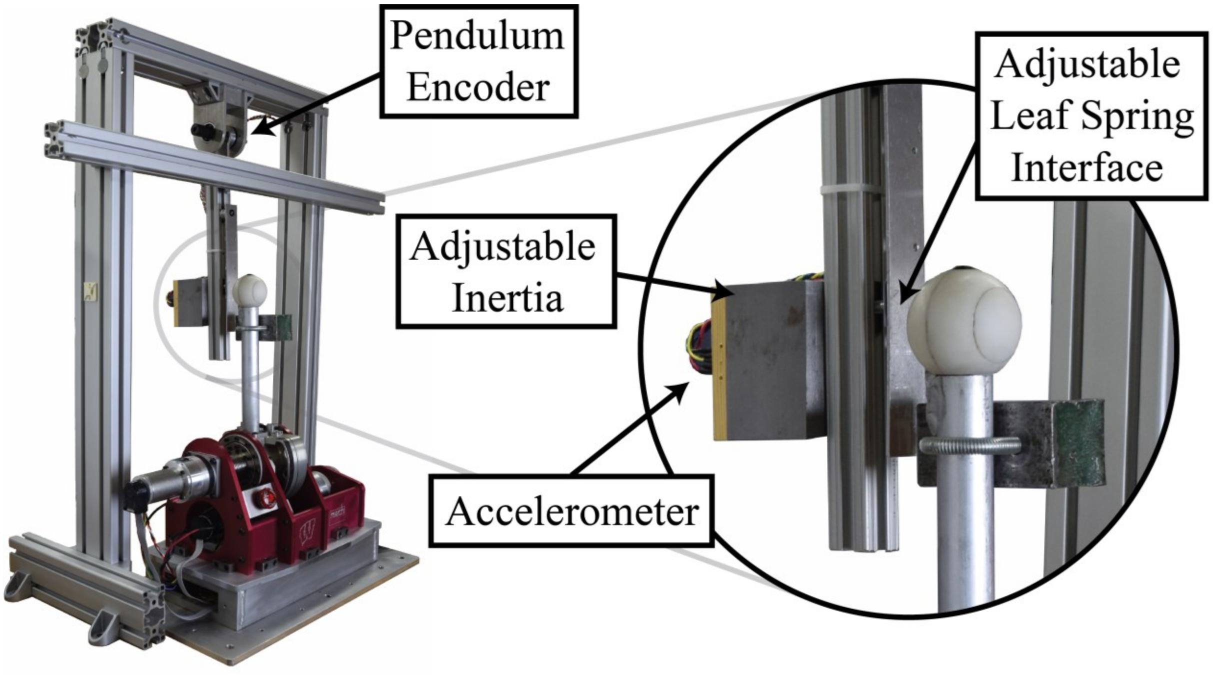

Figure 8. Hybrid actuator impact test setup with instrumented pendulum. The hybrid actuator includes an attached weight and is set up to impact the leaf spring at a prescribed point. The pendulum was instrumented with an accelerometer to measure the resulting impact accelerations, an adjustable inertia and adjustable leaf spring to change the interface stiffness of the collisions.

During the impact tests the robot was controlled using the minimum energy or effort control approach described previously, such that the impact velocity was constant over the set of tests performed. The testbed position trajectory was set to ensure that the passive actuator was engaged at the moment of impact. To evaluate the effect of the passive actuator (i.e. particle brake) on impact safety, we compared the impact results of the full hybrid actuator to that of the active portion alone. During the active-only experiment the particle brake was physically decoupled.

As seen in Fig. 9, the acceleration of the pendulum following impact with the full hybrid actuator testbed as compared to the acceleration following impact with the active only testbed are approximately equal, demonstrating that the addition of the passive actuator has little effect on the peak measured acceleration.

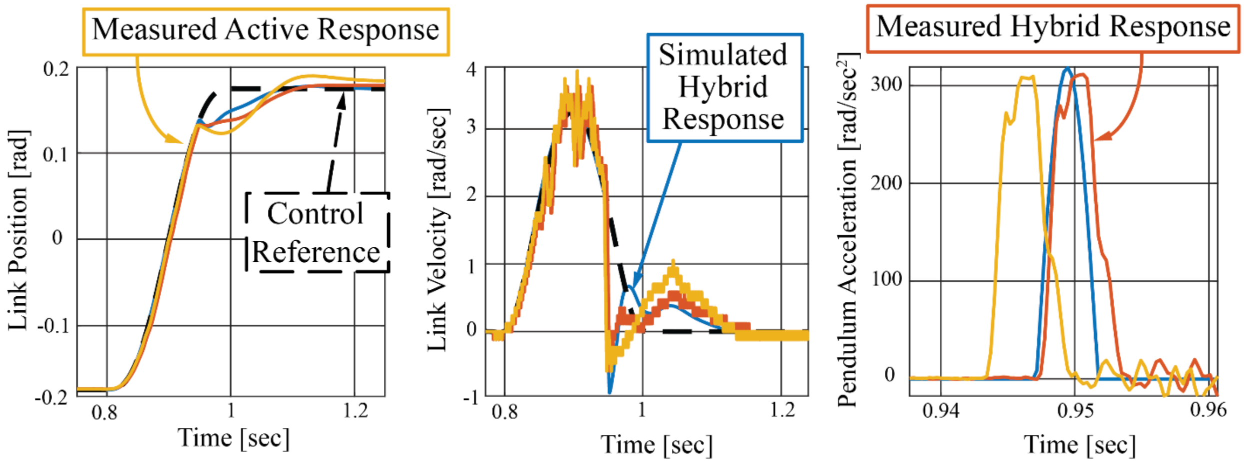

Figure 9. Comparison of active only balanced hybrid and simulation impacts. Hybrid actuator and the active only actuators collisions generate nearly identical acceleration profiles.

2.Balanced Hybrid Cobot Impact

While the test results are informative, the impact safety of a full size hybrid robot and human tissue is still in question. To address this, we developed a simulation, validated using the test results described above (see Fig. 9), with parameters set to represent a head impact with a full-size collaborative robot, in this case a universal robots UR5 configured in its home position. A human head and skull stiffness are estimated at 6 kg and 37000 kg/m, respectively, and are used as the impacted mass and interface stiffness, respectively [8]. Finally, the SEA stiffness and inertia were calculated and set in accordance with the guidelines from [9]. The head acceleration profile, and peak acceleration are shown in Fig. 10. In addition, the Head Injury Criteria (HIC) [6], a common metric used to assess the likelihood of serious head injury, was evaluated to allow a direct comparison of the actuation impact characteristics.

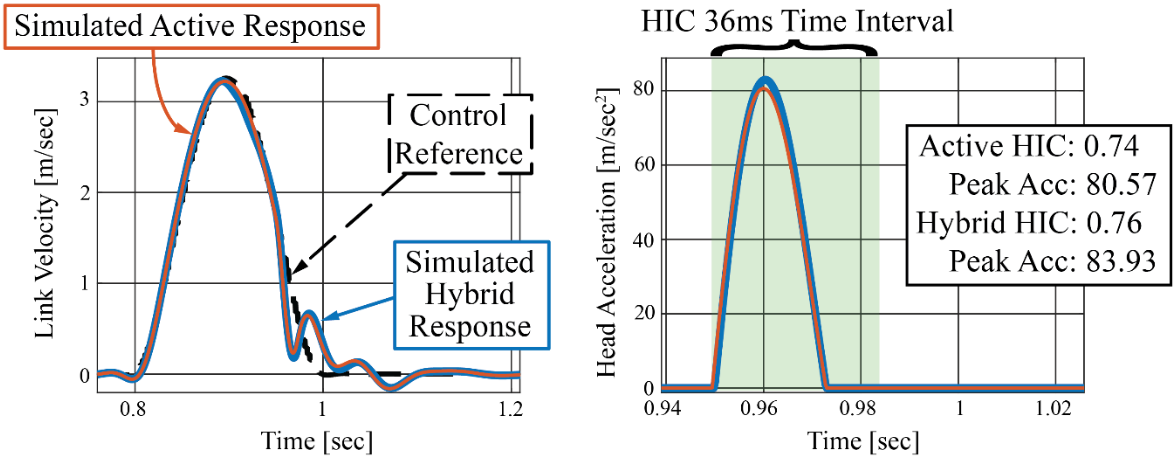

Figure 10. Hybrid cobot impact simulation. Simulated head acceleration profile resulting from full size active and hybrid cobot collision.

As seen in Fig. 10, the simulation demonstrates that for an average human head and skull stiffness the hybrid actuator performs nearly identically to the active only cobot in terms of the resulting peak acceleration and HIC.

References

[1] P. Dills, C. Parthiban, I. Fufuengsin, and M. Zinn, “Design and Analysis of a High Performance Impedance Based Hybrid Haptic Interface,” p. 3, 2018.

[2] C. Parthiban, P. Dills, I. Fufuengsin, N. Colonnese, P. Agarwal, and M. Zinn, “A Balanced Hybrid Active-Passive Actuation Approach for High-Performance Haptics,” in *2019 IEEE World Haptics Conference (WHC)*, Tokyo, Japan, Jul. 2019, pp. 283–288, doi: 10.1109/WHC.2019.8816146.

[3] M. Zinn, B. Roth, O. Khatib, and J. K. Salisbury, “A New Actuation Approach for Human Friendly Robot Design,” *Int. J. Robot. Res.*, vol. 23, no. 4–5, pp. 379–398, Apr. 2004, doi: 10.1177/0278364904042193.

[4] J. Klamka, *Controllability and Minimum Energy Control*, vol. 162. Cham: Springer International Publishing, 2019.

[5] D. W. Robinson, “Design and analysis of series elasticity in closed-loop actuator force control.” Massachusetts Institute of Technology, Cambridge, MA, USA, 2000.

[6] S. Haddadin, A. Albu-Schaffer, and G. Hirzinger, “The role of the robot mass and velocity in physical human-robot interaction - Part I: Non-constrained blunt impacts,” in *2008 IEEE International Conference on Robotics and Automation*, Pasadena, CA, USA, May 2008, pp. 1331–1338, doi: 10.1109/ROBOT.2008.4543388.

[7] S. Robla-Gomez, V. M. Becerra, J. R. Llata, E. Gonzalez-Sarabia, C. Torre-Ferrero, and J. Perez-Oria, “Working Together: A Review on Safe Human-Robot Collaboration in Industrial Environments,” *IEEE Access*, vol. 5, pp. 26754–26773, 2017, doi: 10.1109/ACCESS.2017.2773127.

[8] D. Shin, “A New Actuation Approach For Bio-Inspired Human-Freindly Robots.” Stanford University, Stanford, CA, USA, 2011.

[9] P. Dills, C. Parthiban, I. Fufuengsin, and M. Zinn, “Design and Analysis of a High Performance Impedance Based Hybrid Haptic Interface,” p. 3, 2018.

Conclusions and Future Directions

The parallel and balanced hybrid actuation approach presented here both extends the dynamic range of haptic devices and increases the capabilities of a cooperative robot across an increased range of force and workspace sizes. It does so while remaining naturally low impedance and safe.

A. Hybrid Actuation in Haptics Conclusions

Our hybrid control approach brings dynamic range needed to render diverse virtual environments to the handheld form factor. Our hybrid control system does so though the use of a novel particle brake model, partitioning system, and torque feedback. The actuation and control approach enables increased dynamic range and eliminates common hybrid rendering artifacts like the "sticky wall". Our parallel hybrid approach enables simple mechanical design necessary for handheld haptic applications while the balanced hybrid approach enables larger workspace and higher force haptic devices than previously possible.

B. Hybrid Actuation in Cooperative Physical Human Robot Collaboration Conclusions

Our balanced hybrid human friendly robotic actuator has many benefits. Designing the individual actuators in parallel allows us to size them to be of comparable torque capability which in turn grants the actuation method a high dynamic range while maintaining a low output inertia necessary for safety in cooperative robotics. Our experiments show adding a passive actuator can increase the actuation and power absorption capability of the hybrid actuator, enable lower energy costs, and help to overcome other actuation limitations like SEA velocity saturation in a safe manner. Despite the notable advantages, balanced hybrid actuation comes with some limitations. The first being the added complexity of combining three actuators in parallel. Another disadvantage is the added friction and weight of the DC motor and brake. With that said the presented design was not optimized for weight and additional research into passive actuation itself could help to reduce weight and latent friction in the current design.

C. Future Work and Directions

The Multiple degree of freedom testbed developed as part of this work will provide a platform for future haptics and cooperative robotics research. It represents a step towards higher power and larger workspace haptic and cooperative robotic devices.

Future work specific to haptics could include extending the analysis shown here to virtual inertia in a single degree of freedom and multiple degrees of freedom. Theoretically the hybrid actuator should be able to increase the range of passive virtual inertia as well. However, this was not extensively experimentally tested in this work. The prototype hybrid handheld device presented here only contains one degree of freedom and weighs 550 grams. Integrating the passive torque sensor more fully into the structure of the actuator by using bonded strain gauges would simplify design further, stiffen the device, and reduce weight. Additional design iterations could significantly reduce the weight and size. Limitations on the hybrid actuation approach, especially cable compliance, could and should be a focus of future work as well.

Future work specific to cooperative robotics includes an investigation of multi-phase optimization and model predictive control, to utilize the full brake model in our trajectory optimization program and to enable DC feedforward brake torques. Deploying the trajectory optimization algorithms on a multi degree of freedom testbed to show how hybrid actuators can benefit higher degree of freedom systems would be an important contribution as well. Finally, repeating impact tests on the large-scale multiple degree of freedom system would be a beneficial extension to this work.

Appendix A: Particle Brake Mathematical Model

The particle brake has linear and nonlinear characteristics as mentioned in the particle brake dynamics section of Chapter 2. The block diagram shown in Fig. 1. Summarizes how our brake model is applied.

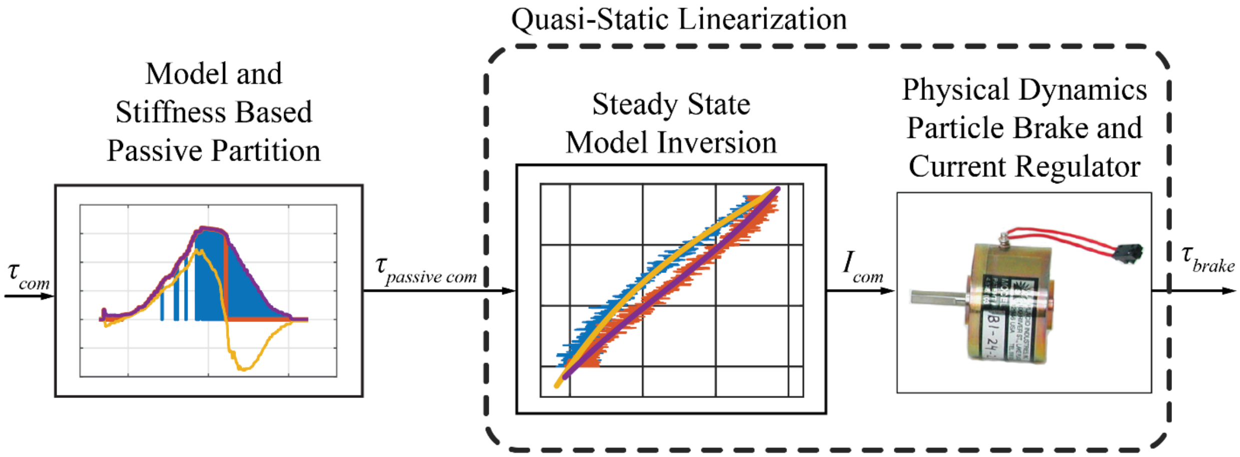

Figure 1. Particle brake compensation methodology. The brake controller uses both a high bandwidth current regulator and a quasi-static hysteresis inversion to improve the torque production accuracy of the particle brake.

A. Quasi Static Torque Current Model Inversion

A nonlinear and hysteretic relationship exists between the current flowing in the brakes coil and the steady state output torque of the brake as shown in Fig. 2. To model this relationship and increase the accuracy of the brake's steady state output torque we utilize a model inverse solution. Inverting the steady state or quasi-static torque to current relationship and fitting third order polynomials to the rising and falling curves forms the boundary of the rate independent hysteretic relationship. We utilize a rate independent hysteresis model of the Dahl variety to transition back and forth between the two fitted curves forming minor loops, Fig. 2.

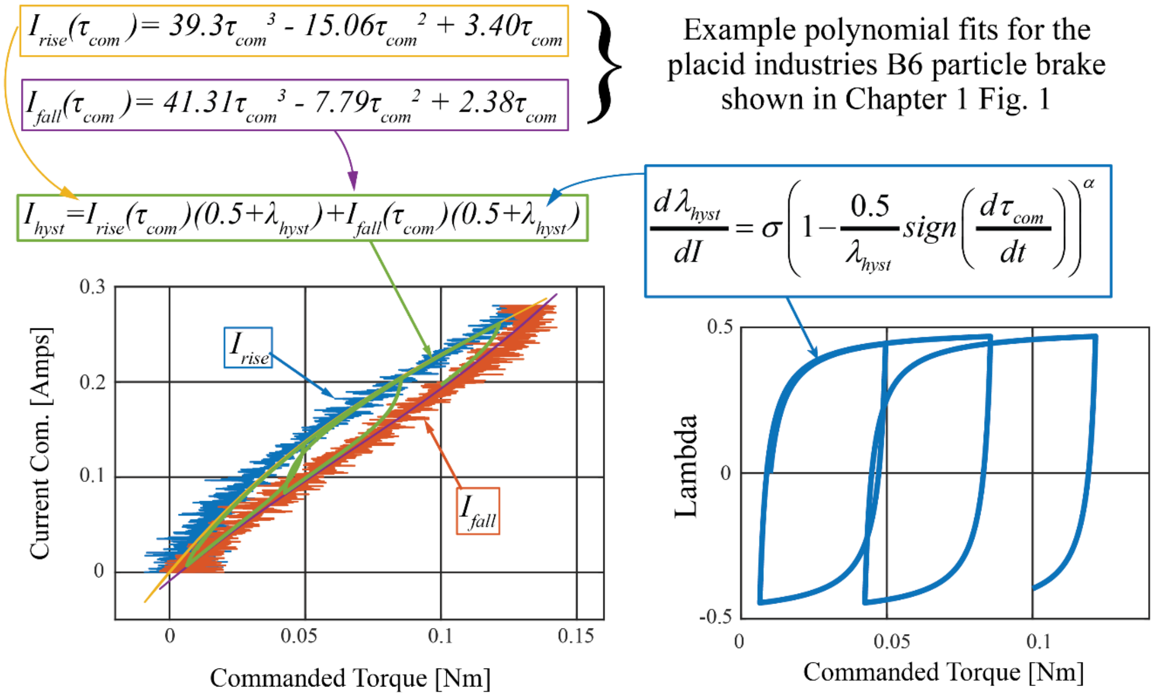

a) Quasi-static relationship

b) Hysteresis Element

Figure 2. Quasi-static current hysteresis compensation method. a) Two third order polynomials bound the hysteretic behavior in the particle brake which occurs due to traversing the B-H curve. b) The hysteresis loops are developed by transitioning between the two using the Dahl inspired hysteresis model. The result is a closer torque command to torque output while the brake is slipping.

B. Velocity Reversal Dynamics – Mechanical Hysteresis

As stated in the particle brake dynamics section of Chapter 2 we use a modified Dahl friction model, (32), to model mechanical hysteresis observed in the brake.

$$\frac{d\tau_b}{d\theta_b} = \sigma\left(1 - \frac{\tau_b}{\tau_c} sign\left(\frac{d\theta_b}{dt}\right)\right)^{\alpha} \tag{32}$$

Where:

$\sigma =$ Brake Stiffness K_b

$\tau_b =$ Brake torque

$\alpha =$ Hysteresis shape parameter

$\theta_b =$ Brake rotor position

$\tau_c =$ The coulomb or steady state brake torque

The modified Dahl model utilizes the output of our electrical dynamic model to change the steady state brake torque. Our quasi-static model inversion makes this possible by linearizing steady state torque characteristics of the brake.

C. Electrical Dynamic Model

Electrical dynamics of the brake give it low pass characteristics. The brake amplifier (Copley JSP-090-10) utilizes a PI current controller. Resistance and inductance associated with the brake's coil limits the rate of change of current and steady state torque production. A closed loop transfer function describing the command tracking current response of a linear inductive load may be written in the form of (33) and is used to represent electrical dynamics of the brake. Where K_p and K_i are the proportional and integral gains of the PI current regulator. L and R are the inductance and resistance of the particle brake coil respectively.

$$\frac{\tau(s)}{\tau^*(s)} = \frac{I(s)}{I^*(s)} = \frac{K_p s + K_i}{Ls^2 + \left(R + K_p\right)s + K_i} \tag{33}$$

Appendix B: Online Impedance Estimation

A more general stiffness estimation approach might be necessary for applications in nonlinear or telerobotic environments where the stiffness of the rendered impedance is unknown. In this case we adopt a method for online parameter estimation. One method we have found useful to estimate the linear stiffness of an unknown virtual environment is the restoring force surface method (34) and [1].

$$\begin{aligned} K_{est} &= \left(A^T A\right)^{-1} A^T b \\ A &= \left[\theta_k \quad \theta_{k-1} \quad \theta_{k-2} \quad \cdots \quad \theta_{k-n}\right] \\ b &= \left[\tau_k \quad \tau_{k-2} \quad \tau_{k-2} \quad \cdots \quad \tau_{k-n}\right] \end{aligned} \tag{34}$$

Where:

$K_{est} =$ The estimated stiffness at the current sample instant

$\theta =$ The measured position error of the actuator at sample k.

$\tau =$ The torque commanded to the actuator at sample k.

n = the number of samples to estimate the parameters over

The equations shown in (34) can be expanded to estimate numerous parameters from a simple state vector and torque input. For example, damping torques could be estimated by expanding A in (34) to include velocity data in addition to position data. The output of the Moore-Penrose inverse or pseudoinverse would have a dimension of 2x1 where the first row indicates the estimated stiffness, and the second row indicates the damping. Incorporating an online stiffness estimation method into our control algorithm makes it suitable for the most general circumstances encountered by a haptic device.

References

[1] M. S. Allen, H. Sumali, and D. S. Epp, “Piecewise-linear restoring force surfaces for semi-nonparametric identification of nonlinear systems,” *Nonlinear Dyn.*, vol. 54, no. 1–2, pp. 123–135, Oct. 2008, doi: 10.1007/s11071-007-9254-x.

Appendix C: Dahl Brake Model - Equivalent Stiffness and Damping

Equivalent stiffness and damping can be calculated by first assuming a displacement and resulting velocity (35) and (36) respectively.

$$x = A\cos(\omega t) \tag{35}$$

$$\dot{x} = -\omega A\sin(\omega t) \tag{36}$$

We can then calculate the time domain waveform of the nonlinearity and find the first two Fourier coefficients (37) and (38).

$$a = \frac{2}{T}\int_{-\frac{T}{2}}^{\frac{T}{2}} F_f(t)\cos(\omega t)dt \tag{37}$$

$$b = \frac{2}{T}\int_{-\frac{T}{2}}^{\frac{T}{2}} F_f(t)\sin(\omega t)dt \tag{38}$$

Recognizing that equivalent stiffness and damping are forces proportional to displacement and velocity we can equate the Fourier coefficients to our assumed position and velocity waveforms resulting in (39) and (40).

$$a\cos(\omega t) = K_{eq}A\cos(\omega t) \tag{39}$$

$$b\sin(\omega t) = -B_{eq}\omega A\sin(\omega t) \tag{40}$$

Solving (39) and (40) for the equivalent stiffness and damping results in amplitude dependent parameters (41) and (42) respectively and is similar to the approach used in [1].

$$K_{eq} = \frac{a}{A} \tag{41}$$

$$B_{eq} = \frac{-b}{\omega A} \tag{42}$$

Applying this method to the Dahl friction nonlinearity numerically begins by assuming an oscillation amplitude and calculating the resulting output of the nonlinear model as shown in Fig. 1. The sum of the first coefficients of the Fourier series for the resulting motions are plotted over the friction waveforms to show the connection between the two waveforms.

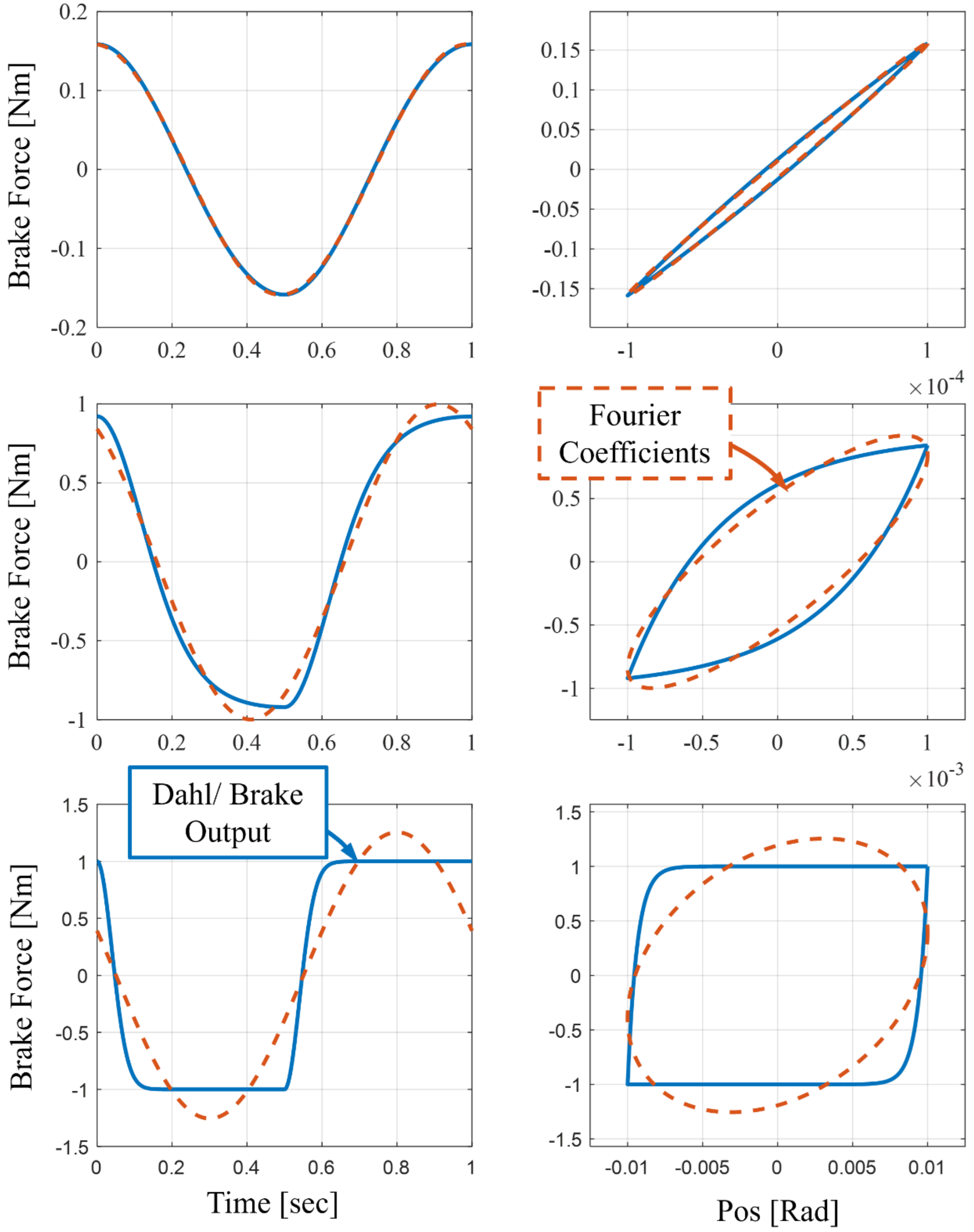

Figure 1. Dahl friction time domain wave forms. The running friction parameter of the brake is set to 1 Nm (F_c = 1Nm) and the brake stiffness is set to 1600 Nm/rad in accordance with real observed values. At small deflections the brake functions almost as a pure stiffness. As oscillations increase in amplitude the mechanical hysteresis increases resulting in more dissipation.

Plotting the equivalent stiffness and damping of the model against both amplitude and frequency shows that the brake performs as a pure stiffness at small deflections as seen in Fig.2.

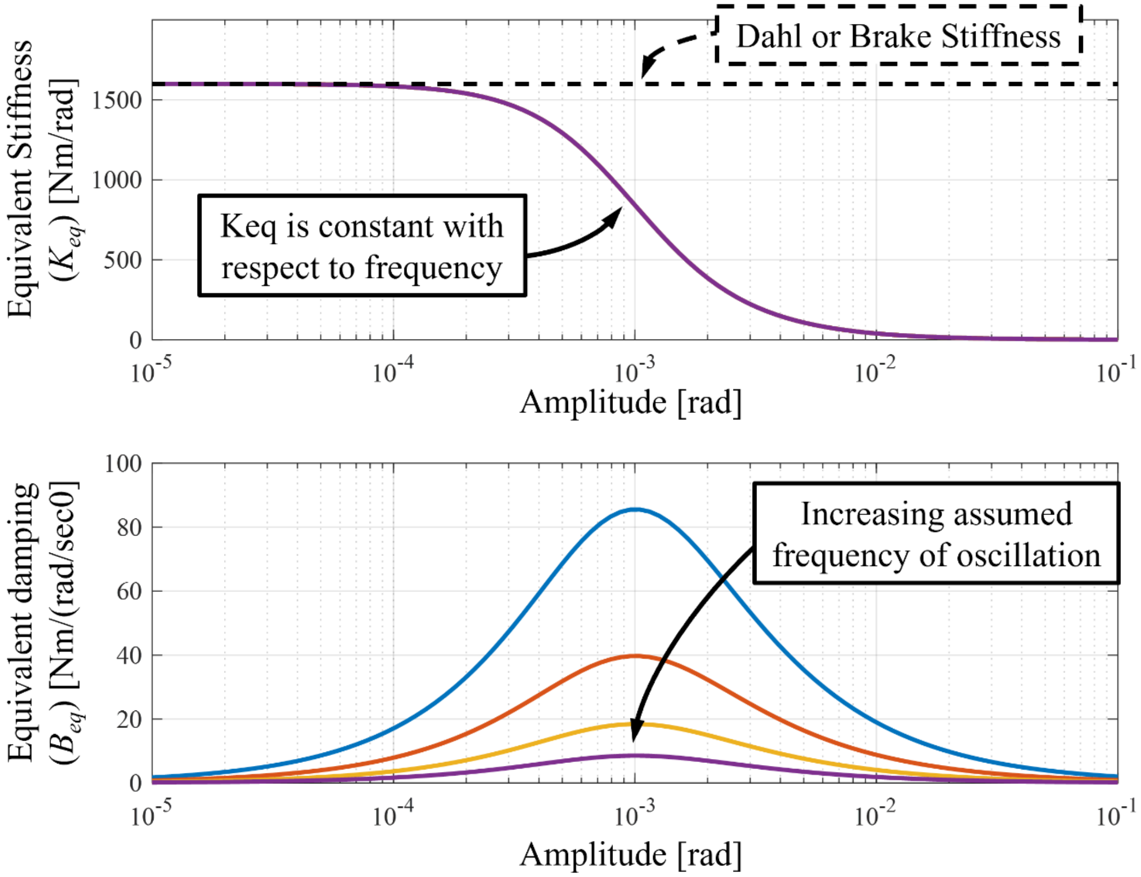

Figure 2. Brake and Dahl friction equivalent stiffness and damping. Again, the running friction parameter of the brake is set to 1 Nm (F_c = 1Nm) and the brake stiffness is set to 1600 Nm/rad in accordance with real observed values. At small deflections the brake functions almost as a pure stiffness and the brake's equivalent damping increases until it reaches a peak. This peak is strongly influenced by the brake engagement or running friction (F_c or τ_c). Increasing F_c both increases the height or magnitude of the peak in damping and shifts the peak to higher amplitudes of oscillation. As oscillations increase past the peak both the equivalent stiffness and damping approach zero. Equivalent damping also has an inverse relationship to frequency that is reflected in (42).

Furthermore, if we can always arbitrarily increase the running friction parameter F_c in the Dahl model by simply increasing the brake current and correctly sizing the brake saturation limits (installing a large enough brake), we can always treat the brake as a pure stiffness. This is the motivation behind brake stiffness simplifications to a pure physical stiffness used in the analytical stability analysis from in Chapters 2 and 3. Neglecting brake damping as an important part of the brakes dynamics is motivated by the lack of equivalent damping at small amplitudes of motion. Furthermore, due to the frequency independent nature of the brake torque and Dahl friction the damping provided by the brake decreases as the assumed frequency of oscillation increases. Essentially making damping provided by the uncontrolled or open loop response of the brake a somewhat unreliable form of dissipation and haptic device stabilization. An analysis of the effects of coulomb friction in [2] shows similar results where column friction has the ability to stabilize a haptic device but only over a limited range of velocities or position oscillations.

References

[1] D. Helmick and W. Messner, “Describing function analysis of Dahl model friction,” in *2009 American Control Conference*, St. Louis, MO, USA: IEEE, 2009, pp. 814–819. doi: 10.1109/ACC.2009.5159996.

[2] N. Diolaiti, G. Niemeyer, F. Barbagli, and J. K. Salisbury, “Stability of Haptic Rendering: Discretization, Quantization, Time Delay, and Coulomb Effects,” *IEEE Trans. Robot.*, vol. 22, no. 2, pp. 256–268, Apr. 2006, doi: 10.1109/TRO.2005.862487.

Appendix D: Hybrid Feed Forward – Trajectory Optimization Formulations

Direct collocation is a numerical method of trajectory optimization which transcribes the dynamics of our system, shown in Fig. 1a and b, into constraints in an optimization problem. Time is discretized at knot points and the dynamics of our system constrains the states at each knot point. A full description of the direct collocation method is out of the scope of this paper. However, [1] provides an excellent introduction to the method. In this work we used Julia and JuMP to transcribe the dynamics into a nonlinear optimization problem and the open-source interior point solver IPOPT to solve all the optimization problems presented in this work.

As stated previously direct collocation relies on the transcription of the system dynamics into constraints. It is important to explore the necessary level of model complexity as a part of the transcription process. While the actual system is more complicated than the two-mass system shown in Fig. 1a calculating a lumped equivalent inertia and damping at the output of the SEA speed reducer and at the robot's link proved to be an effective model for feedforward control of the actuator.

Including the series elastic actuator controller in the optimization problem improved experimental results dramatically. The full dynamics of the particle brake can be represented by a modified Dahl friction model as shown in [2]. Instead, we chose to represent the nonlinear brake dynamics with a smoothed version. A sigmoid function, shown in Fig 1, enforces a purely dissipative constraint on the torque contribution of the brake while allowing for the use of a gradient based nonlinear optimizer.

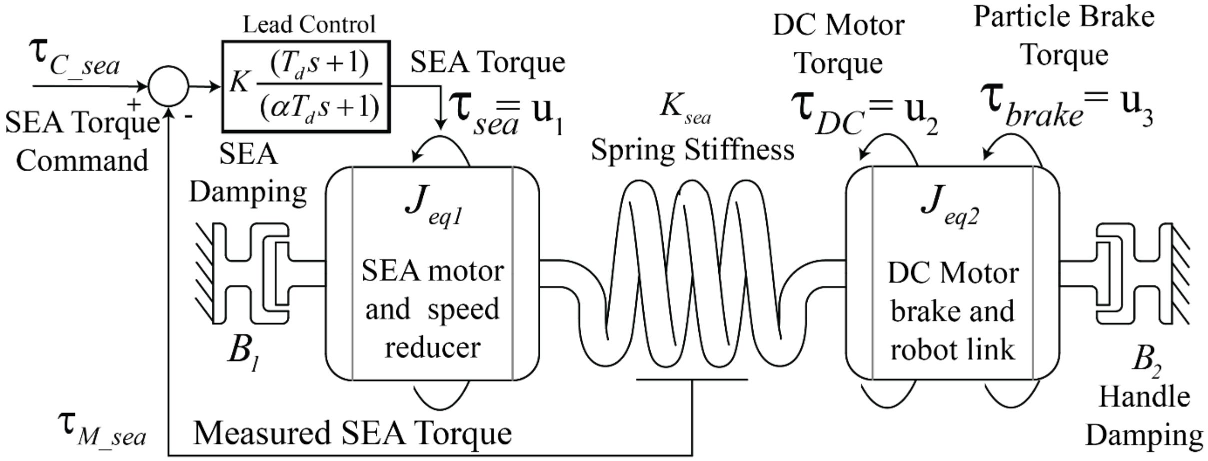

a) Linear portion of the actuation model and SEA feedback controller

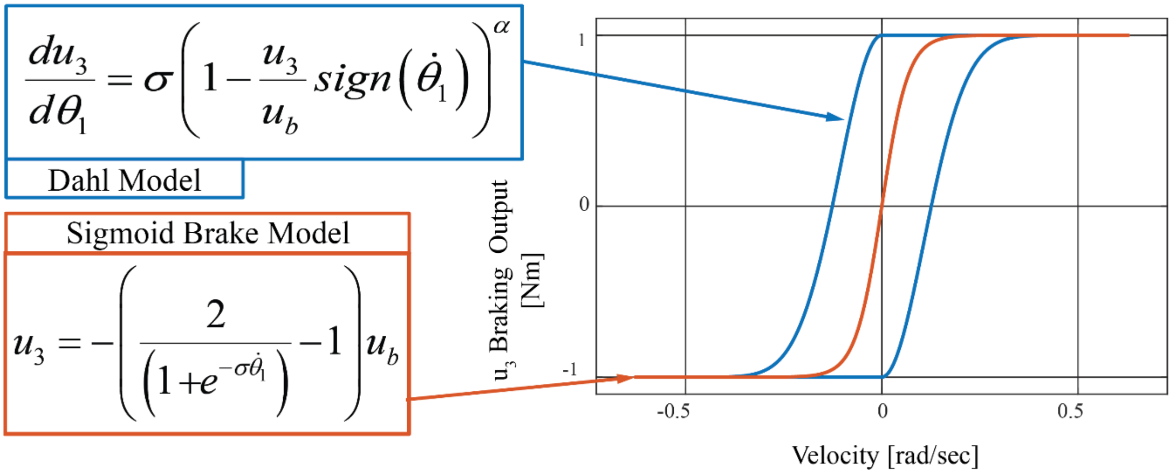

b) Comparison between the Dahl and sigmoid dynamic brake models

Figure 1. Diagram of the equivalent two mass actuator system. a) The model includes equivalent SEA and robot link inertia. For optimization purposes the system includes the series elastic actuator controller (single lead) and the state feedback position controller. b) Comparison of the brake model friction force output showing the differences between the more accurate Dahl model and the sigmoid brake model used in the optimization formulation. Dahl: $\sigma =$ Model stiffness, $\alpha =$ hysteresis shape parameter. Sigmoid: $\sigma =$ slope at origin, u_b = steady state brake torque command.

A. Time Optimal Control Formulation

The time optimal control problem can be solved using direct collocation, as shown in (43)-(50), where the time in-between a finite number of collocation points is treated as a decision variable and is minimized. The time in-between collocation points are included in the Euler integration numerical approximation of the linear state equations shown in (44). Time optimal control must include actuation saturation limits to be well posed as shown in (46)-(48) and have a solution.

Minimize:

$$J = T_S T \tag{43}$$

Subject to: $For: k = 0, 1, \ldots T-1$

$$\frac{\left(x_{k+1} - x_k\right)}{T_s} = Ax_k + Bu_k \tag{44}$$

$$u_{3_k} = \frac{-2u_{b_k}}{\left(1 + e^{-\sigma \dot{x}_1}\right)} + u_{b_k} \tag{45}$$

$$-\tau_{A1_{sat}} \le u_{1_k} \le \tau_{A1_{sat}} \tag{46}$$

$$-\tau_{A2_{sat}} \le u_{2_k} \le \tau_{A2_{sat}} \tag{47}$$

$$0 \le u_{b_k} \le \tau_{b_{sat}} \tag{48}$$

$$x_0 = \begin{bmatrix} 1 & 0 & 1 & 0 & 0 \end{bmatrix} \tag{49}$$

$$x_T = \begin{bmatrix} 0 & 0 & 0 & 0 & 0 \end{bmatrix} \tag{50}$$

B. Minimum Energy Control Formulation

Minimum energy trajectory optimization minimizes the actuation costs to achieve a given trajectory. The cost function utilizes a matrix “R” shown in (51) which weights the relative costs of each actuator. In the trajectories shown we assign the relative weight of the SEA actuator and the DC motor as the ratio of the transmission ratios. That is to say that the ratio of R1 to R2 is set to be 4.7:1. Our justification comes from the effective gain of each actuator themselves. The brake is more efficient at producing torque than either the SEA or the DC motor within its limited dynamics and we penalize the brake's actuation much less than either actuator. The ratio of R2 to R3 is 10:1 for all the plots in this work.

Minimize:

$$J = u^T diag\left(\begin{bmatrix} R_1 & R_2 & R_3 \end{bmatrix}\right) u = u^T R u \tag{51}$$

Subject to: $For : k = 0, 1, ...T - 1$

$$\frac{\left(x_{k+1} - x_k\right)}{T_s} = Ax_k + Bu_k \tag{52}$$

$$u_{3_k} = \frac{-2u_{b_k}}{\left(1 + e^{-\sigma \dot{x}_1}\right)} + u_{b_k} \tag{53}$$

$$x_{1_k} = x_{1ref_k} \tag{54}$$

C. A Tradeoff Between Actuator Effort and Tracking Error - (LQR) Control Formulation

The LQR style cost function, shown in (55), allows us to investigate the tradeoff between tracking states and the control effort needed to do so. Heavily penalizing the first element in the error vector with the weight Q1 causes the actuators output position to track the desired position closely. Penalizing or increasing Q4, the weight associated with the SEA velocity state, helps to address SEA velocity saturation like described in Chapter 6. The second half of the cost function is identical to that seen in minimum energy control. A main difference between the two cases is that both the handle and SEA mass positions are solved implicitly as part of the optimization problem. Only the SEA states are solved implicitly in minimum energy trajectory optimization.

Minimize:

$$\begin{aligned} J &= e^T diag\left(\begin{bmatrix} Q_1 & Q_2 & Q_3 & Q_4 & Q_5 \end{bmatrix}\right) e \\ &+ u^T diag\left(\begin{bmatrix} R_1 & R_2 & R_3 \end{bmatrix}\right) u \\ &= e^T Q e + u^T R u \end{aligned} \tag{55}$$

Subject to: $For : k = 0, 1, ...T - 1$

$$\frac{\left(x_{k+1} - x_k\right)}{T_s} = A x_k + B u_k \tag{56}$$

$$u_{3_k} = \frac{-2u_{b_k}}{\left(1 + e^{-\sigma \dot{x}_1}\right)} + u_{b_k} \tag{57}$$

References

[1] M. Kelly, “An Introduction to Trajectory Optimization: How to Do Your Own Direct Collocation,” *SIAM Rev.*, vol. 59, no. 4, pp. 849–904, Jan. 2017, doi: 10.1137/16M1062569.

[2] P. Dills, N. Colonnese, P. Agarwal, and M. Zinn, “A Hybrid Active-Passive Actuation and Control Approach for Kinesthetic Handheld Haptics,” in *2020 IEEE Haptics Symposium (HAPTICS)*, Crystal City, VA, USA, Mar. 2020, pp. 690–697, doi: 10.1109/HAPTICS45997.2020.ras.HAP20.12.af578b0a.